POLITECNICO
MILANO 1863

SCUOLA DI INGEGNERIA INDUSTRIALE
E DELL'INFORMAZIONE

Laser Pulse Amplification and Characterization studies at the High Power Laser Facility of ESRF

Tesi di Laurea Magistrale in
Physics Engineering

Author: **Matteo Masto**

Student ID: 928682
Advisor: Prof. Giacomo Claudio Ghiringhelli
Co-advisors: Dr. Nicolas Sévelin - Radiguet
Academic Year: 2020-21

Abstract

The experimental study of matter at extreme pressures and temperatures conditions produced with laser driven dynamic compression implies the use of nanosecond high power lasers. This work aims at studying the temporal profile distortion of laser pulses during amplification due to gain saturation and propose a simulation able to compensate this phenomenon for the case of the amplification chain of HPLF at ID24 of the European Synchrotron Radiation Facility. To complement the simulation a novel approach based on the temporal profile measurements has been adopted to estimate the energy of the pulse and the technique of Passive Pulse Replication developed by Marciante *et al.*[1] has been installed in the facility to provide higher quality measurements of the temporal profile.

Keywords: dynamic compression, shock experiments, high power lasers, laser amplification, Frantz Nodvik equations, computer simulation, temporal profile quality, passive pulse replication

Abstract in lingua italiana

Lo studio sperimentale della materia a pressioni e temperature estreme, prodotte mediante compressione dinamica indotta da luce laser, implica l'uso di impulsi ad alta potenza nell'ordine dei nanosecondi. Questo lavoro ha lo scopo di studiare la distorsione del profilo temporale degli impulsi laser causata dalla saturazione del mezzo amplificatore e di proporre una simulazione in grado di riprodurre e compensare questo fenomeno nel caso specifico della High Power Laser Facility dello European Synchrotron Radiation Facility. Per completare la simulazione è stato adottato un nuovo approccio basato sulle misurazioni del profilo temporale per stimare l'energia dell'impulso. Inoltre, La tecnica di Passive Pulse Replication sviluppata da Marciante *et al.* [1] è stata installata per fornire misurazioni del profilo temporale di qualità superiore.

Parole chiave: compressione dinamica, laser ad alta energia, amplificazione di impulsi laser, equazioni di Frantz Nodvik, simulazione numerica, qualità del profilo temporale, replicazione passiva degli impulsi

Contents

Introduction

In the following chapters the work of six months internship at the High Power Laser Facility (HPLF) of the European Synchrotron Radiation Facility (ESRF) is presented. The HPLF currently works combined to the Energy Dispersed branch of beamline ID24 (ID24-ED) in which laser driven dynamic compression experiments are performed on compounds whose absorption edges are within the beamline energy range (5 - 28 keV). The peculiarity of this facility is to couple high power laser pulses with time-resolved X-rays absorption spectroscopy to study matter under extreme conditions of temperature and pressure that go beyond what can be achieved nowadays with static compression, and also matter under high strain rates.

These studies, which are interesting among others, for fields like planetary science, fundamental condensed matter, new materials synthesis and inertial confinement fusion, require a precise characterization of the drive laser pulse since its properties determine the characteristics of the produced shock. Moreover, HPLF had a recent upgrade of the laser with the delivery, in June 2021, by the Amplitude company of the Premiumlite 100 setup, able to increase the pulse energy from 15 J up to 100 J. In this framework, the main activity of the internship focused on the understanding of the behaviour of the whole amplification chain and on the characterization of beam temporal profile.

In particular the work done can be divided into three main chapters.

The first, which is the bigger, concerns the study and computer modeling of the amplification of the laser pulse from the seed to the 100 J target and in particular it is focused on the evolution of the temporal profile and the relationship between the seed and the target time shape. It is indeed extremely important in shock experiments to have a well defined drive laser temporal profile to obtain the desired shock characteristics.

In the second chapter, starting from a more technical issue, the energy estimation from temporal profile measurements is discussed. A conceived simple model is presented for the pulse energy - acquired voltage conversion and fitting with measurements is performed.

The third chapter again concerns temporal profile measurements, in particular the implementation of a system able to improve the signal to noise ratio (SNR) of the temporal measurements. The aim of this project is to provide higher quality measurements of the

laser pulse which is in turn responsible for the settings of the conditions of the shock. Even if still the work of characterization of the whole laser setup is not complete, the results obtained from this work represent a move forward the study of the features of HPLF laser.

1 | Matter at extreme conditions at ID24-HPLF

In recent years the scientific interest towards matter under extreme conditions of pressure and temperatures has grown and so did the technologies employed to study such exotic states. It can be surprising to know that the most part of the solid matter present in the universe is confined inside planets at pressures of several hundreds of gigapascals (GPa) and temperatures of thousands Kelvin, while the *ambient* conditions we live in can be considered as a small exception [2]. As one can imagine, such extreme conditions modify the way matter behaves: electronic, magnetic [3] and structural [4] phase transitions can be induced by high pressures and temperatures, and unusual chemical reactions can be activated [5].
In this framework, the possibility to reproduce these extreme scenarios in laboratories together with probing matter behaviors with adequate tools, provides an exclusive resource for planetary science studies [6] as well as for fundamental condensed matter physics [7], industrial applications like new materials synthesis [8] and energy science like Inertial Confinement Fusion (ICF) [9].

Thermodynamic conditions of matter in such extreme pressures and temperature lie in the peculiar regime called Warm Dense Matter (WDM). This regime spans in the phase diagrams from densities in the range of 10^{-2} to 10 g/cm^3 and temperatures from 10^3 to 10^5 Kelvin [10] and stands in between the well described condensed matter and plasma domains. On the contrary WDM is quite difficult to describe theoretically since the usual approximations adopted for coupling and degeneracy of ions and electrons in ideal plasma or pure condensed matter are no longer valid [11]. Indeed, without entering too much into details, we could say that for WDM the strength of the electrical potential between charged particles is comparable with thermal energy while it is instead way higher in condensed phases and way lower in plasma phases. On the other side, the density is high enough to produce partial overlap among atomic wavefunctions. Under these conditions *ab initio* modeling is required, and by now, simulations obtained with the implementation

density functional theory and classical molecular dynamics results have been developed [12]. However models need validation with data thus the realization of experiments probing the WDM domain in concrete samples.

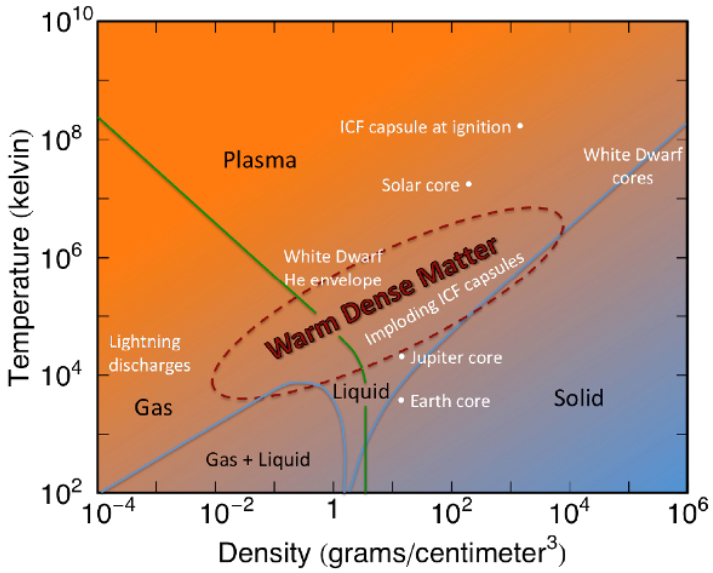

Figure 1.1: Temperature - density phase diagram showing the Warm Dense Matter region [13]

Practically one can say that such extreme conditions are achieved in laboratory frames with two different approaches. Historically the *static compression* has been developed first, with the use of Diamond Anvil Cells (DAC) which allowed to achieve pressures in the order of few hundreds of GPa [14] while successive developments carried to the *dynamic compression* approach which is nowadays the only experimental technique that can reproduce pressures in the TPa range and temperatures in the order of 10,000 K [15]. Main loading techniques are gas guns [16], which have been the first to be used, and high power pulsed lasers, as in our case, but similar experiments have been performed also with Z-machine [17] and with neutrons. In our brief discussion we will focus only on laser induced dynamic compression experiments.

1.1. Laser Driven Dynamic compression

In laser driven dynamic compression experiments a high energy pulse ($I \geq 10^{12}\ W/cm^2$), usually in the nanosecond range, is focused onto an absorbing medium glued onto the

sample to be studied. The high intensity of the drive laser ionizes the absorbing layer producing plasma. The first electrons removed from their atoms get accelerated by the laser electric field and trigger an avalanche process of ionisation of neighbouring atoms due to collisions [18]. Such process, called *laser ablation*, entails the expansion of the plasma in a direction normal to the surface and thus, by reaction, the generation of the compression wave that propagates normally through the target inducing the aimed dynamic compression.

Depending on the intensity temporal profile of the drive laser is possible to have different types of compression waves that in turn move the thermodynamic quantities to different final states in the phase diagrams. Indeed, if the perturbation is abrupted in time, i.e. the intensity temporal profile of the laser pulse has a sharp rising edge we have the production of a *shock wave* that propagates in the sample. In other situations in which the temporal shape of the drive laser gradually increases in time, the shock does not occur and the compression occurs smoothly. These kind of experiments are usually called *ramp* compressions. It is hence clear that the characterisation of the drive laser temporal profile is crucial for its major role in the definition of the shock properties. From now on we will focus mainly on *shock* compression since it is what is currently performed at the HPLF, thus the laser pulse we are considering are high contrast top-hat shaped ones.

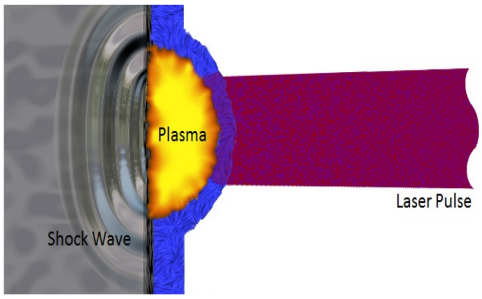

Figure 1.2: Pictorial view of a laser driven shock experiment.[19]

The formalism that describe the evolution of the thermodynamic quantities of under shock waves is a credit to W. J. M. Rankine and P. H. Hugoniot [20][21] who first derived three equation of state for the density, the pressure and the energy density of the material starting from the conservation laws of mass, momentum and energy. From the knowledge of initial conditions of those three quantities and the characteristics of the shock it is possible to know their final state in the phase diagram. The curve that collects all the values of density, pressure and energy density achievable during the shock dynamics it is called Hugoniot curve. If we were performing *ramp* compression experiments, on the

other hand, we would be able to follow the compression over the *isentropic* curve (adiabatic compression).

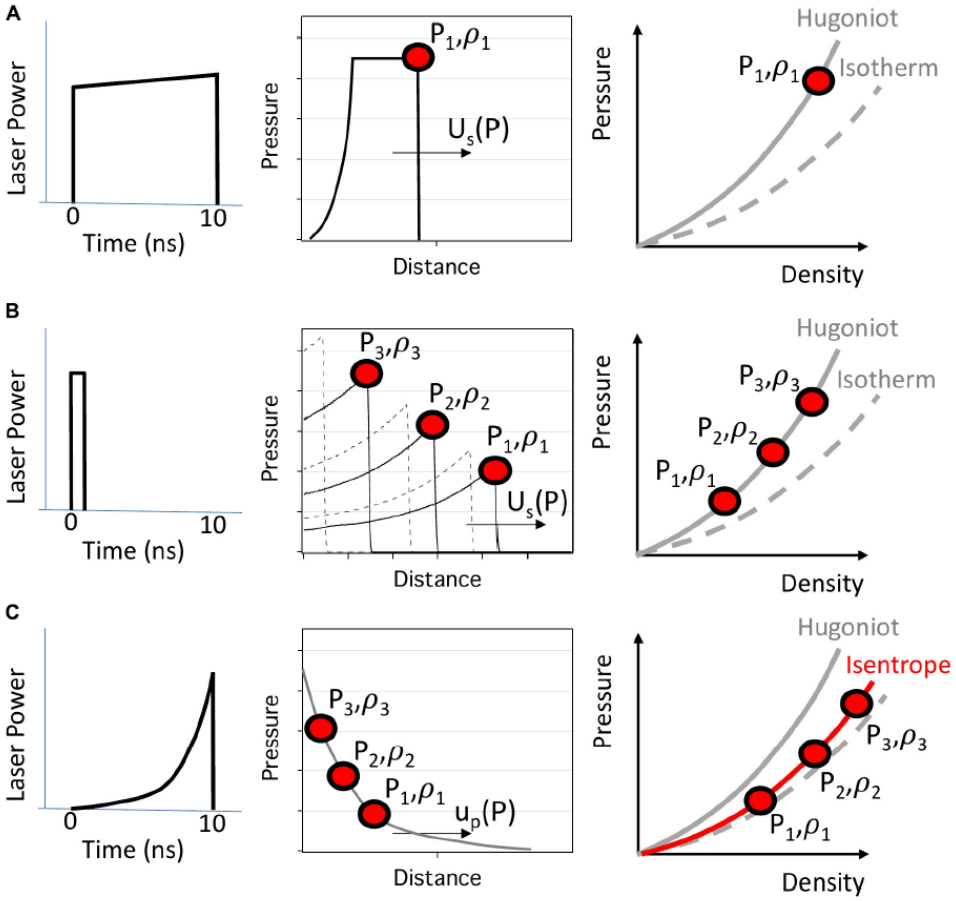

Figure 1.3: Illustration of the three main laser induced dynamic compression. **A)** Temporally steady shock wave produced by a nearly top-hat laser pulse. The shock wave propagates with the pressure dependent shock speed $U_s(P)$ and a single compression state is generated on the Hugoniot curve of the material. **B)** With shorter duration laser pulses we have a temporally decaying shock which produces different discrete states along the Hugoniot curve. **C)** A ramp profile of the drive laser generates a continuum of states close to the isentrope of the material. [15]

Regarding the *spatial* intensity profile of the drive laser we want it to be homogeneous as much as possible. This requirement is necessary to guarantee the uniformity of the shock wave within the sample thus the validity of the assumption to achieve the same thermodynamic conditions for a given position along the propagation direction [22]. However, due the high degree of spatial and temporal coherence of laser light, the spatial profile is affected by non-uniformities and intensity spikes [10]. One way to break this spatial coherence is to use phase plates, i.e. transparent plates that induce a space-dependent

shift, before the last focusing lens. However, to increase the smoothing of the spatial profile one can act also on the *temporal* coherence of the laser pulse with another technique called Smoothing by Spectral Dispersion described in section 2.1.1.

1.2. Shock Diagnostic

Once that one is able to produce the shock, a proper instrumentation to monitor and extract the results of the compression must be found. On one side we want to retrieve the information on the spatial and temporal evolution of the hydrodynamic parameters during the compression while on the other side we want to to probe the changes over time of the sample's atomic and electronic structure. One of the most common choices to collect data on pressure, density and temperature evolution is the employment of the Velocity Interferometer System for Any Reflector (VISAR) and of the Streak Optical Pyrometer (SOP). The analysis of the microscopic structure of samples requires instead brilliant and short pulsed sources of X-rays for absorption spectroscopy or diffraction techniques. For this reason important primary X-rays sources as synchrotrons (ESRF in France and APS in United States) and XFELs (LCLS in United States, the European XFEL in Germany and PAL-XFEL in South Korea) have opted for the coupling with "compact" high power lasers for dynamic compression studies.
A brief overview of the mentioned techniques for shock diagnostics follows in the next three sections. About X-rays techniques we will present the Time Resolved X-rays Absorption Spectroscopy (TR-XAS) which is conducted at ID24-HPLF.

1.2.1. Velocity Interferometer System for Any Reflector

The VISAR system is a widely use technique that allows to measure the shock and particle velocity, i.e. the speed at which the shock wave propagates or the slower speed of the shocked particles. The knowledge of this parameter allows to obtain the density and the pressure values inside the material at the position of the shock front through the mentioned Rankine-Hugoniot relations. The principle of operation is based on the figure of interference created by the probe laser light reflected by the back of the sample. To be precise, the measured velocity can refer to a free reflecting surface, to the interface between reflecting surface and a transparent window or directly the shock speed of a reflecting moving shock front [23]. The type of reflecting surface in turn depend on the configuration of the sample, the type of target material and the pressures achieved.
The main effect is that the reflected laser beam experiences a Doppler shift dependent on the velocity of the reflecting surface. Such reflected beam is injected in a classic

Mach - Zehnder interferometer where in one arm an *etalon* is placed. This last object introduces an already known phase delay to the light passing to the corresponding branch of the interferometer. When the two beams reunite, a figure of interference is created and recorded by a streak camera. When the velocity changes in time we have a modification in the wavelength of the reflected beam thus a collective motion of the fringes. It can be proved that the velocity is proportional to the phase shift of the fringes and another factor named Velocity Per Fringe, which represents the velocity for which the fringe system is shifted of a fringe. This last quantity depends on the wavelength at rest, on the *etalon* parameters and on a correction parameter that accounts for the dispersion induced by the *etalon*.

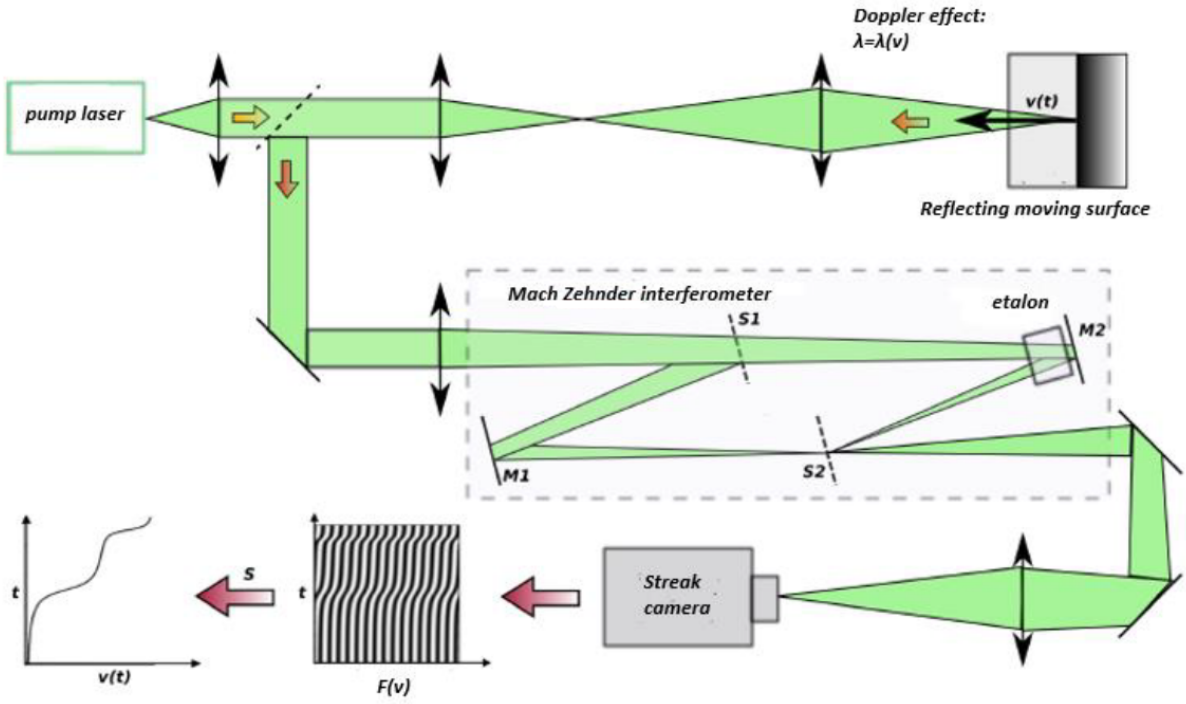

Figure 1.4: Schematics of the VISAR system. The reflected laser beam enters the Mach - Zehnder interferometer and produces the interference fringes captured over time by the streak camera. The horizontal variation of the fringes pattern is proportional to the velocity of the reflecting surface. [23]

Since only the offset corresponding to a fraction of the fringe can be measured, usually a second VISAR with different *etalon* is used in parallel. Another important resource of the VISAR system is the capability, if properly tuned, to measure the reflectivity of the reflecting surface through the intensity of the interference fringes. This last feature is of particular interest either because allows to measure the average shock velocity also in some transparent materials but either because it is useful also for the temperature measurement

provided by the SOP. Usually the two employed VISARs use two different wavelengths (for instance Nd:YAG 1064 nm and the SH at 532 nm) to have the measurement of the reflectivity for both the wavelengths.

1.2.2. Streak Optical Pyrometer

As just mentioned, this diagnostic tool is designed for the temperature measurement which is the missing thermodynamic variable to retrieve. The principle of operation is based on the fact that when the sample gets heated by the shock wave it emits radiation according to the its temperature and to its composition.
More precisely, the spectral radiance $B_\lambda(\lambda, T)$ emitted is linked to the temperature of the body through the Planck's law of black body radiation. The self-emitted radiation is captured by the CCD sensor, placed after a streak camera, that is able to create a bi-dimensional image representing in time and space the intensity of the radiation, i.e. somewhat the temperature of the reflecting surface both in time and space.

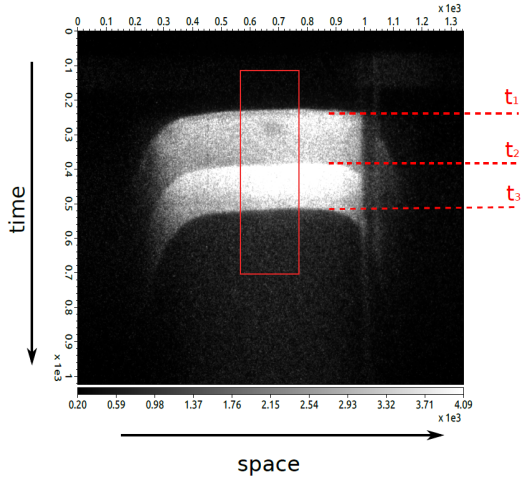

Figure 1.5: Image taken by a SOP diagnostic. The brightness in the image is somewhat proportional to the intensity of the radiation, thus on the temperature of the reflecting surface.[19]

To retrieve this relation between the brightness in the image and the temperature one has to consider few aspects.

Firstly, for a real object the ideal spectral radiance is lower than the ideal black body one, namely it is damped by the *emissivity* $\epsilon(\lambda, T)$ of the material. Such quantity measures the effectiveness of a real body with respect to the black body, in emitting electromagnetic

radiation [10] and it is directly obtainable by the reflectivity of the material measured with the VISAR.
Then, another aspect to be considered is that the pyrometer has finite working spectral interval that is dictated by both the streak camera spectral efficiency and the self-emission maximum of the spectral radiation. To give some numbers this range is in between the 300 nm and the 500 nm having the self- emission maximum around 300 nm for typical achieved temperatures. At this point an approximation, named *grey body approximation*, is taken into account. Since we only know the emissivity at the wavelength of the probe laser it is convenient to neglect the variation of such quantity between the measured value and the actual one corresponding to the SOP spectral range. This assumption is justified for the reflectivity measured by the 532 nm probe laser (very close to 500 nm of the SOP range).
At this point one has to consider the optical system that lies in between the incoming radiation and the CCD sensor of the streak camera that will produce the image. The influence of this optical system on the output image can be summarized by a wavelength dependent *transmissivity*. With this last consideration, the time-dependent number of counts is given by the integral over all the possible wavelengths of the spectral radiance of the reflecting surface self-emitted radiation times the transmissivity of the optical systems interposed. The number of counts recorded is encoded in the image brightness and a post-process of the image that follows all these passages is finally able to retrieve the temperature of the surface.

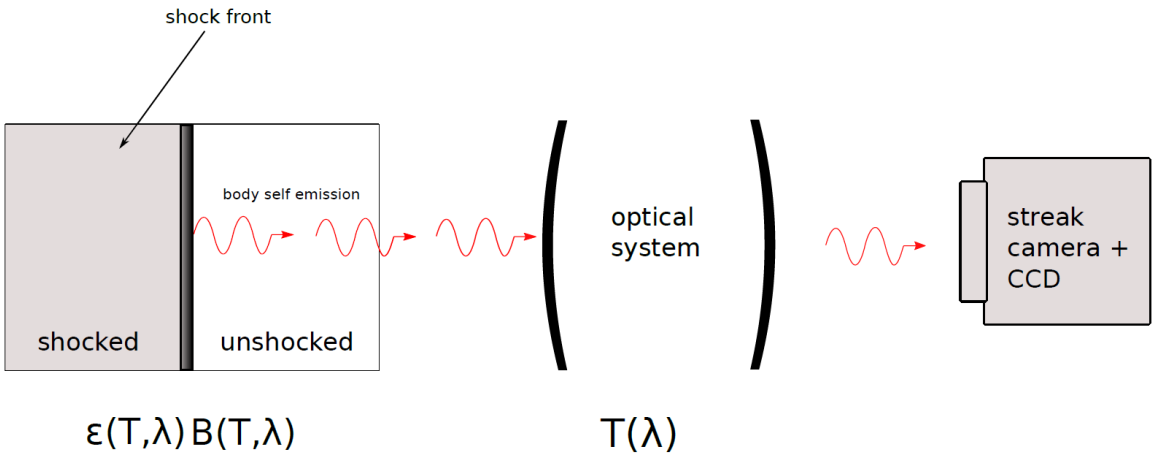

Figure 1.6: Schematics of the SOP instrument. The spectral radiance of the reflecting surface is given by its emissivity times the black body spectral radiance. The interposed optical system has a spectral trasmissivity that filters the self-emitted radiation reaching the streak camera.[19]

It is important for reliable measurements to properly calibrate the instrument with references and to characterise the parameters of the optical system such as the solid angle, the magnification and the overall transmissivity. Moreover also, due to the finite working spectral range, there is a minimum detectable temperature which usually, for dynamic compression experiments, is around 5000 Kelvin [23].

1.2.3. Time Resolved X-Rays Absorption Spectroscopy at ID24-HPLF

To provide an exhaustive explanation of the TR-XAS technique carried out at the beamline ID24 would require a dedicated document, thus in this paragraph only the key aspects are presented with a particular stress on the specific case of ID24.

This method relies on the analysis of the absorption coefficient spectrum $\mu(E)$ of the target material when probed by X-ray radiation. For the typical energies of X-rays, the dominant process of absorption is the photoelectric effect which, in brief, consists in the excitation of a core-level electron (namely K, L or M shell) of the material. The excited electron is ejected from the atom and the excited core-hole left relaxes to the ground state through the incoming of a secondary higher-level core electron [24].
Due to the energy separation among core levels, the absorption coefficient spectrum produces amplitude jumps in correspondence of the energy of the absorbing core level. Indeed, the absorption increases when the radiation energy matches the core-level energy while decreases when it is far from it.
The information on the sample that can be derived by XAS techniques lies precisely inside the shape of the absorption coefficient spectrum in the region near to the jump. Indeed the analysis of this region of the spectrum takes the name of X-rays Absorption Near-Edge Spectroscopy (XANES) or Extended X-rays Absorption Fine Structure (EXAFS) depending on the spectral region considered. It must be said that they cannot be analysed in the same way and also the information content is different. Typical analysis conducted at ID24 for dynamic compression experiments focus on EXAFS region which provides information on the local strucure of the material.
To have a rough idea of this fact one should consider that in condensed matter systems the presence of neighbouring atoms *interferes* with the motion of the excited electron in a way that is related to the position in space of the atoms. It can be demonstrated that this phenomenon of interference modifies the absorption coefficient value that assumes a decaying oscillating behaviour in the proximity of the absorption edge. Translating this trend in the k-space and Fourier transforming it is possible to obtain information on the

local coordination in the real space, thus analyse the crystal structure.

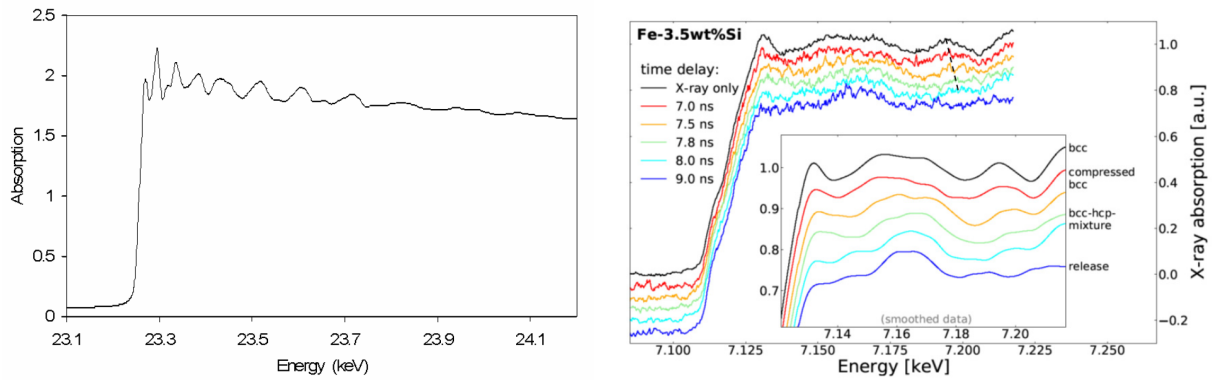

a) b)

Figure 1.7: a) Example of EXAFS spectrum of rhodium foil.[2]. b) Time evolution of EXAFS spectrum of Fe-3.5% wtSi. The interpreted data allowed to describe the modifications of the internal crystal structure of the compound [5].

Moving to the features of ID24-HPLF we can say that the beamline covers the energy range from 5 keV to 28 keV, in which the absorption edges of elements between titanium and uranium [2] lie. The peculiarity of the beamline is to focus onto the target not a monochromatic X-rays beam but a polychromatic one. Indeed, the X-ray pink beam from the beamline is simultaneously diffracted and focused onto the sample by the polychromator (a bent silicon crystal). In this focusing fan of X-rays, to each angle corresponds a single energy (Bragg diffraction). They are all focused onto a single spot on the sample where they are partially absorbed and diverges downstream the latter. Then they are collected onto a position sensitive detector able to correlate each position in space to the corresponding specific energy in the polychromatic fan of X-rays (see Fig.1.8 a)). The major advantage of this setup is the possibility to acquire an entire EXAFS spectrum in one single shot. It is however necessary to couple this feature to a fast enough detector to produce time-resolved spectra aimed at recording the structural modifications during the shock. The main detector the beamline disposes of is based on an array of 1024 germanium micro-strips specifically designed for this purpose [25][26].

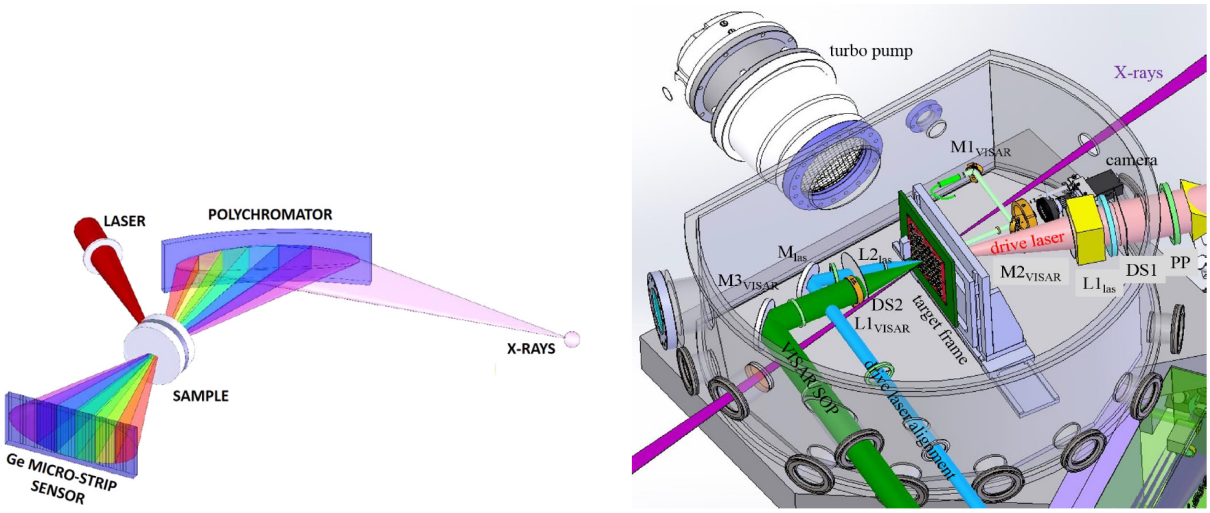

a) b)

Figure 1.8: a) Illustration of the energy dispersion with the polychromator. The curvature of the polychromator follows the profile of an ellipse whose foci are occupied by the X-rays source and the sample. [25]. b) CAD view of the Interaction Chamber of ID24 [23].

According to the energy position of the absorption edge that one wants to study, it is possible to move the whole apparatus comprehending the interaction chamber, the laser transport and the diagnostic systems in the position corresponding to the wanted energy range (see Fig. 2.3). Within these operations the focus of the drive laser, the focus of the X-rays and their angle of incidence remain unvaried.

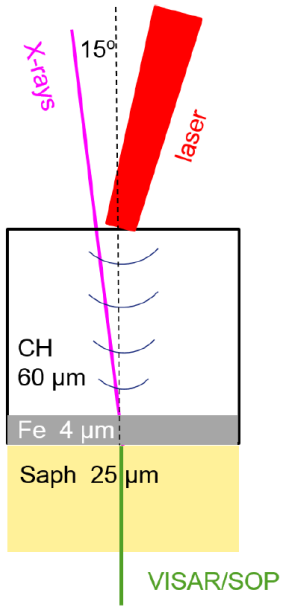

Figure 1.9: Schematics of the focusing and angular disposition of the drive laser with respect to the X-rays. Both are tilted by 15° with respect to the normal of the target. The laser is focused onto the ablator which will produce the shock wave while the X-rays are focused onto the sample. VISAR laser is instead reflecting on the back surface of the sample (or window)[23].

2 | High Power Laser at ID24

In this chapter all the features of the High Power Laser are presented, following the description provided in the Technical Design Report redacted by the staff of ID24 in 2019 [23].
A dedicated Clean Room hosts the entire drive laser setup and properly designed chicane transports the beam into the adjacent Experimental Hutch in which it is focused onto the samples in the Interaction Chamber.

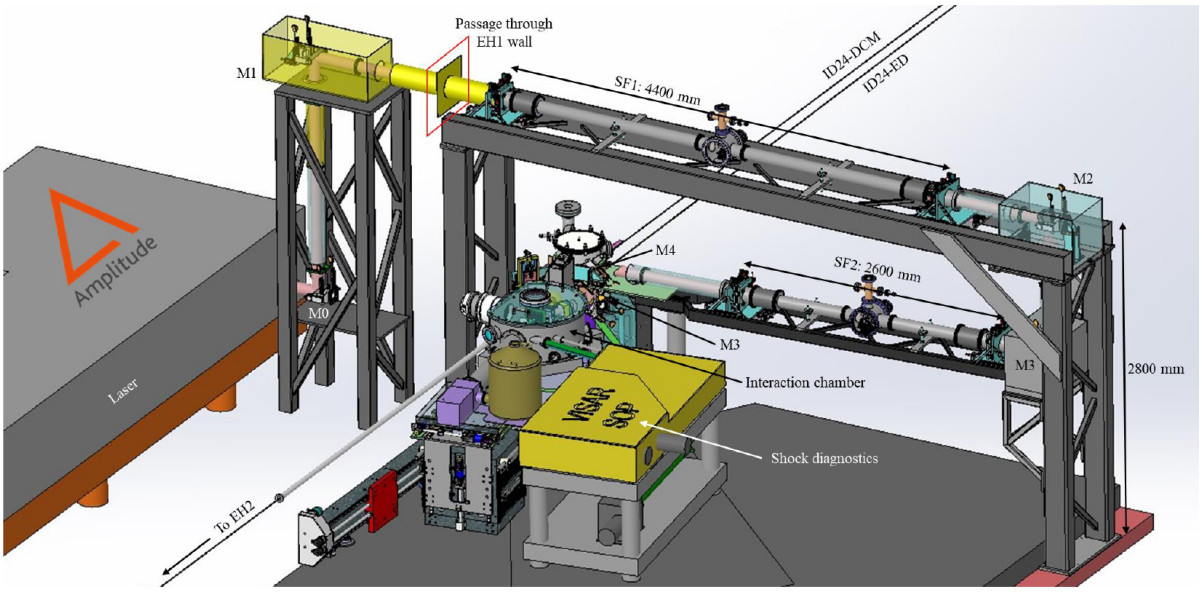

Figure 2.1: CAD view of the Experimental Hutch of ID24-ED. The drive laser leaves the Clean Room through the Laser Transport and follows the path to the Interaction Chamber. [23]

2.1. Laser description

In a separated Front - End ModBox from ©iXblue (Besançon, France) the continuous wave seed source is generated by a Distributed FeedBack laser. The radiation wavelength is 1053 nm, main optical transition of Nd^{3+} ions as we will see in detail in next chapter.

From the continuous wave fiber laser, nanosecond pulses are cropped by acousto-optic and electro-optic modulators in series and modulated by the RF signal as explained in the next section.
For the later stages, ©Amplitude Technologies company built and delivered the laser system composed by two separated setups: the Intrepid Front End and the Premiumlite100. The pulse in fiber leaving the ModBox enters first the Intrepid, which amplifies up to 15 J and then the P100 that increase the pulse energy to 100 J.

Temporal duration of the pulses can be varied from a minimum of 2 ns to a maximum of 15 ns. For every duration the temporal intensity profile of the seed must be regulated to compensate the distortions in the amplification processes. Target temporal profile is top hat with rising edge smaller than 0.25 ns and contrast between the plateau and the pre-edge larger than 10^5. With the 15 ns configuration there is also the possibility to produce a compression ramp following a t^3 law which have the property to ramp compress the sample along along a different thermodynamic path that a conventional single shock (see Fig.1.4. The repetition rate for full-energy pulses is of 1 shot every 10 seconds. This quite long time among each pulse allows for a proper heat dissipation of the amplifiers and a correct restoring of the initial lasing conditions, guaranteeing the desired stability. However, for alignment operation a low energy CW laser at the same wavelength is used.

Spatial profile is circular with top hat shape. In the latest stages the diameter is around 80 mm enclosing 90% of the energy with super gaussian profile of order ≥ 8. The beam is then focused onto the sample with three possible spot-sizes of 100, 250 and 500 μm. It is worth mentioning that the spatial profile at the exit of the ModBox fiber is gaussian and the supergaussian profile is reached with the help of both an apodizer and the gain spatial distribution within the amplifiers. Indeed, the pumping of the gain media is more efficient in the borders of the rods with respect to the centre thus the gain experienced by the wings of the pulse is higher than the one experienced by the central part. Pictures below show the beam intensity distribution at the exit of the ModBox fiber and the impact taken with infrared burnpaper at the output of the P100.

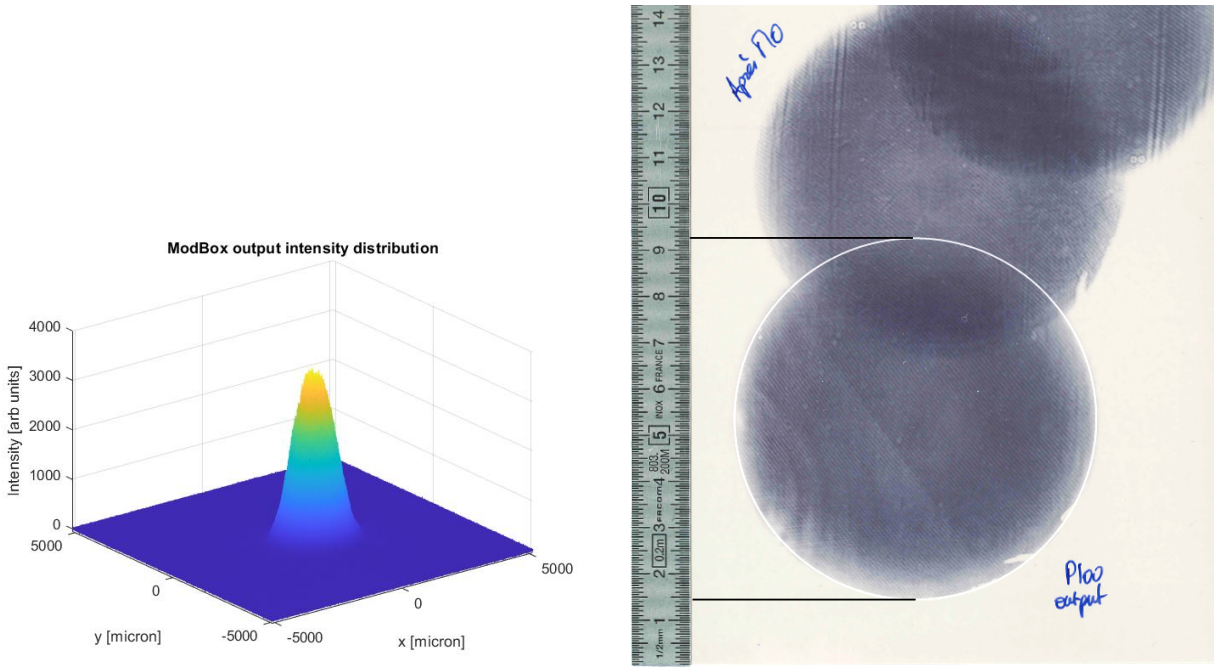

a) b)

Figure 2.2: a) Intensity distribution recorded with infrared camera out of the ModBox. b) Intensity distribution out of the P100

The amplification of laser pulses will be widely discussed in the next chapter. Here we will only say that Nd:Glass rods and slabs are employed in the amplification stages and the pumping process is performed through flash lamps. To be brief we could say that flash lamps are gas discharge lamps that are able to produce high energy white pulses in the μs range. When high voltages are applied to the edges of the tube containing the noble gas, an electrical discharge excites the gas atoms or molecules which in turn emit light in a broad spectral range. As a result, part of the spectral components is not absorbed, and part of the absorbed components is not converted into stimulated emission but relaxes thermally, heating the medium. The emission is also spatially dispersed, thus properly designed reflectors are needed in order to address the largest possible amount of light towards the gain medium. This can affect the distribution of the population inversion produced inside the medium, modifying as we will see, the amplification.
These aspects contribute to low conversion efficiency from the flash lamp power to laser power (few percent [27]), and affect the repetition rate due to time needed for cooling. Better efficiency could be achieved with the use of *diode laser pumping* which can be tuned to pump in a precise spectral region, increasing the conversion efficiency and reducing the thermal load. In our case, for Nd:Glass the pumping wavelength would be 808 nm, and the comparison between the flash lamp and laser diode emission spectrum is depicted in 3.2. Despite these and other advantages of diode lasers, flash lamps still

represent a robust, cheaper, and well known technology and their choice is more suitable for the HPLF case.
Another important characteristic is the **stability** of the produced pulses. The reproducibility in terms of energy, temporal and spatial profiles and pointing directions are key aspects for the drive laser. No measurements have been recorded for this scope up to now but from the Technical Design Report we read that both the energy and the intensity spatio-temporal profile were planned to have stability "better than 2% RMS for the 95% of the shots measured over 50 pulses at the maximum delivered energy at 1 shot every 10 minutes" [23].

The transport of the laser pulse from out of the P100 setup occurs in a dedicate chicane (see Fig.3.1) in which the beam is relay imaged twice before reaching the focusing lens. In these two positions a pin-hole under vacuum is placed in correspondence of the focal plane to filter out all parasitic focal spots generated by multiple reflections inside lenses. The lower arm of the transport structure is able to turn around its axle (M3 in the figure) in order to focus the beam at 15° onto the sample at every energy angle.

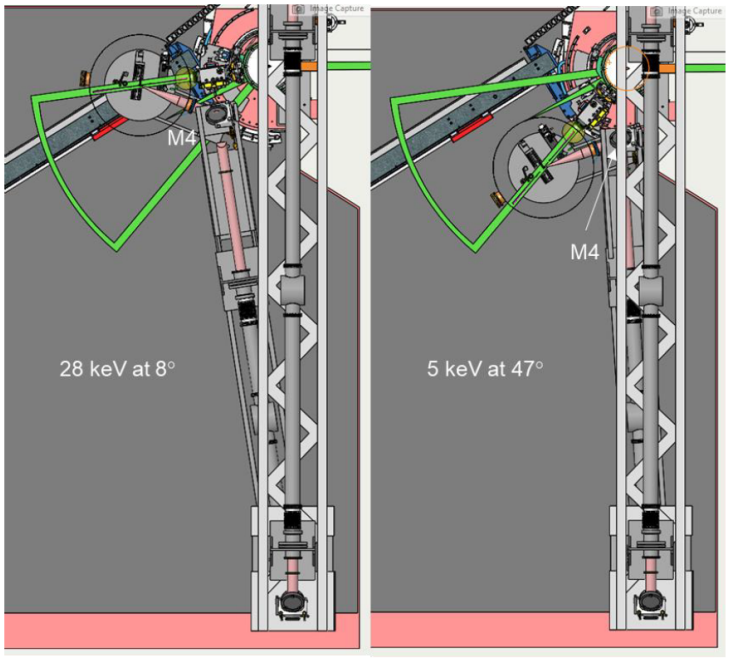

Figure 2.3: CAD view of the turning arm of the laser transport. The motion of both the Interaction Chamber and the laser transport allows the selection of the X-Rays energy range captured by the XH detector.

2.1.1. Smoothing by Spectral Dispersion

Here we present a particular technique used to reduce the temporal coherence of the laser beam in order to have, when coupled to a proper phase plate, a more homogeneous focal spot at the level of the sample to be shocked. This method was invented in 1989 by Skupsky et al. [28] for the production of smooth and focused laser beam in high-power glass lasers fusion experiments. This is highly important to obtain spatially homogeneous and temporally constant compression on the sample. It includes a sin wave radio - frequency modulation of the phase of the beam produced in the ModBox, a diffraction grating (in our case in the Intrepid Front End) and a phase plate (in our case right before the last lens that focuses the beam onto the sample in the Interaction Chamber).
The sin wave modulation spreads the very narrow line spectrum of the laser over 2m+1 lines spaced by the modulation frequency.

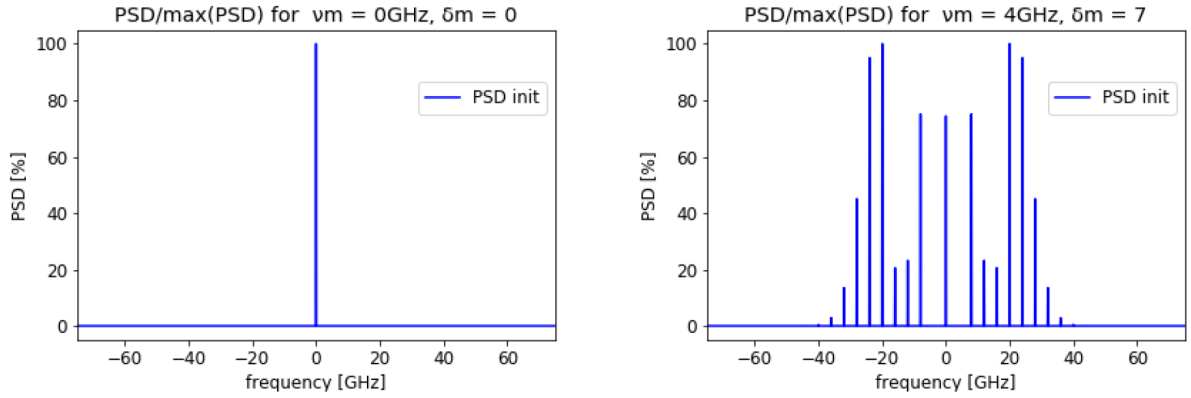

Figure 2.4: Normalized Power Spectral Densities of non-modulated laser line centered at ν_0 (*left*) and modulated one for 4GHz of modulation frequency and 7 rad of modulation depth (*right*). [23]

The larger spectrum of the laser pulse allows the diffraction grating to produce an *angular* dispersion. The wave vector is swept with the modulation frequency in many slightly tilted wave vectors positions that compose the laser pulse, that will thus look like diverged in a time integrated image. It is worth notice that with a modulation frequency of 5 GHz the duration of each sweeping is of 200 ps, thus way shorter than the duration of the whole pulse.

The main difference with a non modulated pulse, is that when this last pulse crosses the phase plate, a constant in time speckle pattern is produced at the focal plane. With an angular dispersed pulse instead this interference pattern is time varying according to the time varying wave vectors tilt. This allows a further smoothing of the focal spot.

It can be proved that the larger is the number of beamlets, the smoother *in space* is the focal spot. However, to increase the number of laser lines it is necessary to decrease the modulation frequency which, in turn, means increasing the interaction time of each specific speckle pattern with the sample. This on the other hand reduces the smoothing effect *in time*. In this case the lower limit on the modulation frequency is given by the plasma. Indeed, the duration of the interaction between each speckle pattern and the plasma which is produced must be shorter than the response time of the latter.

Another constraint on the modulation frequency and modulation depth is the emission bandwidth of amplifier. Indeed, if the frequency gain curve is too narrow around the central emission frequency, the modulated laser lines at higher and lower frequency will experience a smaller gain (gain narrowing). Fourier transforming the convolution of the gain bandwidth curve with the modulated laser frequency produces in time domain a sinusoidal modulation of the intensity of the pulse in time. In this way the frequency modulation appear in time domain as amplitude modulation. This last effect, that gets amplified through all the amplification stages, can be detrimental for the final pulse temporal profile and consequently for the shock.
To overcome this issue a wide emission bandwidth gain medium must be chosen. For this reason Nd:Glass has been chosen instead of Nd:YLF despite the higher thermal conductivity, i.e. better cooling, of the latter.

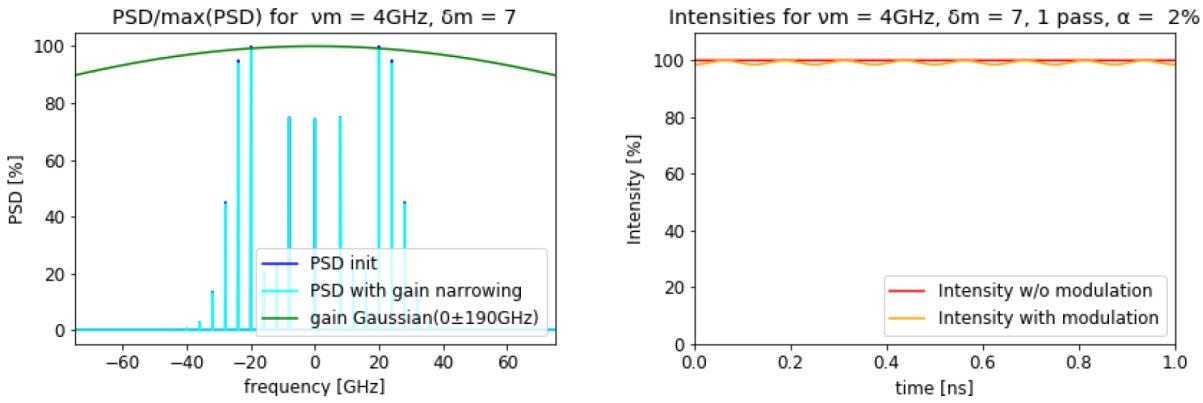

Figure 2.5: Example of FM - AM conversion using Nd:YLF as laser medium. Power Spectral Densities with the effect of not constant gain in frequency domain (*left*) and consequent amplitude modulation in time domain (*right*). Coefficient α represents the degree of AM for a single pass through the amplifier. [23]

Here below a picture of the focal spot is reported in both cases in which the SSD system is on and off. As we can observe, the smoothing occurs along one direction only. This is

indeed due to the fact the our SSD system operates only in one direction (1D-SSD, using one RF modulator and one diffraction grating).

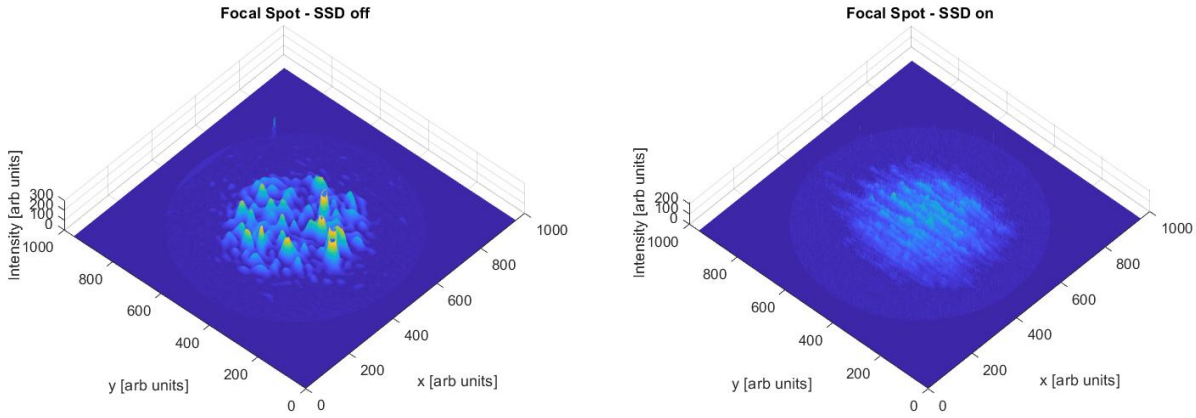

a) b)

Figure 2.6: a) Intensity distribution at the focal spot recorded without SSD system. b) Intensity distribution at the focal spot with the SSD on. The envelope is $\approx 250\mu m$ in diameter.

2.2. Laser diagnostic

In order to monitor all the parameters of the laser pulse that is going to produce the shock it is useful to install a diagnostic system that allows users to obtain information about the energy and the intensity temporal and spatial profile. In our case the main diagnostic workbench contains an energy meter, one Near Field camera, one Far Field camera and a fast photodiode and it is placed vertically on one side of the Interaction Chamber. It takes the leakage of one of the last mirrors and splits it into four parts directed towards the four detectors. The same setup is present also in other strategic positions inside the amplification chain and are useful to retrace the origin of any possible error.

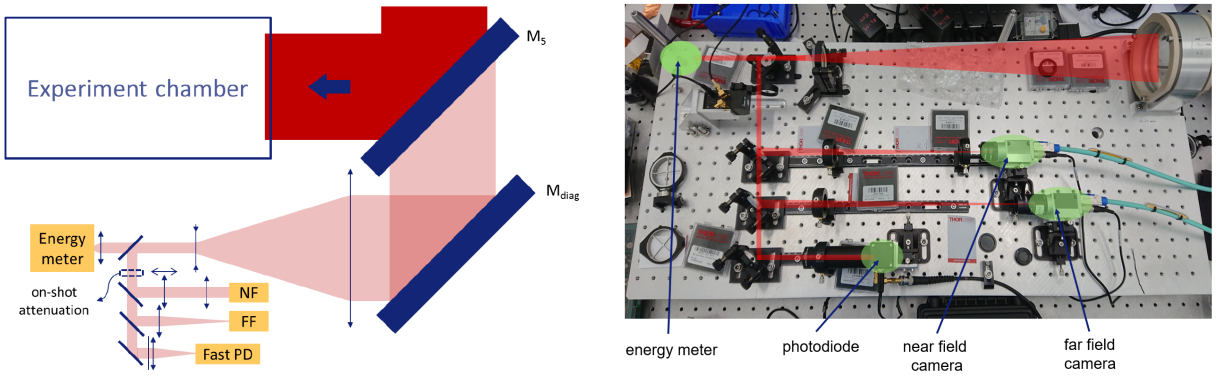

a) b)

Figure 2.7: a) Scheme of the laser diagnostic. b) Picture of the diagnostic during installation.

After a first demagnification the beam is collimated by a concave lens (f = -75mm) towards the first beamsplitter. A portion of the two is directed to the energy meter while the other gets splitted again to reach the others detectors. Various attenuators are placed in between the optics to protect detectors from damaging.

The energy meter is a high sensitivity pyroelectric detector that can self-trig on shot above a pre-defined threshold. It must be calibrated to properly relate the pulse energy and the energy of the fraction uptaken by the device.

The Near Field camera is a CCD camera that provides information on the shape of the beam and its intensity distribution in space. Two lenses are used to make the beam size match with the camera chip. It also gives information about the shape in image planes at specific positions inside the main beam path, and by moving the first lens it is possible to shift these image planes and monitor the spot in different positions.

The Far Field camera is instead placed in the focal plane of a positive lens thus "looks" at the spatial Fourier transform of the beam. Being the pulse shape supergaussian in the real space, we have that its Fourier transform, recorded by the camera, is the so called Airy disk whose size determines the intensity at the focus. This figure acts as a virtual alignment reference and an angular stability measurement [23]. It is curious to notice that when the SSD system is ON, the image captured by the camera is not a circle with

Airy pattern but a *line* made by the superposition of many displaced Airy disks. This indeed is a proof of the angular dispersion of the wave vector of the beam produced by the diffraction grating. To each different wave vector corresponds a different displaced Airy figure on the camera chip. However, being this temporal sweeping too fast for the camera response and being the SSD system one - dimensional, the resulting image produced is the superposition all the different disks in one line.

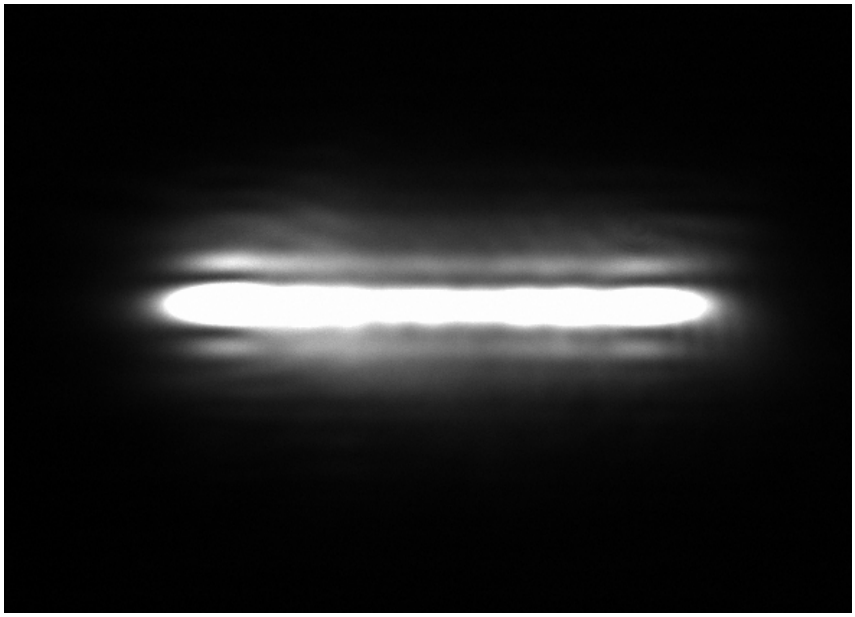

Figure 2.8: Picture taken by the FF camera with the SSD. A sharp horizontal line represents a correct alignment.

The fast photodiode measures the temporal profile of the laser pulse. It is a InGaAs PIN detector with fast rising time (70 ps). It will be mentioned widely in the next chapters.

All the information obtained from the diagnostic setup are of great importance to run shock simulations as close as possible to the experimental parameters.

3 | Laser Amplification and Seed Reconstruction Model

In this chapter, starting from the derivation of the laser rate equations, the process of amplification of a laser pulse during the passage through a gain medium is described. The validity of the assumptions made for the specific case of the drive laser is discussed in a dedicated section. Later, the phenomenon of saturation of the amplifier is explained along with its effect of distortion of the temporal profile of the pulse. This last topic is presented according to the analytic derivation proposed by Lee M. Frantz and John S. Nodvik in 1963.
Once the mechanism of amplification is explained for one and multiple passages through the gain medium, the computing model referred to the case of the HPLF together with all assumptions and approximations is presented.
Aim of the code is to reconstruct the pulse temporal shape and energy before the amplification stages once that a given output shape and energy are furnished.
Experimental measurements and simulation results are compared in the last section of the chapter.

3.1. Amplification by stimulated emission

The theory of pulse amplification by stimulated emission is based on the assumption of a monochromatic plane wave entering the gain medium with uniform intensity spatial profile.
The medium energy levels participating to absorption and emission of light are then modeled as a 4-level system where the radiative process takes place from the $|2\rangle$ state to the $|1\rangle$ state [Fig.3.1]. The populations of these levels are named N_i, expressed in $[\#electrons/cm^3]$, so that the *population inversion* is given when $N_2 > N_1$. This population inversion, in a 4-level system, is produced exploiting the fact that typically the lifetimes τ_3 and τ_1 of states $|3\rangle$ and $|1\rangle$ respectively, are smaller with respect to lifetime τ_2 of level $|2\rangle$. In this way pumping electrons up to level $|3\rangle$ will soon satisfy the population

inversion condition.

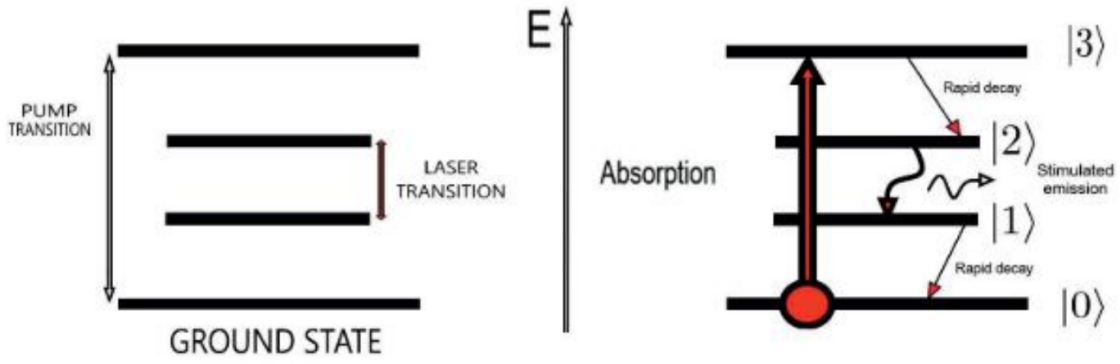

Figure 3.1: Scheme of a 4 levels gain medium from [27]

We now suppose that the input beam is a pulse of duration τ_p. Given that the propagation of the pulse occurs in the z direction from the position $z = 0$ coincident with the beginning of the gain medium and $z = L$ at the end of the material. Our aim is to retrieve the rate equations that describe, in a semiclassical approach, the evolution of the population $N(z, t)$ and the intensity of the pulse $I(z, t)$.
The approach is named semiclassical since it does not take into account the quantization of the fields, treating in a classical way, while on the other hand is based on purely quantistic phenomena such stimulated emission and absorption. In order to follow with the derivation the pulse duration τ_p must be assumed much larger than the lifetime of level $|1\rangle$. In this way we assume that during the passage of the pulse through the medium the population of level $|1\rangle$ is negligible since electrons rapidly decays, non-radiatively, towards the ground state. Such assumptions allows us to approximate the difference $N = N_2 - N_1 \approx N_2$.
The first rate equation for the population inversion takes the form of

$$\frac{\partial N}{\partial t} = R_p - WN - \frac{N}{\tau_2}$$

where R_p is the pumping rate, which can be set to zero during the passage of the pulse through the medium, W is the rate of stimulated emission and $-\frac{N}{\tau_2}$ is the spontaneous emission rate from the level $|2\rangle$. Also this last term can be neglected since the duration of the pulse is much smaller than the lifetime τ_2. To proceed, it is better to express the rate W as the product of the photon flux F and the *cross section* for simulated emission σ_s and recognize that the photon flux, which represents the number of photons per unit area, per unit time, is given by $F = \dfrac{I}{h\nu}$.

The term $-WN$ can be then rewritten as $-\frac{NI\sigma_s}{h\nu}$ where I is the intensity of the radiation, h is the Planck constant and ν is the central frequency of the pulse. At this point we can introduce the *saturation fluence* defined as $\Gamma_s = \frac{h\nu}{\sigma_s}$ and rewrite the equation as

$$\frac{\partial N}{\partial t} = -\frac{NI}{\Gamma_s} \tag{3.1}$$

However, to be precise, we should consider that the creation photons, given by the source term, must be the same as the rate of increase of ground state atoms, which in turn is the same as the rate of decrease of excited state atoms. For this reason, one should write *two* rate equations for the populations on the levels $|1\rangle$ and $|2\rangle$.

$$\frac{\partial N_1}{\partial t} = \frac{I(N_2 - N_1)}{\Gamma_s} \tag{3.2}$$

$$\frac{\partial N_2}{\partial t} = -\frac{I(N_2 - N_1)}{\Gamma_s} \tag{3.3}$$

with the constraint that the sum of the population must be constant $N_1 + N_2 = N_t = const.$ In this way we assumed that at the wavelength of the laser radiation, the cross section for the stimulated emission has the same value of the cross section of the absorption process. This assumption is validated from spectroscopic measurements [29]. This last consideration leads us to the final form of the first rate equation for the difference of the population inversion between the levels.

$$\frac{\partial N}{\partial t} = -2\frac{NI}{\Gamma_s} \tag{3.4}$$

To obtain the second rate equation we need to define the *instantaneous* intensity which differs from the *average* intensity by a factor $\frac{1}{2}$. The instantaneous intensity is directly proportional, through the speed of light c, to the energy density of the electromagnetic wave $\rho(z,t)$. An approach to derive the rate equation for the intensity is to consider an elemental volume dV inside the gain medium and to evaluate all the contributions to the change in time of the energy density. This can be summed up in three main terms:

1. Stimulated emission $\left(\frac{\partial \rho}{\partial t}\right)_1 = +\sigma_s N I(z,t)$

2. Absorption $\left(\frac{\partial \rho}{\partial t}\right)_2 = -\alpha I(z,t)$ where the absorption coefficient α has been introduced
3. Net photon flux that flows through the volume $\left(\frac{\partial \rho}{\partial t}\right)_3 = \frac{\partial I(z,t)}{\partial z}$

Summing all the contributions and exploiting the relation $I = c\rho$ we can write the second rate equation for the intensity of the pulse.

$$\frac{1}{c}\frac{\partial I}{\partial t} + \frac{\partial I}{\partial z} = \sigma_s N I - \alpha I \tag{3.5}$$

3.1.1. HPLF case

Before continuing with the solution of the rate equations it is worth evaluate the validity of the assumptions and approximations taken into account up to here in the specific case of the HPLF laser. The first assumption is to work with monochromatic plane waves. In reality plane waves do not exist since they are defined for an infinite time interval. Nevertheless a pulse duration of 4 - 15 ns at the central wavelength of 1053 nm like in our case is enough to guarantee a $\frac{\Delta\nu}{\nu}$ of the order of 10^{-7} thus allowing us to approximate it as a monochromatic plane wave in the calculations. This assumption holds also considering the SSD system, discussed in the previous chapter, due to which we have a broadening of around 0.22 nm in wavelength. However it must be said that in the simulation it has not been implemented the SSD effect of Amplitude Modulation since its modifications to the amplification are not so relevant.

The second assumption we made is to have a uniform intensity spatial profile so that we can consider, for symmetry, an homogeneous rate of stimulated emission and absorption through the medium, as long as the latter is homogeneously pumped in all directions. For what concern the laser in our case we saw that we have a circular spatial profile with top hat shape enclosing 90% of the energy with a supergaussian profile of order $N \geq 8$.
On the side of the gain medium not all the amplifiers have a symmetric pumping system, especially both $\Phi 5mm$ heads which are pumped by only one flash lamp. However the reflectors of the amplification heads are designed in a way that minimizes the non-homogeneous pumping. As first approximation for a 1D model we can assume a homogeneous distribution, also because further details could be introduced only knowing the shape of the reflectors, which in turn is an ©Amplitude trade secret.

The third assumption is to treat the gain medium as a 4-levels system with rapid non radiative decay between the two upper and two lower levels and radiative decay only between the intermediate levels. In our case the medium is a Nd:Glass and its energy levels can be evaluated from an analysis of the spectroscopic properties of the ion Nd^{3+} which has the ground electronic configuration of $4f^3$. To obtain the electronic energy levels of the ion at ground state one should consider the multi-electron Hamiltonian [30]:

$$H = H_{H-like} + H_{Coulomb} + H_{SO} + H_{CF}$$

Here the hydrogen-like term contains the sum over n electrons of the kinetic and effective potential operators, the Coulomb term is a repulsive term considering the electron - electron interaction, the third term considers the spin-orbit interaction and the last term accounts for the crystal field interaction of the neodymium ions in the glass matrix. While the first contribution is the most important in terms of magnitude the others are way smaller so that can be treated as perturbations. The removal of degeneracy due to perturbations leads the final spectrum of energies to have levels depicted in Fig. 3.2.
Even if, at first sight, it might not look like a 4 levels system, we can notice that the spacing in energy among the states above $^4F_{3/2}$ state below the flash lamp curve is small and comparable with the phonon energy of the glass matrix [30]. This allows the system to rapidly relax in a non-radiative way down to the $^4F_{3/2}$ state. From here the energy gap to the next lower level is too big for the same multi-phonon relaxation process and therefore the radiative decay dominates. The latter process is not as fast as the former so that in the end the population of electrons in the $^4F_{3/2}$ state is larger with respect to the $^4I_{11/2}$ state where still a fast phonon mediated relaxation process takes place. It is worth mentioning at this point that the phonon mediated non - radiative processes are responsible for the conversion of the optical pump energy into *heat*. This is one of the main reasons why repetition rate in glassy matrix lasers are kept low. Glass indeed shows poor thermal conductivity, i.e. poor heat dissipation.
C. Bibeau and S.A. Payne in [31] report lifetimes in the order of 250-450 ps for the $^4I_{11/2}$ to $^4I_{9/2}$ decay and similar values for $^4G_{7/2}$ to $^4F_{3/2}$ state, while the radiative lifetime reported in [30] for $^4F_{3/2}$ state is of the order of 360 μs.
These last quantities allows us to verify that the assumption of 4-levels system with $\tau_1, \tau_3 \ll \tau_p \ll \tau_2$ and $N_2 - N_1 \approx N_2$ are completely satisfied for the 10 ns pulse of our laser.

The last important assumption we did was considering that the rate of pumping R_p is negligible, meaning that the variation in time of the pumping process during the stimu-

lated emission caused by the passage of the laser pulse is almost zero. In practice, this assumption is valid since we know that the time interval between the maximum peak of the flash lamps fluorescence curve and the passage of the laser pulse is around 100 μs, when most of the population has been already inverted and, in the the timescale of the laser pulse, the variation in time of the flash light fluorescence is negligible (see inset of Fig.3.8) meaning that no significant changes on the population inversion occur in that amount of time because of it.

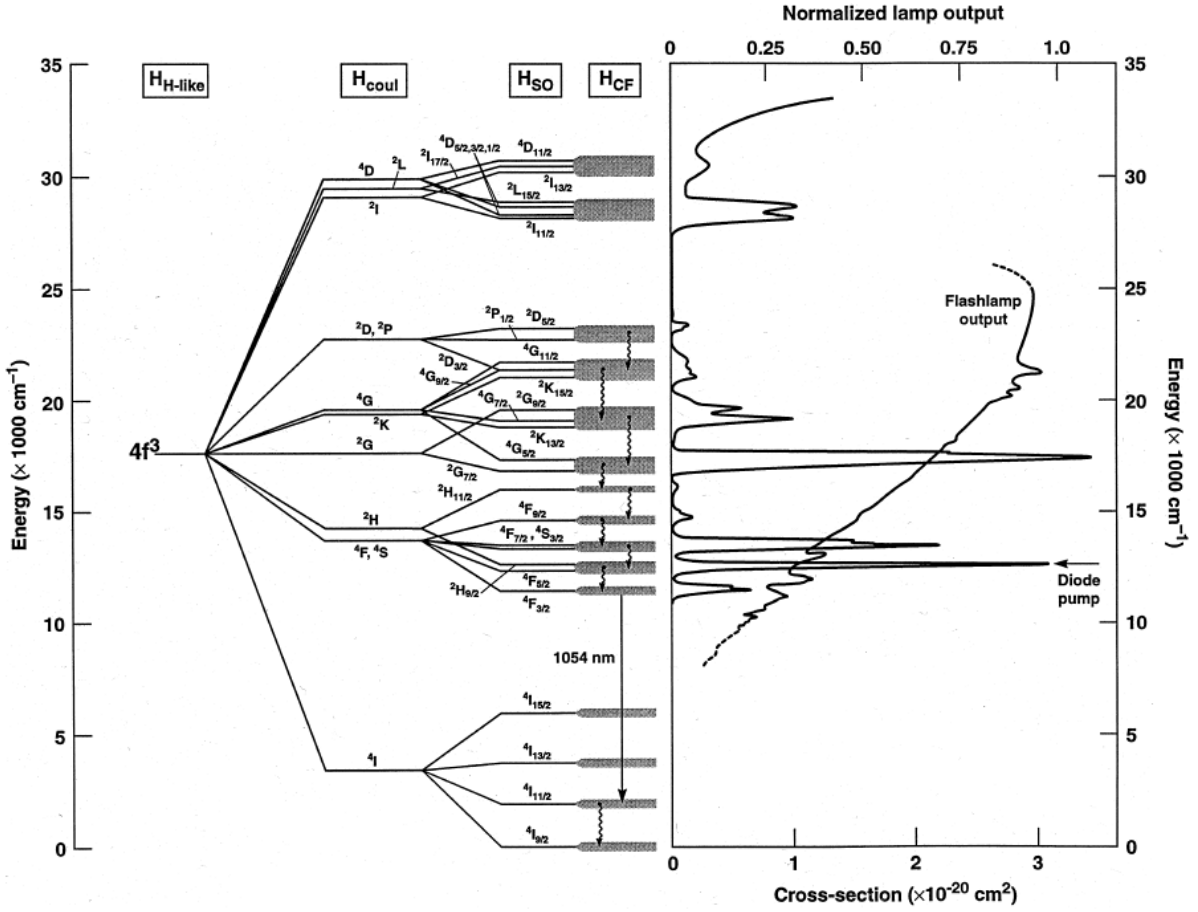

Figure 3.2: Scheme of energy levels of Nd^{3+} according to the Hamiltonian considered. "*The laser transition of interest (1053 nm) is from the metastable* $^4F_{3/2}$ *state to the* $^4I_{11/2}$ *terminal level. The wavy lines denote rapid non-radiative (multi-phonon) transitions. The energies shown are relative to the* $^4I_{9/2}$ *ground state*". On the right side the typical Xenon flash lamp output curve [30]

3.2. Frantz - Nodvik equations for pulse amplification

In this section, the results of the rate equations solutions are presented and discussed. Given the equations 3.4 and 3.5 one has to fix boundary conditions for the resolution:

- $N(t=0,z) = N_0(z)$ the pristine population inversion before the pulse passage is the one produced by the flash lamp
- $I(t, z=0) = I_0(t)$ for the pulse intensity before the amplification

Given these conditions one can prove, following the calculations provided in [32] that there is an analytical solution for the intensity $I(z,t)$ and the population inversion $N(z,t)$ given by

$$I(z,t) = \frac{I_0(t-\frac{z}{v})}{\left[1-\left[1-exp\left\{-\sigma_s\int_0^z N_0(z)dz\right\}\right]exp\left\{-\frac{2}{\Gamma_s}\int_{-\infty}^{t-\frac{z}{v}} I_0(t')dt'\right\}\right]} \tag{3.6}$$

$$N(z,t) = \frac{N_0(z)exp\left\{-\sigma_s\int_0^z N_0(z)dz\right\}}{\left[exp\left\{\frac{2}{\Gamma_s}\int_{-\infty}^{t-\frac{z}{v}} I_0(t')dt'\right\} + exp\left\{-\sigma_s\int_0^z N_0(z)dz\right\} - 1\right]} \tag{3.7}$$

These solutions are valid for an arbitrary input intensity profile and population inversion distribution that has been produced in a gain medium of length L, under the assumption that non-linear effects (like Raman-effect [33] and two-photons absorption [34]) do not affect the propagation of the pulse through the gain medium [35].

3.2.1. Analysis of the Frantz -Nodvik equations

Equation 3.6 describes the time and space dependent instantaneous intensity of the pulse in each point inside the gain medium along the direction of propagation. It does not provide information about the transverse directions because a cylindrical symmetry around the z is assumed in both the initial intensity and population inversion distribution. Equa-

tion 3.7 on the other hand, describes the population inversion distribution that is left in the medium when the pulse with intensity $I_0(z,t)$ has passed through. To better understand these equations one may introduce a new fundamental quantity named *fluence* of the pulse defined as

$$\Gamma(t) = \int_{-\infty}^{t} I_0(t')dt' \tag{3.8}$$

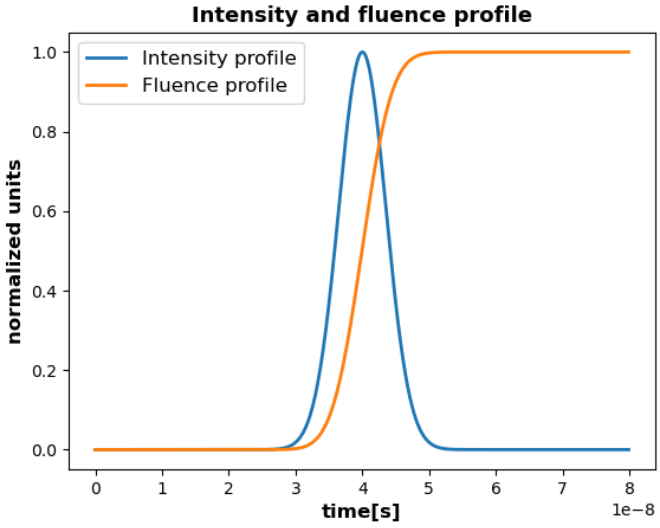

Figure 3.3: Intensity and Fluence temporal profile

This last quantity, measured in J/m^2, indicates the amount of pulse intensity that has passed in a certain region up to a time t. The ratio between the fluence of the pulse and the constant saturation fluence Γ_s of the medium is, in both equations, the exponent of an decaying exponential term at the denominator. This means that the more is the amount of pulse that has entered the gain medium, the closer to zero will be this exponential term. This term represents the level of saturation of the amplifier. For an unsaturated amplifier it is close to one. In the equation for the intensity 3.6 we see that the latter term is multiplying an expression of the form $1 - exp(-\sigma_s N_0^{tot}(z))$. Here for $N_0^{tot}(z)$ we intended the "cumulative" population inversion inside the medium before the passage of the pulse, obtained integrating the population inversion distribution along the length of the medium up to the position z. Usually, we are interested in the intensity at the end of the gain medium, so when $z = L$, thus the integral calculated for the whole length of the amplification medium. For the first passage after the flashing of the lamps, when we can consider a *uniform* distribution of $N_0(z)$, we have that $N_0^{tot}(L) = N_0(z)L$.

This last exponential term $exp(-\sigma_s N_0^{tot}(L))$ is often called *small signal gain* and represents the gain that a signal which is weak enough not to saturate the amplifier would experience. Indeed if we would have an unsaturated amplifier, i.e. $exp(-\frac{2\Gamma(t)}{\Gamma_s}) \approx 1$, we would end up with an exponential gain law for the intensity which is actually what experiences the leading edge of the pulse. Then with the passage of the pulse, the amplifier saturates and the overall gain experienced by the late temporal parts of the pulse decreases.

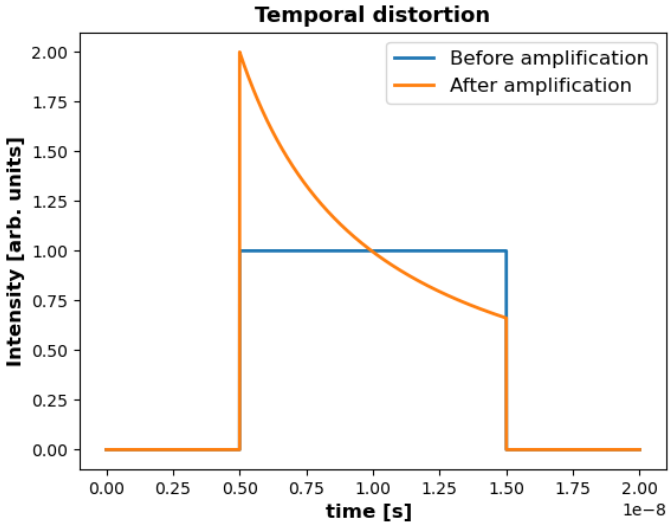

Figure 3.4: Temporal profile distortion induced by the saturation of the amplifier for a top hat initial shape. The leading edge experiences a gain exponentially dependent on the cross section and the total population inversion, while the trailing edge suffers a damped gain due to a depleted upper level.

It is important to notice that the overall gain is dependent only on the *total* population inversion and not on its *distribution* in the medium, and also there is no dependence on time for N_0 in 3.6. This is of particular relevance when we will need to consider several passages of the pulse through the medium after one single flash of the lamps, and we will ask ourselves which is the value of $N_0^{tot}(L)$ we should use.
Another thing we may comment is the change of the time variable that it is operated in the intensity fluence term. Here the intensity at time t depends on initial intensity and fluence at time $t - \frac{z}{v}$ where v is the light velocity in the medium. This transformation takes into account the travelling behaviour of the pulse along the propagation direction, hence, if we settle at the position $z = L$ where we look at one particular temporal portion of the pulse going out of the medium, this is dependent on the initial intensity and fluence

at the beginning of the gain medium $\frac{L}{v}$ seconds before, which is the time needed by that portion of intensity for passing through all the medium. Considerations about change of variable are important when we think about implementing the equations into a code for the simulation. In that case indeed we will not need the time transformation since we do not need to describe the travelling behaviour of the pulse. In other words the time variable becomes an *index* for the array of intensity and fluence, meaning, physically, that we place ourselves in a reference frame moving at the speed of light thus seeing the pulse not travelling.

About Eq.3.7 we said that it describes the population inversion distribution that is left in the medium after the passage of the pulse. Indeed, to have a better comprehension, we should assume a single passage of the laser pulse and observe it at a time $t = +\infty$. In this way we evaluate $N(z, +\infty)$, so when all the passage has already left the medium. The fluence we need to consider in this case is the *total* fluence of the input pulse which is something we already know before the amplification. If we now consider the single passage as the first after the flashing of the lamps, by looking at the equation, we can qualitatively say that as much as we increase the position z from 0 to L, $N(z, +\infty)$ decreases. Moreover, it is clear that the more intense is the incoming pulse, the more rapidly will be the decrease of N along the z direction.

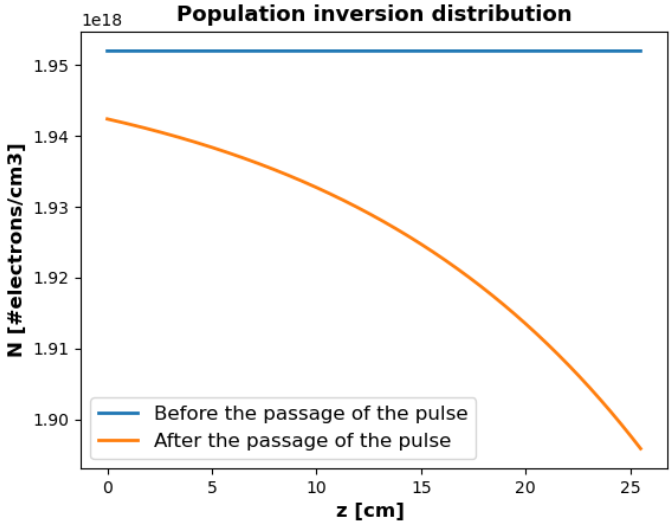

Figure 3.5: Population inversion distribution along a 25.5 cm long gain medium. The blue line represents the initial uniform distribution while the orange line is the one calculated after the passage of the pulse

We are now ready to write down equations 3.6 and 3.7 in the form we need for imple-

menting them into a code and simulate an arbitrary number of round-trips through the amplifier. The first thing to consider is the discretization of time and space which will turn integrals into summations. It is important the choice of the infinitesimal length and time interval small enough not to introduce errors and guarantee at the same time a reasonable simulation time. In our case a time interval of 10 ps has been chosen while for Δt larger than 50 ps unreliable edgy shapes were produced. Taking smaller time intervals slows down the computing time with no significant gain in accuracy.
Secondly, we want information on the amplified pulse intensity at the end of the gain medium, so we can remove the dependence on z from Eq.3.6 since from now on it will be not a variable but a parameter L. In the same way, we can remove the dependence on t from Eq.3.7 because, as we said before, in Eq.3.6 we need its dependence only on z.
In the case of multi-passage through the medium we thus need to have an initial population inversion distribution and an initial intensity temporal profile and starting from them we can calculate the output intensity profile and update the population inversion distribution we have to use for the next passage in the same medium. This last procedure is based on the assumption that the time elapsed from the exit of the pulse and its return back into the amplifier is much smaller than the fluorescence lifetime. This allows us to leave unchanged the population inversion distribution within that time. In all the cases of our interest this is a more than reasonable assumption because the already cited fluorescence time for Nd:Glass media is of the order 360 μs and in the worst case, in the Regenerative Amplifier, we leave the pulse in the cavity, running through the medium back and forth, for 922 ns.
With all these considerations in mind we can rewrite the Frantz-Nodvik equations:

$$I_t^{(p+1)} = \frac{I_t^{(p)}}{\left[1 - \left[1 - exp\left\{-\sigma \Delta z \sum_{z=0}^{L} N_z^{(p)}\right\}\right] exp\left\{-\frac{2}{\Gamma_s}\Delta t \sum_{t=0}^{t} I_t^{(p)}\right\}\right]} \tag{3.9}$$

$$N_z^{(p+1)} = \frac{N_z^{(p)} exp\left\{-\sigma \Delta z \sum_{z=0}^{z} N_z^{(p)}\right\}}{\left[exp\left\{\frac{2}{\Gamma_s}\Delta t \sum_{t=0}^{\tau_p} I_t^{(p)}\right\} + exp\left\{-\sigma \Delta z \sum_{z=0}^{z} N_z^{(p)}\right\} - 1\right]} \tag{3.10}$$

Here the superscript p indicates the p-th passage of the pulse through the medium while

the subscript t or z indicates the index of the position in the vector of intensity and population inversion distribution respectively and Δt and Δz represent the discrete time and length interval. The implementation of these equations with proper parameters and constants allows to simulate the amplification of whatever laser pulse given any kind of initial intensity temporal profile and population inversion distribution provided that limits of validity of assumptions are respected.

3.2.2. Small signal gain update

In this section, starting from the Eq.3.4 and Eq.3.6 we will derive another method to simulate multi-passage amplification which does not need to introduce Eq.3.7. This different approach has the advantage of not introducing discretization of the gain medium in space but on the other hand will not provide us any information about the population inversion distribution. We saw that, in Eq.3.6, if we look at the intensity for $z = L$ the small signal gain does not depend on z anymore. The idea is then to evaluate the small signal gain left in the medium after the passage of the pulse, and use it for the next passage, in a form that only requires the initial uniform population inversion distribution. The following derivation and discussion is mostly taken by Appendix D of [27].
This updated small signal gain is just the one that the initial pulse experienced *at the end* of the gain medium and we will call it G_{end}. It can be expressed as:

$$G_{end} = e^{\sigma_s N_{tot}} \tag{3.11}$$

where

$$N_{tot} = \int_0^L N(z)dz \tag{3.12}$$

At this point, we need the first rate equation 3.4 to find an expression of $N(z)$. By integrating Eq.3.4 we find:

$$ln\frac{N(+\infty, z)}{N(-\infty, z)} = -\int_{-\infty}^{+\infty} \frac{2I(z,t)}{\Gamma_s}dt \tag{3.13}$$

where $N(+\infty, z)$ is the population inversion distribution *after* the passage of the pulse,$N(z)$ and $N(-\infty, z)$ is the population inversion distribution *before* the passage of the pulse N_0. If we now recognise the fluence of the pulse at position z $\Gamma(z)$ in the integral we can rewrite:

$$N(z) = N_0 e^{-\frac{2\Gamma(z)}{\Gamma_s}} \tag{3.14}$$

At this point we have an expression for N_{tot}.

$$N_{tot} = \int_0^L N_0 e^{-\frac{2\Gamma(z)}{\Gamma_s}} dz \tag{3.15}$$

To continue with the calculation of the last integral we recall Eq.3.4 and we integrate all the terms in time.

$$\frac{1}{c}\int_{-\infty}^{+\infty} \frac{\partial I}{\partial t} dt + \int_{-\infty}^{+\infty} \frac{\partial I}{\partial z} dt = \int_{-\infty}^{+\infty} \sigma_s N I dt - \int_{-\infty}^{+\infty} \alpha I dt \tag{3.16}$$

Of this last equation we can evaluate each term separately. Beginning from the left side the first we see that it is equal to zero because it is an integral in dI and both $I(-\infty, z)$ and $I(+\infty, z) = 0$. Physically this implies the total absence of the pulse inside the medium before its arrival and after a very long time after its passage.
The second term can be rewritten as the partial derivative in space of the total fluence of the pulse: $\frac{\partial \Gamma(z)}{\partial z}$.
While the second term on the right, that accounts for absorption, can be neglected in first approximation since the medium is in a situation of inverted population, the first term on the right side can be easily obtained from the 3.4 and 3.14:

$$\int_{-\infty}^{+\infty} \frac{\partial N}{\partial t} dt = N(z) - N_0 = \int_{-\infty}^{+\infty} -\frac{2NI}{\Gamma_s} dt \tag{3.17}$$

If we substitute *N(z)* with 3.14 and rearrange the 3.17 we find that the first term on the right side of 3.16 is:

$$\int_{-\infty}^{+\infty} \sigma_s N I dt = \frac{1}{2}\sigma_s \Gamma_s N_0 \left(1 - e^{-\frac{2\Gamma(z)}{\Gamma_s}}\right) \tag{3.18}$$

Summing up all the results we can write a final equation for the derivative with respect to the direction of propagation of the fluence:

$$\frac{\partial \Gamma(z)}{\partial z} = \frac{1}{2}\sigma_s \Gamma_s N_0 \left(1 - e^{-\frac{2\Gamma(z)}{\Gamma_s}}\right) \tag{3.19}$$

This last result is useful if rearranged and substituted in 3.15 because it allows us to calculate N_{tot}.

$$N_{tot} = \int_0^L \Big(N_0 - \frac{2}{\sigma_s \Gamma_s} \frac{\partial \Gamma}{\partial z} \Big) dz \tag{3.20}$$

$$N_{tot} = N_0 L - \frac{2}{\sigma_s \Gamma_s} \Big[\Gamma(L) - \Gamma(0) \Big] \tag{3.21}$$

Where $\Gamma(L)$ is the *output* fluence Γ_{OUT} and $\Gamma(0)$ is the *input* fluence Γ_{IN}. So, to conclude the derivation, we need to substitute Eq.3.21 into 3.11 and to consider the *initial* small signal gain expression $G_0 = e^{\sigma_s N_0 L}$. The final expression for the small signal gain left into the medium will be:

$$G_{end} = G_0 e^{-\frac{2}{\Gamma_s}[\Gamma_{OUT} - \Gamma_{IN}]} \tag{3.22}$$

To simulate a multi-passage amplification it would be necessary to have an initial value for the population inversion distribution to evaluate the first passage amplification and from them calculate the remaining small signal gain of the medium to be used in the second passage amplification, and so on iteratively for the whole number of passages. Writing these couple of equation in a more suitable form for code implementation will provide us two expressions like these:

$$I_t^{(p+1)} = \frac{I_t^{(p)}}{\left[1 - \left[1 - G_p^{-1} \right] e^{-\frac{2\Gamma_p}{\Gamma_s}} \right]} \tag{3.23}$$

$$G_{p+1} = G_p e^{-\frac{2}{\Gamma_s}[\Gamma_{p+1} - \Gamma_p]} \tag{3.24}$$

The two approaches have been implemented separately and they provided the same results, as we will see later. If, on one side, this could have been rather expected from theory, on the other hand can be seen as a confirmation of the correctness of the simulations.

3.2.3. Temporal overlap inside the gain medium

With this last section about the theory of laser amplification we will deal with a direct consequence of most double pass amplifiers. In such configuration a mirror is placed after

the end of the gain crystal in the direction of propagation and a second amplification is exploited with the passage of the backward beam. Often, due to spatial length of the beam, there is the coexistence of the forward and backward propagating parts of the laser pulse inside the medium at the same time. This phenomenon is quite common in nanosecond pulses like the one we use. Indeed, making a rapid calculation, a 10 ns pulse will have a spatial length of around 3 metres in vacuum and 2 metres in glass media. This means that unless we have at least 1.5 metres between the end of the crystal and the mirror we will always have at least partial time overlap inside the crystal. The physical process governing the stimulated emission does not change however an appropriate model must consider that forward and backward beams simultaneously extract energy from the gain medium, modifying in this way the energy gain and the temporal profile distortion.

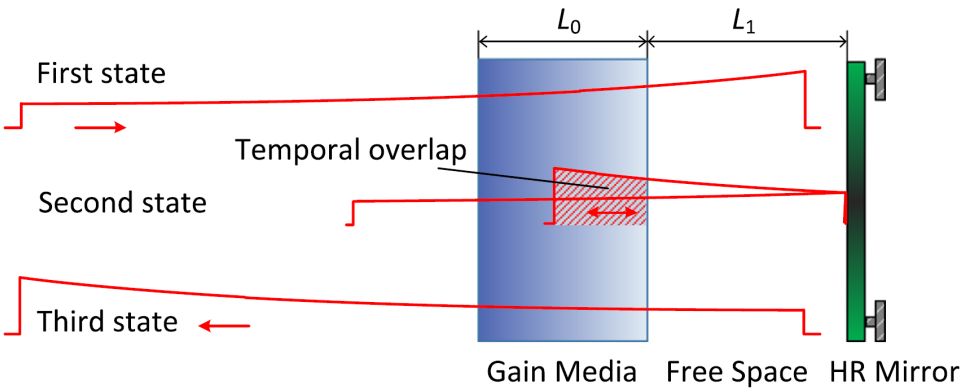

Figure 3.6: Schematic of temporal overlap. Credits to [36]

It is worth saying that temporal overlap modifies significantly amplification in case of high unsaturated gain and in case of high input fluence. In all the other cases the correction to the not-overlapping double passage case is negligible. However, it is interesting to understand how to approach the description of this phenomenon with equations. Before entering the formalism it must be precised that equations below are valid for the case in which the two counter propagating beams are *incoherent*. This is a quite common practice in order to avoid what is called Spatial Hole Burning (SHB) which would affect the amplification [37]. In HPLF chain, counter-propagating laser pulses have linear but orthogonal polarization in rods amplifiers and opposite circular polarization in disk amplifiers meaning that the incoherence requirement is satisfied.
Usually three cases are separated: 1) If the reflecting mirror is placed immediately after the gain medium we are in the Complete Temporal Overlap case (CTO). 2) If the distance between the medium and the mirror is not negligible we are in the Partial Temporal Over-

lap (PTO). 3) If the round trip time between the end of the medium and the mirror and back is more than the pulse duration there is No Temporal Overlap (NTO) and normal Frantz-Nodvik equations can be used. Analytical solution for the CTO case is confirmed by different studies [38], [39] while for PTO case numerical methods only are available [36] [40]. The solution proposed by [39] for the CTO assumes small extracted energy a consequent negligible modification of the population inversion distribution. In other words, the small signal gain must not vary significantly, meaning that the input fluence must be relatively small. Starting from the rate equations the authors derived a simple expression for the output intensity after the double pass in the crystal:

$$I_{out}^{back}(0,t) = \frac{I_{in}^{forw}(0, t - \frac{2z}{v})}{\left[1 - \left[1 - exp\left\{-2\sigma_s \int_0^z N_0(z)dz\right\}\right] exp\left\{-\frac{4}{\Gamma_s}\int_{-\infty}^{t-\frac{2z}{v}} I_{in}^{forw}(0,t')dt'\right\}\right]} \tag{3.25}$$

which differs from 3.6 for the factor 2 in the small signal gain and in the saturation term. The complete derivation is reported in the Appendix A of [36].
This last equation is slightly different from a normal double pass gain without overlap which would contain at denominator in the overall gain expression, the double product between the small signal gain and the saturation term. The residual population inversion distribution, or equivalently the small signal gain, are calculated in the same way from the evaluation of the output fluence.
Eq. 3.25 will be implemented with the same formalism of 3.9 for describing the amplification process in the disk amplifiers of HPLF. Such amplifiers have indeed a negligible spacing between the gain medium and the mirror and, despite the high energy, a relatively low input fluence due to the large spot size.
Regarding the PTO case its full description goes beyond the scope of this work, nevertheless it is interesting to have a rough idea of the process that can be divided in three steps: (1) The first portion of the input pulse passes through the medium with no overlap and normal amplification. (2) The same already amplified portion comes back into the amplifier while still the tail is passing for the first time. During this phase both portions of the pulse are gaining energy, so the medium will reach more rapidly the saturation.(3) All the pulse has already passed once, thus there is no more overlap and normal amplification is restored.

3.3. HPLF Amplification Chain modeling

As anticipated in the above section about the HPLF laser description, it is possible to divide the whole amplification setup in two different workbenches. The Front End, named Intrepid, and the Premiumlite 100. In the following subsections the amplification stages and substantial modifications to pulse temporal profile and energy are presented. Particular attention is paid to active elements which are responsible for changes in energy of the laser pulse. Passive elements such as lenses, mirrors, polarizers, wave-plates and so on have been considered ideal so that no losses are introduced by them. A rough estimation of the energy losses throughout the whole chain will be performed later with the comparison of simulation results with both temporal profile and energy experimental measurements.
Following quantities of energy, fluence and time are referred to a 10 nanosecond pulse. Slightly different values must be considered in case of smaller or larger pulse duration.

3.3.1. Intrepid Front End

In the following figure the Front-End pre-amplification is sketched.

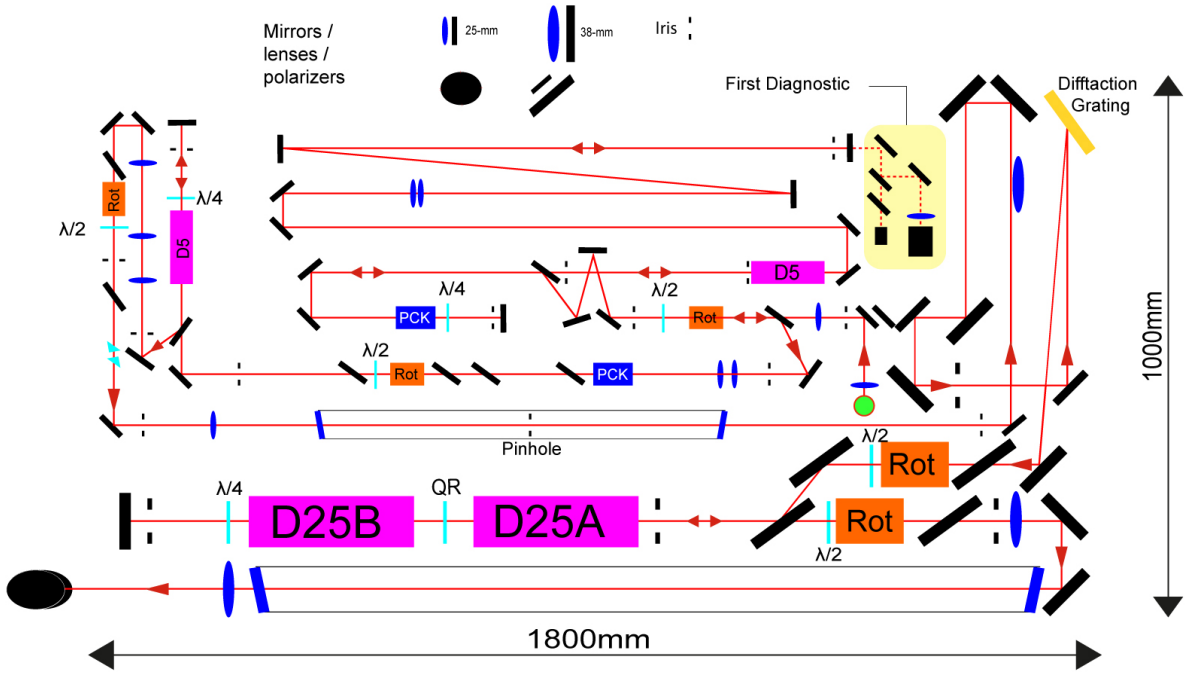

Figure 3.7: Schematic of Intrepid Front-End. The green dot represents the input. Light follows the red path through amplification modules D5 and D25, Pockels cells (PCK), Faraday rotator (Rot), mirrors, lenses and waveplates.

The beginning of the amplification chain is represented by the green dot in Figure 3.7. There, the ModBox fiber output enters the Front End with a temporal profile already shaped and an energy in the order of few nanojoules. The temporal shaping and the energy estimation at this stage will be discussed in dedicated sections. Entering the free space propagation the laser pulse is soon injected into the Regenerative Amplfier (RGA) cavity in which a 5 mm Nd:Glass rod amplifier is placed and it is reflected back and forth until the Pockels cell switches the polarization of the beam after a build-up time of 922 ns. Another important parameter is the beam diameter, needed to calculate the fluence of the pulse, which is $\approx$ 2.3 mm at this stage.
The measured energy at the output of the RGA is around 10 mJ and the spotsize is not varied.
A diagnostic system similar to the one described in the previous chapter, composed by an InGaAs fast photodiode, a NF Camera and a FF camera, uses the leakage of one of the mirrors of the RGA cavity to monitor the pulse status at this stage.
After few passive elements the pulse is injected into a double pass amplifier (D5 up left side in Fig. 3.7). This Nd:Glass rod has a diameter of 5mm and length of 11.5 cm as well as the RGA gain medium. Both of them also share the same pumping configuration and the same flash lamp trigger signal. Having a single flash lamp positioned parallel with respect to the glass rod, and exploiting only the reflectors system for an homogeneous illumination might affect the assumption of homogeneous pumping but, as already mentioned, no further information is available on the shape of the latter.
In both cases we have also partial temporal overlap since the distance between the edge of the crystals and the nearest back reflecting mirror is around 15 cm.
After the double pass in D5, an apodizer and the following pinhole in the vacuum tube perform a spatial filtering of the pulse spatial shape cutting the edges in the plane perpendicular to the direction of propagation and shaping the intensity distribution like a top hat profile. These passive elements reduce the energy of the pulse of a factor of 0.6 approximately.
Before entering the third amplification stage the beam encounters the diffraction grating mentioned above in the section describing the SSD system (section 2.1.1), and a Faraday rotator that acts on the polarization of the pulse. Then, two heads in series of 25 mm in diameter and 25.5 cm of length each amplify in double pass configuration the pulse up to 14 J.

Here the pumping is performed by 4 flash lamps symmetrically placed around each rod and triggered by a different electrical signal shifted in time with respect to the one used for the previous amplifiers. It is interesting to notice that the energy gain of the ampli-

fier can be tuned by shifting this timing. Indeed, the fluorescence curve in time, after a first maximum in intensity, has a long decaying tail in the hundreds of microsecond range, upon which the laser pulse passes at a certain position in time (see Fig.3.8) This means that, depending on the relative position in time of the laser pulse with respect to the maximum of the flashing curve, the population inversion "seen" by the pulse can be either higher or lower, which is translated in higher or lower gain experienced.

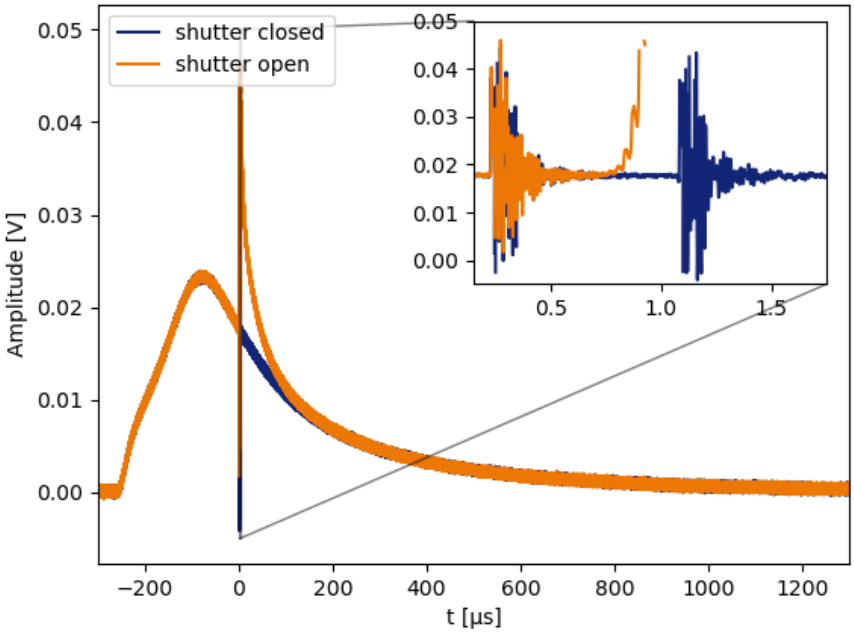

Figure 3.8: Temporal profile of the fluorescence curve of the flash lamps. With the shutter open, in the zoomed panel it is clear the saturation of the photodiode due to the laser pulse. Both curves show the presence of noise due to the switching of the RGA Pockels cell.

To reduce the fluence of the pulse, i.e. to avoid damaging of elements, the spotsize of the beam is increased up to 23 mm in diameter in this stage. About these two amplifiers, named together as D25, it is worth saying that heat production due to high energy flash lamps is significantly high with respect to the others amplifiers. An efficient cooling system and thermal effect compensation elements must be implemented in this case. For this reason a quartz rotator is placed in between to restore the linear polarization in the amplifiers.
Another remark concerning passive elements that we see in Fig.3.7 is that the presence of $\lambda/4$ waveplates placed between the end of gain media and back reflecting mirrors

guarantees at the same time an incoherent superposition of the forward and backward propagating beams and the distinction of the path of incoming or outgoing pulse at the level of the polarizer placed at the end of each multipassage stage.
Before leaving the Front End, the beam is relay-imaged with a second in-vacuum telescope. At these stages indeed energy is high enough to produce air ionization if confined in a small spot size.

Figure 3.9: Picture of Intrepid Front-End

3.3.2. Premiumlite 100

Once left the Front End, a periscope system lifts the pulse to the height needed to be injected into the last stages of amplification. The figure below schematizes the setup and the beam path in this section.

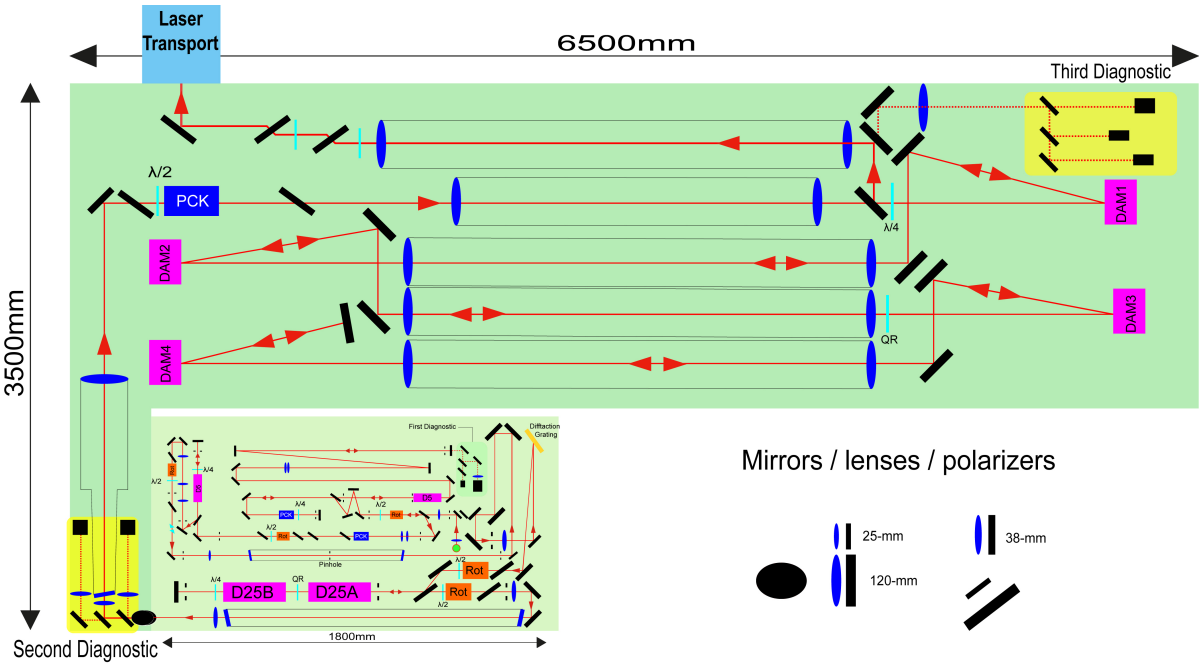

Figure 3.10: Schematic of the whole amplification chain

As depicted in Fig.3.10 a second diagnostic system is placed right after the Intrepid output while the main portion of the pulse undergoes a double increment of the spot-size up to 83 mm in diameter before being amplified by the first disk amplifier (DAM1 in the figure). Each disk amplifier has a diameter of 85 mm and a thickness of 3 centimetres. With such large area the fluence of the pulse is way lower than the saturation fluence of the gain medium so that it is far from saturation. This again, along with preventing damaging of optical elements and excessive thermal effect in the amplification, allows a lower distortion of the temporal profile.

The sequence of passages of the pulse is from double passage through DAM1 to double passage through DAM4 and back as depicted. Each double passage occurs with complete temporal overlap of the forward propagating beam with the backward propagating one. The output energy, after the all the passages, is theoretically of 100 J.

It is worth mentioning that the flashing of the lamps in this case is much more powerful and homogeneous with respect to the previous amplifiers. Indeed, 6 flash lamps, equally spaced behind each disk, are employed and their flash is anticipated by *simmers operation*, i.e. partial ionization of the lamps before the proper flashing, to facilitate the main high-current electrical discharge of the latter and prolong their lifetime.

Working with large spot-size implies also to increase the dimension of the setup since, to minimize aberrations, long distances are required to focus and to create images of the beam. Another technical issue when working in this energy regime is the cooling of the

amplifiers. In this case controlled water is used and its resistivity is kept high, with a particular deionising salt, to ensure electrical insulation and provide efficient cooling to the amplifier module.
Before leaving the Premiumlite 100 and travelling through the Laser Transport up to the Interaction Chamber, the leakage of one of the last mirrors is used in the third diagnostic system.

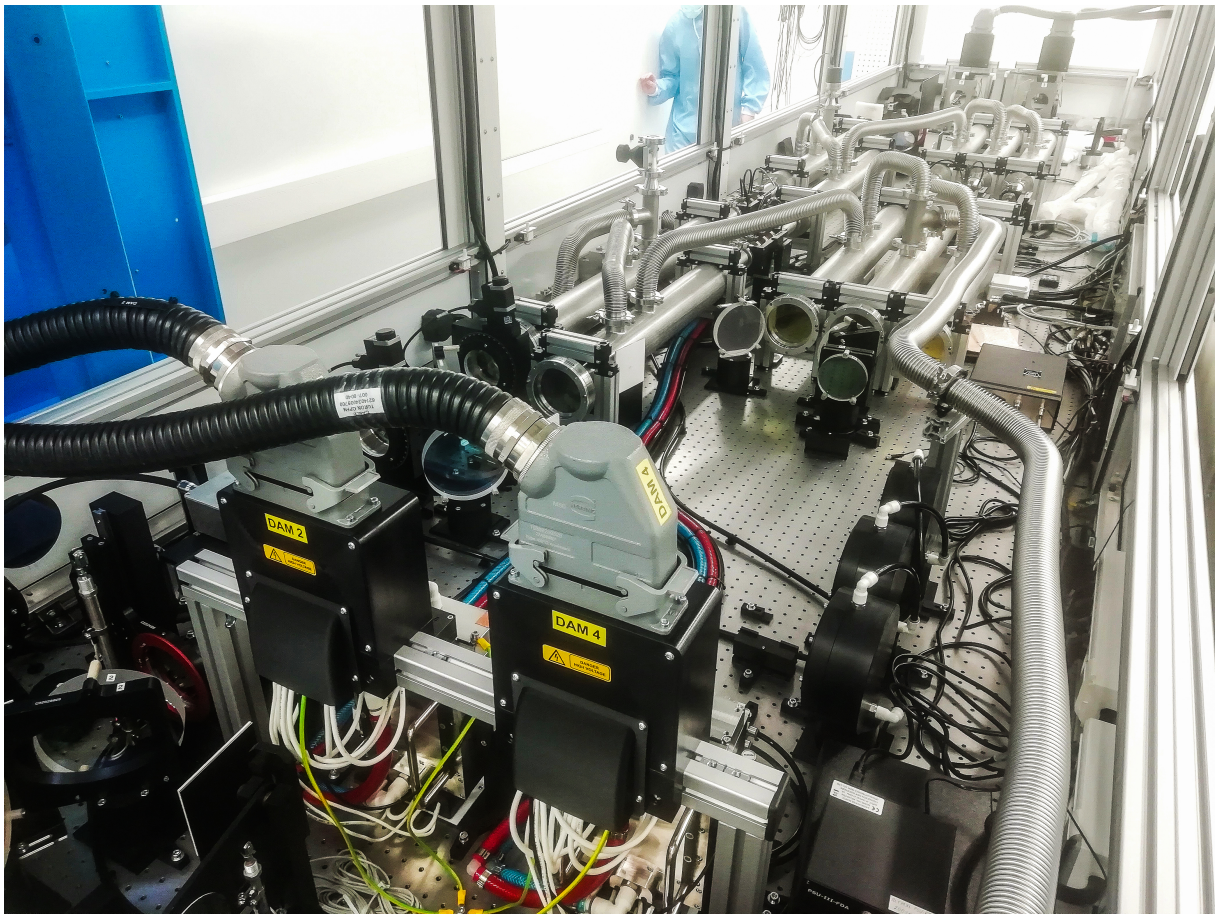

Figure 3.11: Picture of the Premiumlite 100 in the Clean Room

3.3.3. Summary of the Amplification Stages

In the following table all the stages that induce modification in both energy and temporal profile of the pulse are summarized with their relevant features.
Other important quantities that we find in Frantz - Nodvik equations are the stimulated emission cross section and the saturation fluence of the gain medium we are considering. Quite accurate values of them are found in [30] and are $\sigma_s = 3.6 \times 10^{-20}\ cm^2$ for the cross section and $\Gamma_s = 5.2\ J/cm^2$ for the saturation fluence.

	ModBox Output	RGA	D5	Apo + Sp. Filter	Change Spot-size	D25	Change Spot-size	DAMs
Energy	$\approx 10nJ$	10 mJ	150 mJ	89 mJ	89 mJ	14 J	14 J	100 J
Spot Size diameter	2.3 mm	2.3 mm	2.3 mm	2.3 mm	$2.3 \rightarrow 23mm$	23 mm	$23 \rightarrow 82.5mm$	82.5 mm
Fluence [J/cm2]	2.4e-7	0.24	3.61	2.17	0.02	3.36	0.26	1.87
Passages	-	27	2	1	-	1 in series and back	-	2 each and back
Ampl. length		11.5 cm	11.5 cm			25.5 cm each		$\approx 3cmeach$

Table 3.1: Scheme of the pulse amplification stages

With these last information we can compare the value of the fluence at each stage with the saturation fluence and make some comments on the temporal distortion. For example, being the fluence at the input and output of the RGA considerably smaller than the saturation fluence, we do not expect important distortions of the temporal shape. On the other hand, for the D5 and D25 stages the output fluence is in the same order of magnitude of Γ_s so we expect the amplifiers to go in saturation regime and consequent notable distortion of the temporal shape. With such high fluences also the partial temporal overlap occurring in both D5 and D25 might have a non negligible weight in the energy gain and the temporal profile distortion.
The only missing piece of information is the initial population inversion distribution that is build up in each gain medium at the beginning, before the pulse passage. This last quantity is almost impossible to know *a priori* since, as already mentioned, we should know the reflectors shape, the flash lamps pumping efficiency at each time of the fluorescence curve and the relation with their applied voltage, which is the only controllable variable, together with the delay of the flashing trigger. It has been thus necessary to estimate, assuming it constant, the initial population inversion distribution of each amplifier starting from the energy obtained at each stage. This last procedure allowed us to retrieve values in the order 10^{18} $electrons/cm^3$ which is consistent with the expected values found in literature.

3.4. Iterative method for seed reconstruction

Up to now all the passages that lead to the amplification and temporal distortion of the seed pulse have been discussed but the ultimate goal of this work was to retrieve the seed pulse shape that is needed in order to produce a pulse, at the end of the amplification chain, with the desired energy and temporal profile.
As briefly discussed in previous chapter, the output temporal profile of the drive laser is extremely important for dynamic pressure experiments since it determines the shock

characteristics and the thermodynamic quantities in the equation of state of the sample under analysis. Moreover, the target pulse shape might change according to the type of studies that are carried on, thus a versatile and reliable method for the seed reconstruction is needed.

The approach that has been chosen consists in running all the amplification chain backwards using as input pulse shape and energy the target ones. The equations used in the reconstruction process, for amplifiers, are the reversed form of 3.9 modified according to the particular stage considered while for fluence re scaling, simply the inverse of the re scaling factors used in the amplification process are employed.
The reversed form of 3.9 is:

$$I_t^{seed} = I_t^{target}\left[1 - \left[1 - exp\left\{-\sigma\Delta z \sum_{z=0}^{L} N_z^{seed}\right\}\right] exp\left\{-\frac{2}{\Gamma_s}\Delta t \sum_{t=0}^{t} I_t^{seed}\right\}\right] \tag{3.26}$$

Looking at 3.26 is immediately clear that it would impossible to know either the quantity of the population inversion distribution left by the unknown seed pulse either its fluence in time. To overcome this problem, the idea has been to save the vectors of N_z and Γ_t for each passage at each stage during the amplification forward process and to use them as parameters in the backward reconstruction. Indeed, even if they are not the exact ones they are a good enough starting point to produce a seed shape and energy closer to the right one. Iterating the whole procedure using always the same target pulse in the reconstruction process while updating the retrieved seed at each iteration, allows the convergence of the algorithm after few iterations. The convergence is monitored controlling the norm of the difference between the produced output intensity profile and the target one, and iterations are carried on until such norm is larger than a defined tolerance. The last retrieved seed will, at that point, have the right shape and energy to produce exactly the target shape and energy after all the amplification stages.

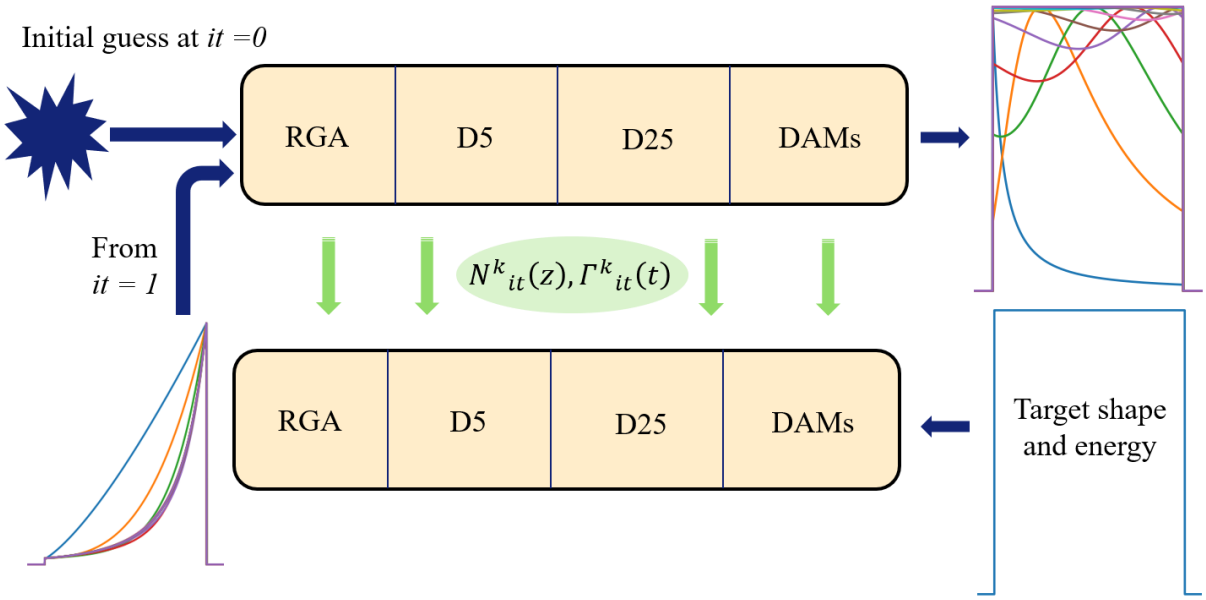

Figure 3.12: Schematics of the self - consistent iterative process adopted for the seed reconstruction. During the amplification the vectors of the population inversion distribution and the fluence are saved and then used as parameter in the reconstruction process. Using a squared initial guess convergence is reached after $\approx$ 15 iterations

This method allows the reconstruction of whatever seed pulse given the wanted target pulse starting from an initial input at choice. However, what is controlled by laser users is not the pulse shape at the ModBox output but only a digital input, i.e. a text file implemented in the latter apparatus. The text files contains numbers from 0 to 4095 which are the levels of the 12 bits DAC contained in the ModBox, responsible for the voltage applied, with time interval of 125 ps, to the electro-optic modulator devoted to pulse shaping. An attempt to model the behavior of this tool is discussed in the next chapter.

3.5. Experimental results and comparison with simulation

In this section the results of the simulation are presented. Firstly we will have a look at the temporal shapes obtained with the reconstructed seed, then we will only use the forward amplification part of the code using as input shape and energy, the ones measured and estimated respectively. The normalized temporal profile after each stage of amplification will be compared to the measured one.

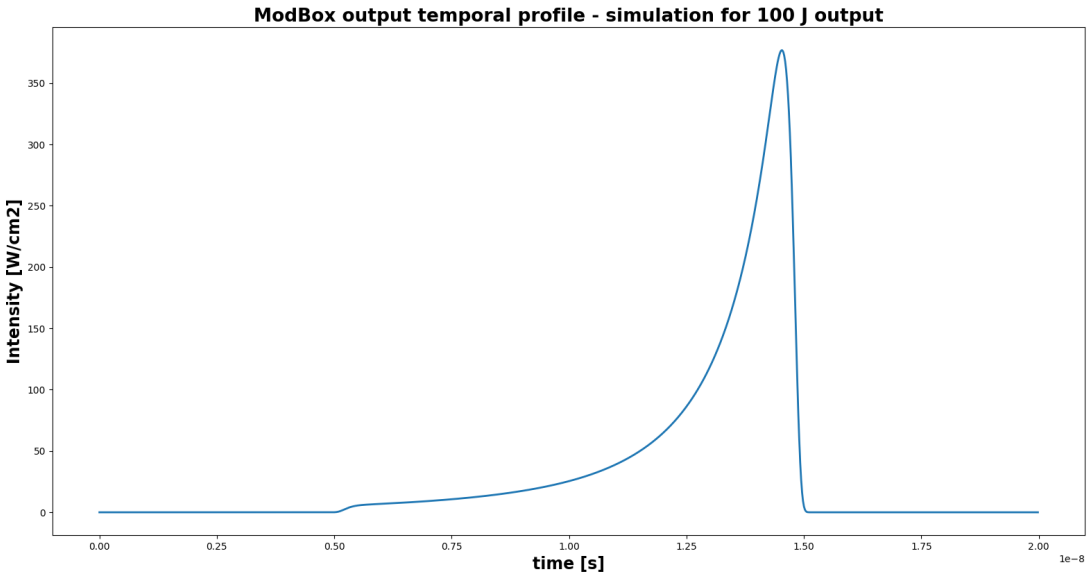

Figure 3.13: Reconstructed 10 nJ seed for a 100J top hat profile output

Figure 3.13 represents the intensity profile retrieved by the simulation given a 100 J top hat profile target. The target shape chosen is a super-gaussian pulse of order 35 since it optimizes, especially in the rising and falling edge, the fit with the measured shape. As expected we observe that the shape compensates the effect of saturation of the amplifier, reducing the amplitude on the leading edge and increasing it when moving to the trailing edge of the pulse.
Consequently, as depicted in Fig.3.14 , during all the amplification stages the target top hat is gradually established at the output.

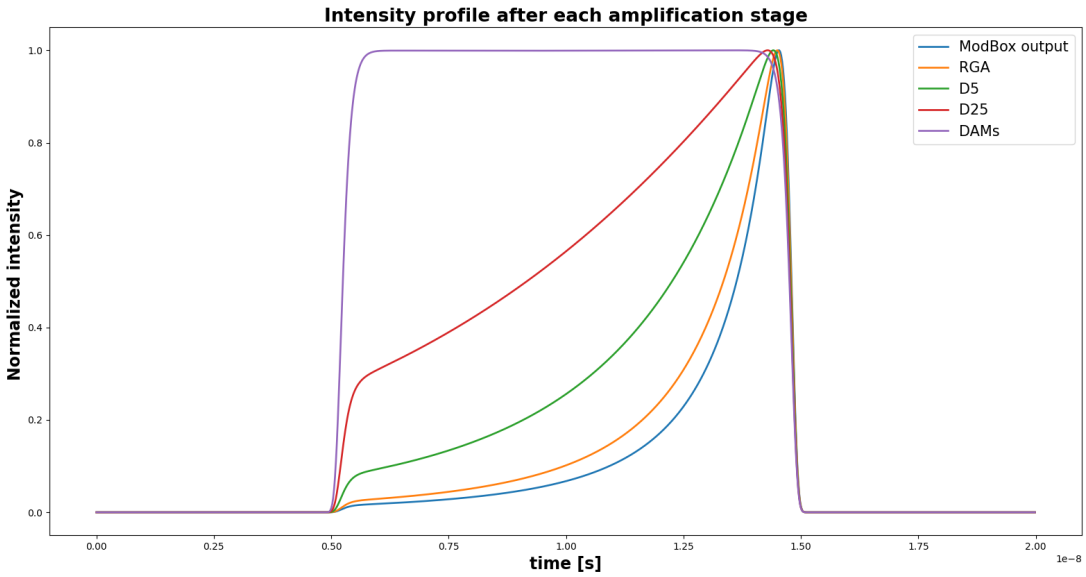

Figure 3.14: Gradual deformation of the intensity profile after each amplification stage

As expected, the RGA stage does not deform significantly the pulse shape while for others, in which higher levels of the saturation are reached due to higher pulse fluence, the temporal distortion is rather important.

An interesting comparison can be made between the simulated ModBox output and the measured one, which in principle should be very similar. The current temporal shape in use at HPLF has been designed to reach a squared shape of approximately 70 J at the DAMs output thus a proper comparison should be done setting such energy also in the simulation. Indeed, if we look at the picture below we see that there is a significant similarity between the two shapes, even if the simulation seems to compensate more the effect of gain saturation.

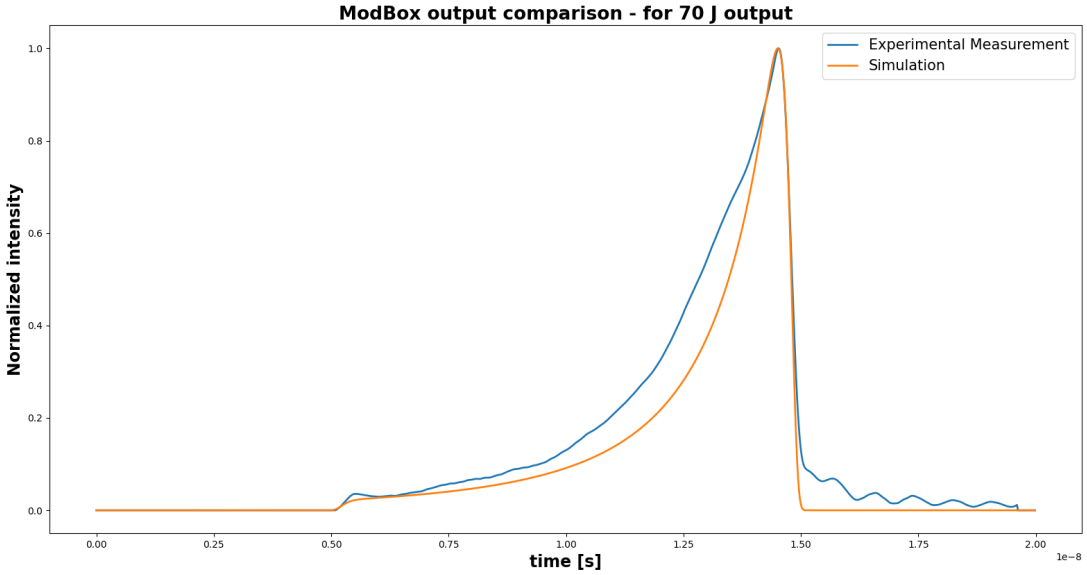

Figure 3.15: Comparison of real and simulated ModBox output for 70J top hat P100 output. A beveled form of the measurement is obtained with a proper smoothing of the experimental curve. Ripples after the falling edge of the pulse are due to the response of the photodiode.

Unfortunately there are not available measurements of the 70 J output for a comparison with a top hat profile, but, on the other hand, recordings of the intensity temporal profile after each amplifier have been taken, with the same ModBox output for 70 J, for a DAMs output of 55 J. In particular, gains of the RGA and D5 have not been modified while the gain of D25 has been decreased, shifting the trigger of the flash lamps, down to 8.8 J output and the DAMs as well, as anticipated, up to 55 J.
The comparison of these experimental measurements with the simulation temporal shapes obtained for such energies, using the simulated ModBox output shape for 70 J, gives rather disappointing results as we can see below.

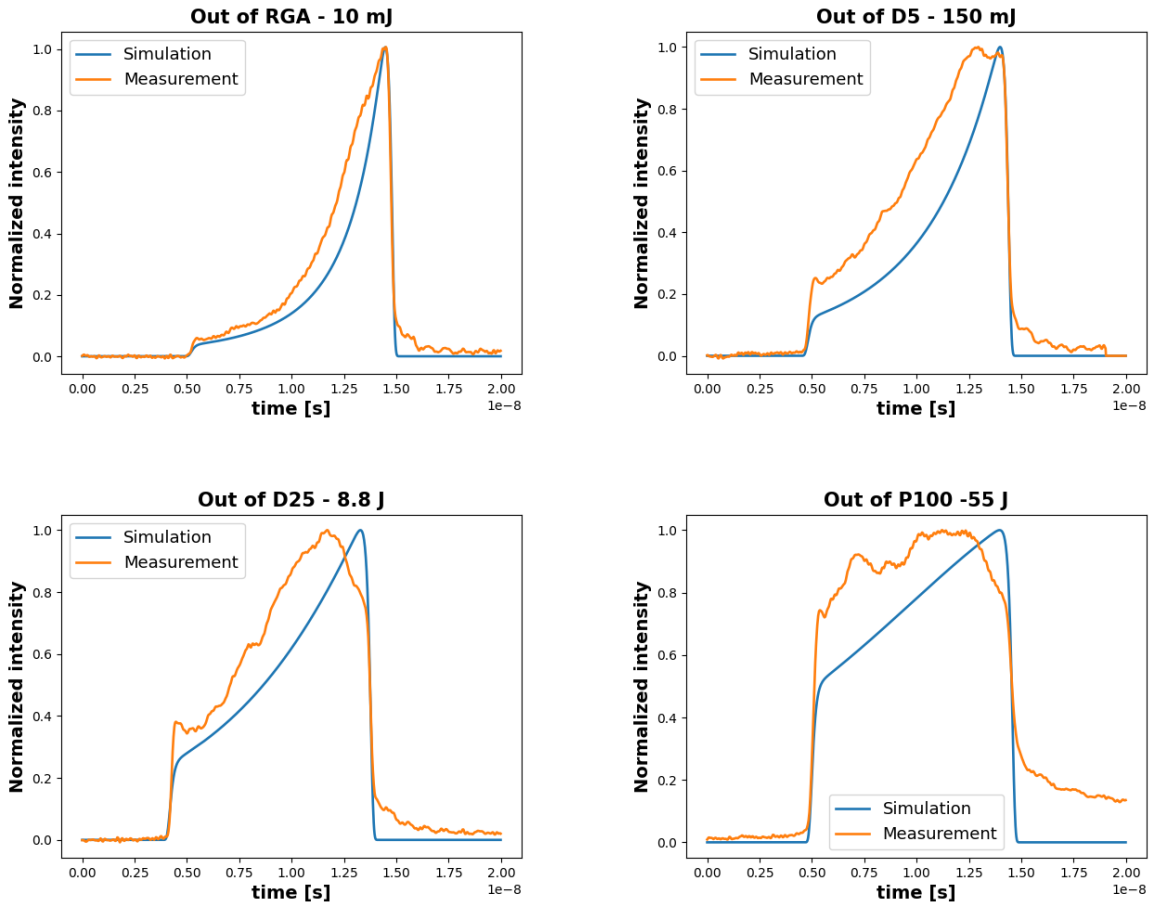

Figure 3.16: Comparison of simulation with experimental results using the simulated ModBox output for 70 J output energy

Beside the strong disagreement of the overall shape, it is curious to notice that for every stage the rising edge of the simulated curve remains lower in amplitude with respect to the measurement. This implies that the actual small signal gains of the amplifiers are higher than the ones used in the simulation, meaning that the pulse energy they could produce is *ideally* higher than the one measured and a significant amount of losses is present among or within each stage.

Typical losses sources are absorption and scattering processes of light in optical elements such as lenses, mirrors, wave-plates etc. In amplifiers also the mechanism of depolarization can contribute to decrease the energy of the pulse. Indeed, without entering into details, such distortion of the polarization of the beam in the amplifier does not allow the passage of the whole pulse through the polarizer out of the gain medium but only of that "portion" with the right component of the polarization.

Together with the increment of the initial population inversions to match the early step

of the pulse with the measurements, we could try to use the experimental temporal shape of the ModBox output in the simulation and look at the resulting shapes and energies in the other stages.
The results in this case are much more reassuring as we can see in the pictures below.

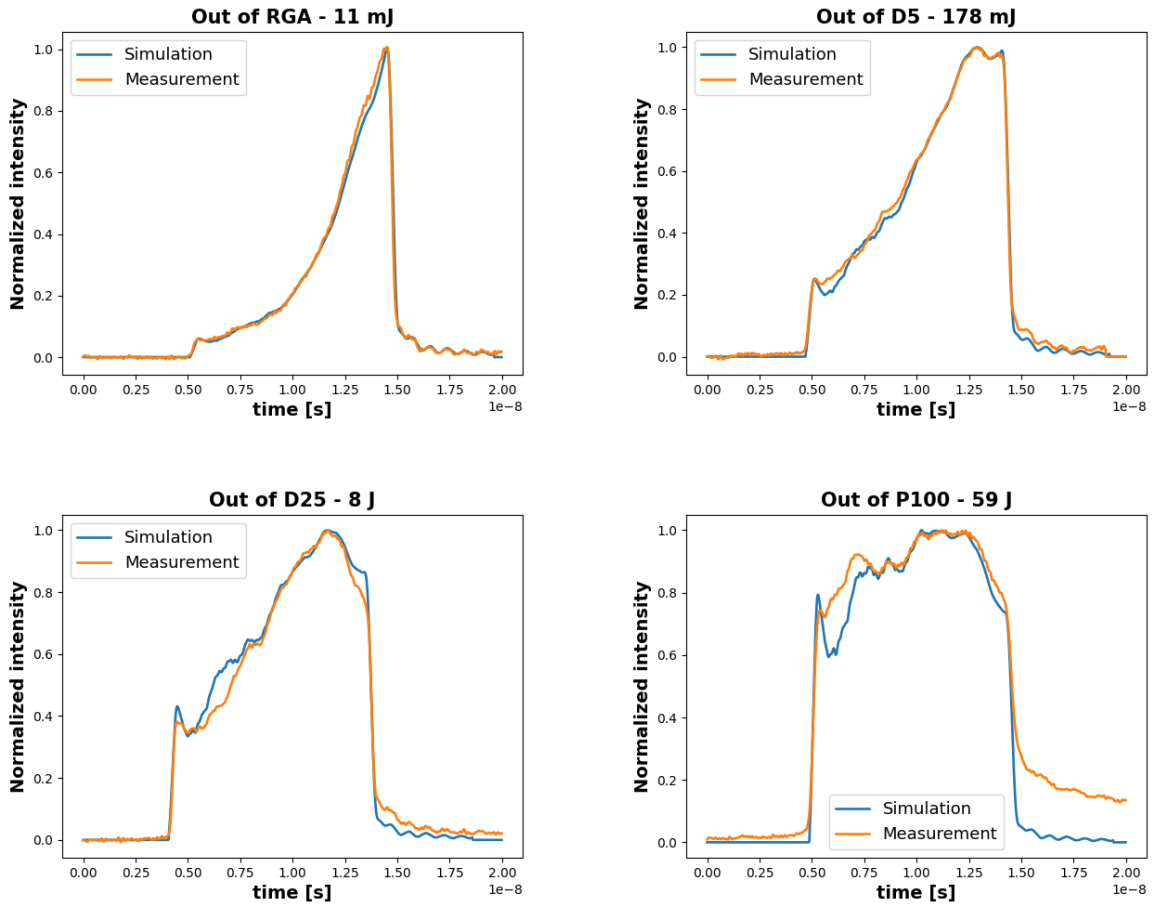

Figure 3.17: Comparison of simulation with experimental results using the measured ModBox output for 70 J output energy

On the side of the temporal *shape* the agreement is quite accurate for all the stages. For the RGA output the shapes are almost identical while as we move to further stages we loose more and more accuracy especially in the first temporal region where the amplification is higher due to low saturation. On the side of *energies* we actually see that the best fit is reached when the energies of the simulation (ideal) are higher than the measured ones. The only exception is the energy of the D25 pulse which conversely decreased. Nevertheless, the values of the losses are reasonable with what expected.
To conclude the presentation of experimental result it would be interesting to use as input for each amplification stage, the corresponding experimental measurement. This

will allow us to see if an improvement of the temporal shape and energy is found and also to check whether each amplifier has been modeled in the correct way or some other not accounted phenomena that modify the shape are taking place in a significant manner.

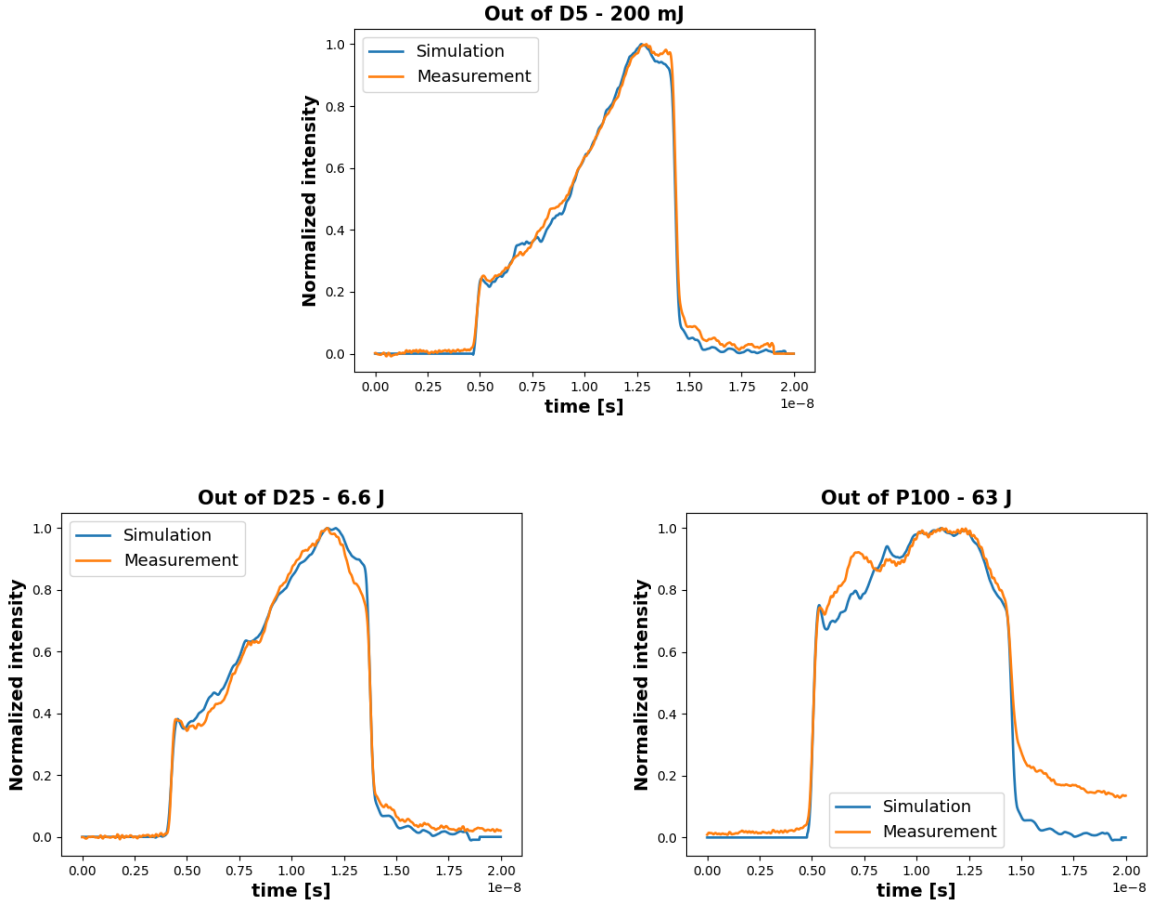

Figure 3.18: Comparison of simulation with experimental results using for each amplifier the measured profile as input.

From this last comparison we really see that the agreement in first temporal region improved. As anticipated the amplification in this portion of the pulse is dominated by the small signal gain since the saturation term is not important still. This means that the gain is almost exponential both for the optical signal and the noise or errors in the recording. For this reason it is always difficult to reach a good agreement in this region. Another possible source of disagreement is the partial temporal overlap that occurs in both D5 and D25 that has not been considered in the simulation.
Looking at the previous set of graphs it is curious to notice how less is amplified in reality the initial peak of the pulse. Indeed, following only the implemented Frantz - Nodvik equations that part of the pulse would be exponentially amplified at every passage through amplifiers. One possible explanation is that initial peak is actually cut out by the Pockels

cell transmittance temporal window. This last indeed does not have perfectly sharp edges but there is a transient time required to switch to zero to full transmittance of the light. We do not know this characteristic time but we can imagine it to be in the nanosecond range to produce such effect. A pictorial view of this phenomenon is given below.

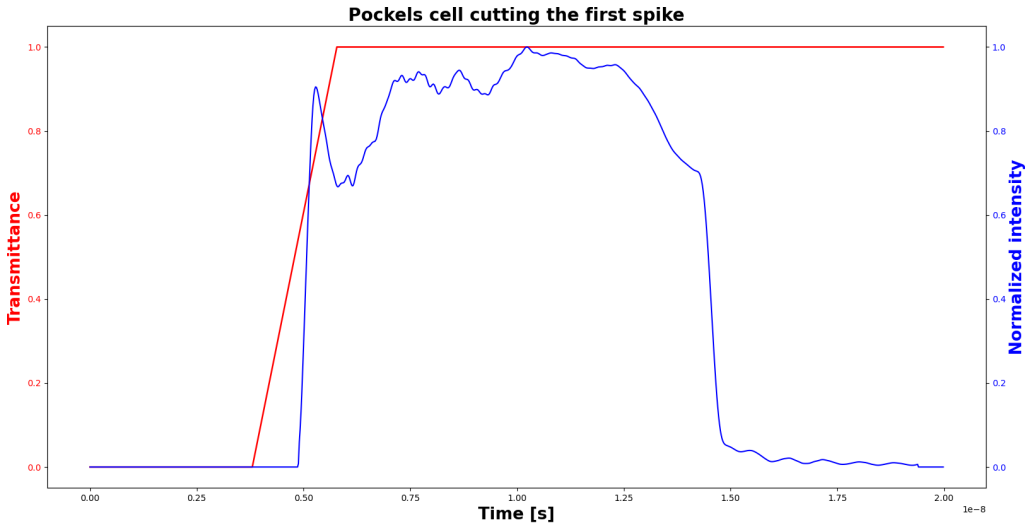

Figure 3.19: Possible effect that cuts the initial intensity spike.

A way to verify this assumption would be to modify the trigger time of the Pockels cell before D5 amplifier and the one in the P100 and look for modifications in the amplification of the pulse.
We can conclude that the simulation describes within a good degree of accuracy the whole amplification chain of HPLF meaning that assumptions and approximations considered were valid. It will be helpful for future updates of laser temporal shapes, especially to match specific users requests, and useful also to estimate the energy losses within the stages.

3.6. ©iXblue ModBox behaviour and modeling

As introduced in the last section, we know that to properly act on the seed pulse shape we need to understand how the temporal shape is physically produced inside the ModBox. What we know is that firstly an acousto-optic modulator cuts a 200 ns window out of the 5W (tunable) CW laser. The shape after this modulator will thus be still squared within a large width in time. The actual shape needed to compensate the saturation distortions is given by an electro-optic modulator which takes as input a vector of voltage levels from

0 to 4095 which are temporally spaced by 125 ps. That text file containing the voltage levels is the one we can modify according to the target shape we want.
To understand how to retrieve the voltage levels we need to know firstly how does an electro-optic intensity modulator work.

Usually, a birefringent material such as $LiNbO_3$ crystal is placed in one of the two arms of a Mach - Zehnder interferometer and a DC voltage + a RF signal is applied to it [41]. The peculiarity of these crystals is that they exhibit Pockels effect, i.e., in brief, a linear effect for which the refractive index of the medium changes linearly with the applied electric field.

$$n(E) = n - \frac{1}{2} r n^3 E \tag{3.27}$$

Where n is the refractive index, E is the applied electric field and r is the electro-optic coefficient.
Assuming a crystal of length L and thickness d transversely biased with respect to the propagation direction of the light, and placed in one arm only of the Mach - Zehnder interferometer, the phase difference between the light passing through the two arms is given by

$$\Delta\phi = -\frac{\pi r n^3 V L}{\lambda d} \tag{3.28}$$

where V is the applied voltage.
Usually this last expression is written in terms of a characteristic parameter of the modulator V_π which represents the voltage needed to produce a phase shift of π.

$$\Delta\phi = -\frac{\pi V}{V_\pi} \tag{3.29}$$

At the output of the interferometer we have re-conjunction of the two beams whose intensity is summed with the well known relation:

$$I_{out} = I_1 + I_2 cos(\Delta\phi) \tag{3.30}$$

To proceed we can consider equal amplitude of the intensity in both arms of the interferometer and the fact that only half of the output beam is collected at the exit. Thus, using also 3.29 and the bisection rule of cosine, we obtain

$$I_{out} = I_{in} cos^2\Big(-\frac{\pi V}{2V_\pi}\Big) \tag{3.31}$$

It is clear that, unless the electrical input stands in the very proximity of $V_\pi/2$, where the cosine squared has a linear trend, the modulation is highly non-linear, especially for low and high voltages.
From ©iXblue web page one can read that typical values of V_π are of few units of volts while no information are available on the digital to analog conversion of the input nor the non-modulated input intensity. Despite this lack of knowledge we could anyway try to evaluate the effect of this amplitude modulation to show the modification of the temporal shape.
In the best of the hypothesis the normalized modulated shape of the digital input is equal to the optical signal measured by the photodiode at the ModBox output.

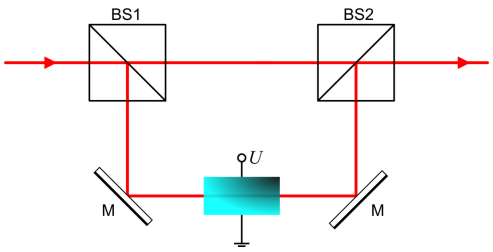

Figure 3.20: Mach-Zehnder modulator schematics. [42]

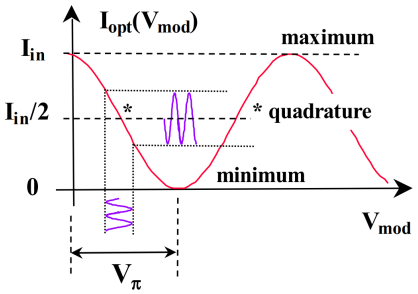

Figure 3.21: Optical intensity and applied voltage relation in a Mach-Zehnder modulator. [43]

Unfortunately, from what emerges in the below picture, we see that, even if a sensible improvement is produced with the cosine squared modulation, the pulse temporal profile at the output is still significantly different from the modulated digital input.

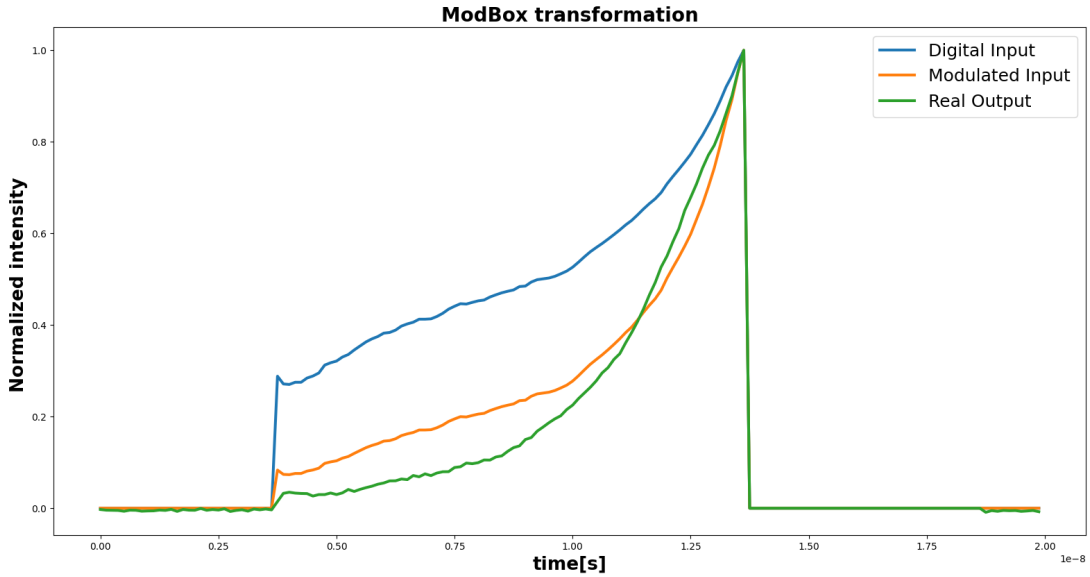

Figure 3.22: Different temporal shape of the digital input of the ModBox, modulated digital input and measured optical output

It must be said that the cosine squared modulation works well for temporal shapes that do not require fast rising edge but a smooth increment of the intensity is expected (see Fig. 3.23). For this reason one hypothesis that might explain the differences in Fig. 3.22 is that in addition to the electro - optic modulator, also an electronic circuit designed to ensure steep rising edges without overshoots and ripples must be implemented inside the ModBox. However, its modelling in absence of proper knowledge about its design and behaviour is way beyond the scope of this work.
A different approach based on neural networks and the analysis of several input/output profiles might be a solution for this problem but still it out of the aim of this thesis.

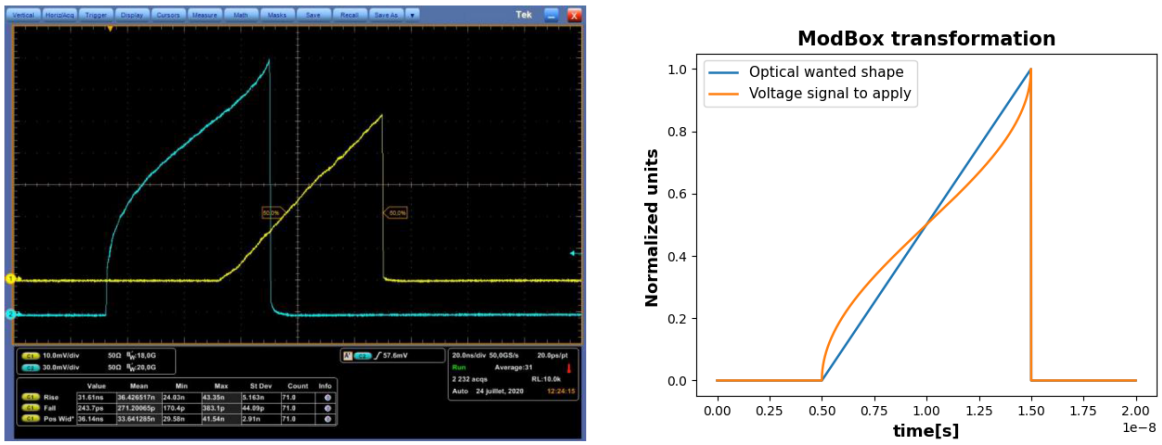

a) b)

Figure 3.23: a) Example of ramp-like optical temporal shape (yellow curve) obtained for the showed voltage digital input (blue curve) taken from (iXblue report, 2020)[44]. b) Voltage shape obtained reversing the cosine squared modulation for a ramp-like optical output

4 | ModBox output energy estimation from temporal measurements

In the previous chapter on laser amplification model we pointed out the necessity to know the energy of the ModBox output in order to set the parameters of the initial population inversions in the simulation. While for later stages we have proper energy meters which provide reliable measurement of the pulse energy, for the ModBox output no similar instrumentation, sensitive in the nanojoule scale, was available at the HPLF. To overcome this technical issue an alternative approach based on the available temporal measurements has been considered.
Indeed, considering the technical specifications of each element in the pipeline from the ModBox output fiber and the oscilloscope, it is possible to build a simple model that relates linearly the optical energy to the voltage read by the oscilloscope. Moreover, an estimation of both energy and unknown losses throughout the path of the signal can be done analysing different measurement recordings and fitting their results with the model.

4.1. Fiber-Oscilloscope Pipeline modeling

The conversion from optical power to electric signal occurs in the fast photodiode. Without entering into the theory of photodetectors we can say that one of the most important figures of merit of PN junction photodiodes is the *responsivity* which, expressed in A/W, indicates the photo-current I_{ph} generated by the incident optical power P_{in}. It takes into account the energy of the incoming photon and the quantum efficiency of the instrument. Responsivity R_λ is thus highly dependent on the wavelength of the light and its value is usually reported on photodiode specifications. The other important figure of merit is the bandwidth of the photodiode. To be brief as usual, it is in a way related to ability of the instrument to detect short variations of the optical power in time. In our case we

have an InGaAs PIN photodiode whose data-sheet (see [45]) reports a value of $R_\lambda = 0.72$ A/W at 1053 nm and 5 GHz of BW with rising time of 70 ps. Last piece of information allows us to neglect bandwidth considerations since strong temporal variations in our case are present only in the rising and falling edges with minimum intervals of the order of magnitude of the electro-optic modulator timescale (125 ps). Another reported parameter is the *dark current* which represents the current produced by the photodiode in absence of input light. This value, being around 1.5 nA in our case, can be neglected. Moreover, it has to be said that rising time response is optimized with $R_{load} = 50\ \Omega$ cable that connects the photodiode to the oscilloscope whose input impedance is 50 Ω as well. Electrical power losses across the cable are reported in its data-sheet and consist in $\beta =$ 2.6 dB for the 10 metres long one. With all this information and following the simple derivation in Appendix A we can write:

$$P_{in} = \frac{10^{\frac{\beta}{20}}}{R_\lambda R_{load}} V_{osc} \tag{4.1}$$

It is important to notice that the linear relation with the voltage is preserved as long as the optical power is not too high. In those cases the photodiode reaches saturation, in our case around 1.5 V, distorting the temporal profile in a non reliable shape. One now has to consider that the optical power impinging onto the active area of the photodiode might be only a fraction of the real optical power exiting the ModBox. This can be modeled by a factor γ expressed in dB that accounts for mismatch in the beam spot-size and active area. This in principle depends on the diameter of the core of the fiber used and on the distance between the end of the fiber and the sensing area. Equation 4.1 becomes thus

$$P_{in} = \frac{10^{\frac{\beta}{20}+\frac{\gamma}{10}}}{R_\lambda R_{load}} V_{osc} \tag{4.2}$$

To evaluate the energy of the pulse we should integrate in time the optical power and, on the other side the voltage read by the oscilloscope obtaining the anticipated linear relation between laser energy and voltages. An additional correction can be introduced accounting also for noise recorded by the oscilloscope. In first approximation it would be sufficient to integrate the baseline, before the pulse arrival, and subtract its portion from the integral signal. The new expression becomes then

$$E_{in} = \frac{10^{\frac{\beta}{20}+\frac{\gamma}{10}}}{R_\lambda R_{load}} \Big(\int_{\tau}^{\tau+\tau_p} V_{osc} dt - \frac{\tau_p}{\tau} \int_0^{\tau} n_{osc} dt \Big) \tag{4.3}$$

Now we reached an equation that links easily the recorded voltage to the energy of the pulse. However, we have one equation with two unknowns (energy and γ). A way to overcome this problem is to take the measurement with other configurations and add to that γ other sources of losses according to the configuration considered. This will allow us to to have a larger number of equations with respect to the number of unknowns which basically is an over-determined linear system easily solvable with a least squares approach.

4.2. Measurements and loss terms estimation

Different measurements of the ModBox output temporal profile have been recorded with additional fiber length in between the ModBox output fiber and the photodiode FC/PC connector. In this way the typical losses due to fiber-fiber connection, attenuation due to fiber length have been introduced. It must be said that the ModBox output fiber is different from the other type employed. This turns into different attenuation coefficients for the connectors. For simplicity in the notation we will call A the connection between ModBox fiber and "normal" fiber and B the connection between "normal" fibers. Another possible term of attenuation is the presence or not of the anti-reflective coating (AR) on the fiber input. In the end, calling α the losses in dB due to fiber-fiber connectors, we have

$$E_{in} = \frac{10^{\theta}}{R_{\lambda} R_{load}} \Big(\int_{\tau}^{\tau+\tau_p} V_{osc} dt - \frac{\tau_p}{\tau} \int_{0}^{\tau} n_{osc} dt \Big) \tag{4.4}$$

$$\theta = \frac{\beta}{20} + \frac{\gamma_A}{10} + \frac{\gamma_B}{10} + \frac{\alpha_A}{10} + \frac{\alpha_B}{10} + \frac{AR}{10} + \frac{\eta L}{10} \tag{4.5}$$

If now we manipulate the equation above separating the known and unknown variables we obtain

$$\gamma_A + \gamma_B + \alpha_A + \alpha_B + AR - 10log(E) = -10log\Big(\frac{\langle V \rangle}{R_{\lambda} R_{load}}\Big) - \frac{\beta}{2} - \eta L \tag{4.6}$$

Where with $\langle V \rangle$ is indicated the integral of the voltage read by the oscilloscope minus the portion of noise and ηL represents the losses due to the length L of the fiber with the attenuation factor declared by the producer. This last term is negligible for small distances considered in our measurements.

Before looking at the experimental measurement we should consider the fact that leaving the energy as unknown with the same coefficient for all the equations of the linear system we are building, will produce an *inconsistent* system because the rank of the matrix of the coefficient will be less than, and not equal to, the rank of its augmented matrix. In such cases a unique solution is not guaranteed. To get through this problem another type

of measurement has been considered, leading to the introduction of another unknown but providing on the other hand a known value of the energy given by the energy meter. In fact, the pulse has been intercepted before the D5 amplifier by a collimator that coupled from free space into fiber propagation of the beam and then the same system of fibers delivered the light to the photodiode. In this way we add a new source of losses coming from the free-space - fiber coupling (named ψ) and bring the logarithm of the energy on the right hand side together with another new known term accounting for the optical densities filters placed in front of the collimator to avoid damaging of the fiber and to leave the photodiode out of the saturation regime. The measurements that were recorded are summarized in the table below together with the coefficients of the unknowns.

	γ_A	γ_B	α_A	α_B	AR	10log(E)	ψ
MB fiber - PD	1	0	0	0	0	-1	0
MB fiber - 2m - PD	0	1	1	0	0	-1	0
MB fiber - 2m - no AR - PD	0	1	1	0	1	-1	0
MB fiber - 5m - PD	0	1	1	0	1	-1	0
MB fiber - (2+5)m - PD	0	1	1	1	1	-1	0
MB fiber - (2+2+5)m - PD	0	1	1	2	1	-1	0
MB fiber - (2+2+2+5)m - PD	0	1	1	3	1	-1	0
collimator - (2+2+2+5)m - PD	0	1	0	3	1	0	1

Table 4.1: Table of the coefficients of the unknown parameters for the different measurement configurations

A first remark on the above table is that the coefficient for the absence of AR coating is 1 in the case of 2m long fiber is employed switching input and output pins and in the cases in which 5m long fiber is used since not equipped with AR coating.
A second comment on the measurements is that 6 measurements with the same configuration have been taken and then averaged to have a better estimation. The variation of the time integrated voltage among these takes, translated in dB is at maximum 0.6 dB. This result will be compared with the residuals of the least squares solution.

The vector b of the known parameters is

$$b = \begin{pmatrix} -10log\left(\frac{\langle V_1\rangle}{R_\lambda R_{load}}\right) - \frac{\beta}{2} \\ -10log\left(\frac{\langle V_2\rangle}{R_\lambda R_{load}}\right) - \frac{\beta}{2} \\ -10log\left(\frac{\langle V_3\rangle}{R_\lambda R_{load}}\right) - \frac{\beta}{2} \\ -10log\left(\frac{\langle V_4\rangle}{R_\lambda R_{load}}\right) - \frac{\beta}{2} \\ -10log\left(\frac{\langle V_5\rangle}{R_\lambda R_{load}}\right) - \frac{\beta}{2} \\ -10log\left(\frac{\langle V_6\rangle}{R_\lambda R_{load}}\right) - \frac{\beta}{2} \\ -10log\left(\frac{\langle V_7\rangle}{R_\lambda R_{load}}\right) - \frac{\beta}{2} \\ -10log\left(\frac{\langle V_8\rangle}{R_\lambda R_{load}}\right) - \frac{\beta}{2} + 10log(3.1mJ) - 70 \end{pmatrix}$$

where we clearly see in the last row the term for the energy (3.1 mJ measured) and the attenuation due to the optical density filters. The last source of attenuation is considered at the wavelength of the radiation.

We are now ready to write the over-determined linear system in the form $\underline{\underline{\mathbf{A}}}\ \underline{\mathbf{x}} = \underline{\mathbf{b}}$.

$$\begin{pmatrix} 1 & 0 & 0 & 0 & 0 & -1 & 0 \\ 0 & 1 & 1 & 0 & 0 & -1 & 0 \\ 0 & 1 & 1 & 0 & 1 & -1 & 0 \\ 0 & 1 & 1 & 0 & 1 & -1 & 0 \\ 0 & 1 & 1 & 1 & 1 & -1 & 0 \\ 0 & 1 & 1 & 2 & 1 & -1 & 0 \\ 0 & 1 & 1 & 3 & 1 & -1 & 0 \\ 0 & 1 & 0 & 3 & 1 & 0 & 1 \end{pmatrix} \begin{pmatrix} \gamma_A \\ \gamma_B \\ \alpha_A \\ \alpha_B \\ AR \\ 10log(E) \\ \psi \end{pmatrix} = \begin{pmatrix} -10log\left(\frac{\langle V_1\rangle}{R_\lambda R_{load}}\right) - \frac{\beta}{2} \\ -10log\left(\frac{\langle V_2\rangle}{R_\lambda R_{load}}\right) - \frac{\beta}{2} \\ -10log\left(\frac{\langle V_3\rangle}{R_\lambda R_{load}}\right) - \frac{\beta}{2} \\ -10log\left(\frac{\langle V_4\rangle}{R_\lambda R_{load}}\right) - \frac{\beta}{2} \\ -10log\left(\frac{\langle V_5\rangle}{R_\lambda R_{load}}\right) - \frac{\beta}{2} \\ -10log\left(\frac{\langle V_6\rangle}{R_\lambda R_{load}}\right) - \frac{\beta}{2} \\ -10log\left(\frac{\langle V_7\rangle}{R_\lambda R_{load}}\right) - \frac{\beta}{2} \\ -10log\left(\frac{\langle V_8\rangle}{R_\lambda R_{load}}\right) - \frac{\beta}{2} + 10log(3.1mJ) - 70 \end{pmatrix}$$

Solving the system with a simple ®MATLAB function for linear least squares problem with the constraint on the loss terms to be in the range between 0 and 10 dB allows to find a value for the energy of laser pulse at the ModBox output in the order of few units of nanojoules. This is roughly the order of magnitude expected making us conclude that the described model and approach to the estimation is quite accurate. Results are reported in the following table.

Making some comments about the results we can clearly see that the connection between

ModBox output pulse energy	5.6711 nJ
ModBox fiber - photodiode coupling	6.5516 dB
Normal fiber - photodiode coupling	5.2644 dB
ModBox fiber - normal fiber	7.5519 dB
Normal fiber - fiber coupling	0.7984 dB
Absence of AR	0.0 dB
Free space - fiber coupling	2.6618 dB

Table 4.2: Least squares solution for the unknown term of losses and ModBox output energy

ModBox fiber and normal fiber produces the major amount of losses. Indeed, as we already mentioned, even if no information is available on its properties, we could see by eye that the ModBox fiber had a larger size and a different angle cut with respect to the normal one with 125 μm core diameter.
Other important terms of losses are due to the fiber - photodiode coupling. It is indeed reported in the datasheet of the detector a value of 80 μm for the active area diameter which, accounting also for a divergence of the beam due to the distance between the fiber end and the sensing surface, can reasonably produce a loss of around 5 or 6 dB.
Smaller losses instead are obtained for the collimator and for coupling between normal $\phi = 125\mu m$ fibers. While the former is still quite high due to possible reflections on the collimator surface and due to the hard and tricky alignment and focusing into the fiber, the latter is quite low as expected too.
Remains unexpected instead the result of 0 dB of losses due to the absence of the AR coating in fibers. Such value is clearly due to the constrain, indeed, negative quantity is reached otherwise. However the unexpected result agrees with the experimental measurement which reported on average higher voltages for the pulse collected after 2m long fiber *reversed* with respect to the one recorded after the same, but well placed, fiber.
In table 4.3 are reported the residuals of the least squares solution.

Measurement	Residual (dB)
MB fiber - PD	0.0000
MB fiber - 2m - PD	-0.4727
MB fiber - 2m - no AR - PD	-0.2919
MB fiber - 5m - PD	0.4300
MB fiber - (2+5)m - PD	0.3459
MB fiber - (2+2+5)m - PD	0.3116
MB fiber - (2+2+2+5)m - PD	-0.3230
collimator - (2+2+2+5)m - PD	0.0000

Table 4.3: Residuals of the least square problem

From what we see their value is in the same order of magnitude of the uncertainty on the measurements retrieved by the 6 takes of each measurement, confirming the reliability of the results.

The obtained result of 5.67 nJ for the ModBox output energy has been used in the simulation of the laser amplification described in the previous chapter. However, it must be said that since the initial population inversion of the RGA still remains a variable that is tuned accordingly to obtain good energy and shape fit, there is no way to compare this result with the energy retrieved by the simulation.

5 | Improvement of the temporal profile measurement

In this chapter the theory, the implementation at HPLF and the results of the Passive Pulse Replication System (PPRS) are presented.
All the work done found its basis in the paper of John R. Marciante *et.al.* published in 2007 [1], which presents this technique. Before entering the details of PPRS, two relevant issues with laser driven shock experiments that lead to the development of this method must be pointed out, namely the importance of the temporal profile of the drive laser pulse, especially in the proximity of the rising edge, and the impossibility to replicate the same shock with the same identical pulse shape on the same sample. The former requires a sufficiently clean signal recorded by the oscilloscope with the less possible amount of electrical noise while the latter prevents the possibility to obtain such high signal-to-noise ratio (SNR) with averages with other temporal measurements since only single - shot is available.
Regarding the importance of having a good quality temporal profile measurement there are essentially two fronts. From an operation-wise point of view it allows the facility to follow the evolution of the amplification and monitor the laser itself. From users point of view, it is extremely useful to use this pulse shape as an input for hydrodynamic simulations of laser - target interaction in order to reproduce as close as possible what they measured. With this, any noisy signal will be source of numerical instabilities which in the end generate unreliable results.
Following [1] the main idea is to obtain, with the help of passive elements, several temporal replicas of the drive pulse and to perform an average among them.
The complete description of this technique is discussed in the following section.

5.1. Passive pulse replication system

This paragraph sums up the work described in [1] and the main passages that, taken from there, have been adopted in our case.

Given that the best way to improve the SNR of a periodic signal is to average over many different recordings of it, the aim of the PPRS is to allow the same averaging without the need of other recordings but *creating replicas* of the single shot from itself. This is possible with a structure made of optical fibers of different lengths and optical couplers. Once collected a bounce of photons from the single pulse into a fiber, the idea is to make it run through a series of optical couplers that are able to split the incoming pulse into two identical parts of half the initial power each, and make them travel through two different paths. It is clear that, if a proper delay is introduced between the two outgoing branches of each coupler extending the length of one of them with the help of optical fiber, the splitted pulses will not overlap when passing through the subsequent couplers, allowing for the creation of a *train* of ideally identical pulses. Once the train is acquired by the oscilloscope it is only matter of slicing each single pulse among the sequence and make the average with them. A better visualization of what described is depicted below.

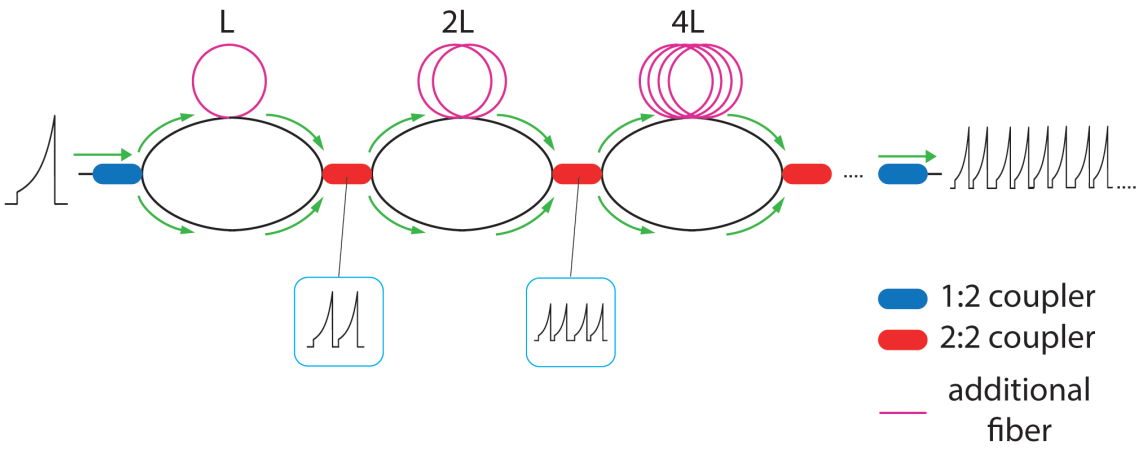

Figure 5.1: Schematics of the pulse replication system. The single pulse enters the first coupler from the left and gets splitted in two identical parts. The part running in the upper branch travels for a longer distance L before entering the second coupler. In such way the two parts are delayed in time. This system can be repeated with other identical modules, doubling each time the length of the fiber, allowing the same separation in time between each pulse.

In our particular case we used at the beginning a 1:2 coupler then 4 couplers 2:2 with power splitting ratio of 50 %, and at last another 2:1 coupler to bring back the two trains of pulses into one going up to the photodiode allowing for the production of 32 replicas. The chosen length L for the additional fiber employed was of 5 metres minimum up to 80 meters for the last stage. Assuming a velocity of $2 \times 10^8 m/s$ inside the fiber the induced

delay will be around 25 *ns*, thus leaving an interval of 15 *ns* among a train of 10 *ns* pulses. This delay is more than enough to avoid overlap and guarantee an easy slicing of each replica.

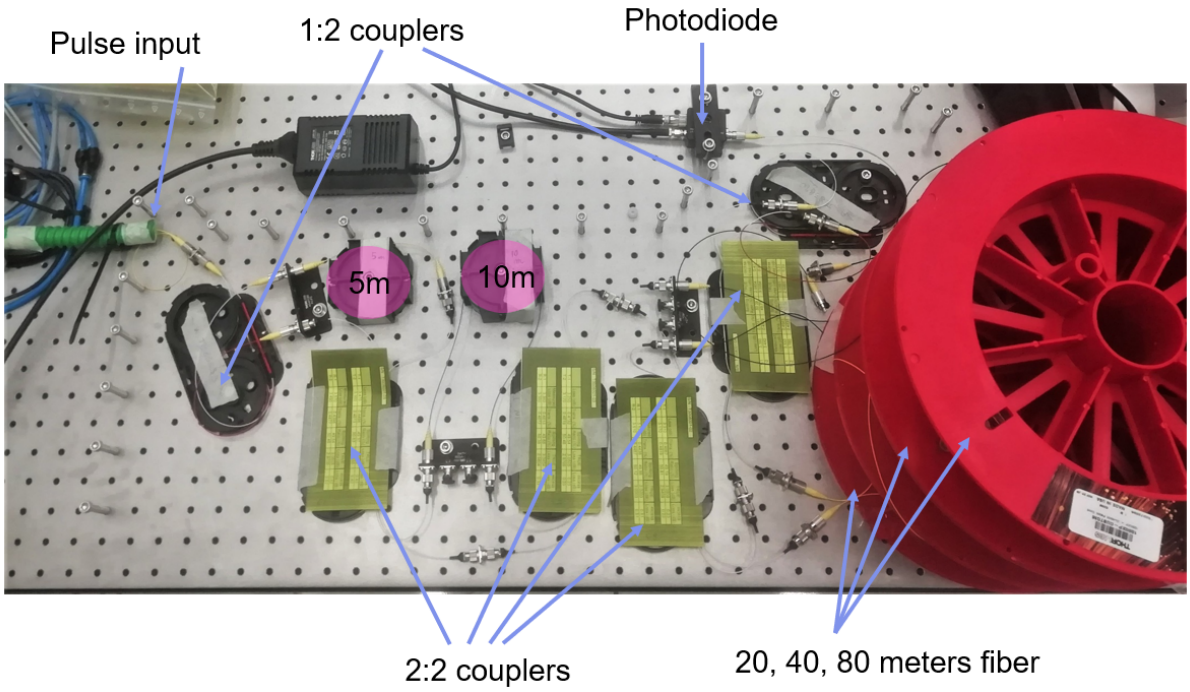

Figure 5.2: Implementation of the Passive Pulse Replication System in the HPLF Clean Room. The single pulse comes from the yellow fiber on the left and output train of replicas reaches the photodiode on the top of the image.

Up to now we described how to produce a train of replicas but it is worth mentioning also the method proposed in the paper for an optimal slicing. To make an efficient average we need all the replicas to be perfectly superimposed with each other, thus to know exactly the time intervals among the replicas. This is ideally identical for every replica if a sequence of additional fibers with subsequent doubled length is employed, but in practice, even if such fiber length configuration is chosen, small drifts can be present.
The idea suggested in the paper and adopted in our case is to calculate the cross-correlation function between the first pulse $P_1(t)$ and the whole train and find the maxima of this function.

$$X_{1j}(t) = F^{-1}\{F[P_1(t)] \times F^*[P_j(t)]\} \tag{5.1}$$

Indeed, the cross-correlation function has its maxima when $P_1(t)$ perfectly superimposes to the subsequent $P_j(t)$ pulses. In this way it would be only necessary to find the position

in time at which we have those maxima to retrieve the exact delay of $P_j(t)$ from $P_1(t)$, bypassing any impact due to possible timing error.

Before moving to the experimental results it is worth to discuss about the energy issues of the PPRS. Indeed, we must consider that when using this system the energy of the single pulse is divided into N small portions for each replica. This implies that the voltage signal at the oscilloscope is way lower than the one expected from the single pulse measurement having an actual SNR of the self-averaged pulse even worse than the SNR of the single shot measurement. However the major limit of the single shot measurement is the saturation voltage of the photodiode ($\approx 2V$) above which the recording is no longer reliable. One has thus to regulate the ND filters in order to have the maximum signal below the saturation threshold. On the other hand, when using the PPRS such partition of the single pulse energy reduces drastically the voltage peaks produced by the photodiode, allowing for the reduction of the neutral density filters applied, thus for a more efficient use of the optical signal for its measurement. In other words we could say that using the PPRS, in our case with $N = 32$, the upper bound for the pulse energy is no longer the photodiode saturation voltage but the fiber damage threshold which usually is higher than the power needed to saturate the photodiode.
Indeed, from fiber specifications (see ®THORLABS website [46]) the estimated damage threshold intensity for a 10 ns pulse is in the order of the GW/cm^2 while using 4.2 and considering for the photodiode an active area of $\phi = 80\mu m$, for $2\,V$ we obtain an optical intensity 100 times smaller with no losses considered to reach saturation.

5.2. Experimental results

In this section the temporal measurements recorded with the PPRS system are presented. Two types of measurement have been carried out: firstly using the same ND filters in front of the collimator and secondly adjusting them in order to reach approximately the same voltage peak level.
All the measurement we are presenting were taken before the D5 amplifier while the final aim will be to employ the system closer to the interaction chamber, picking up a portion of the leakage from one of the last mirrors.

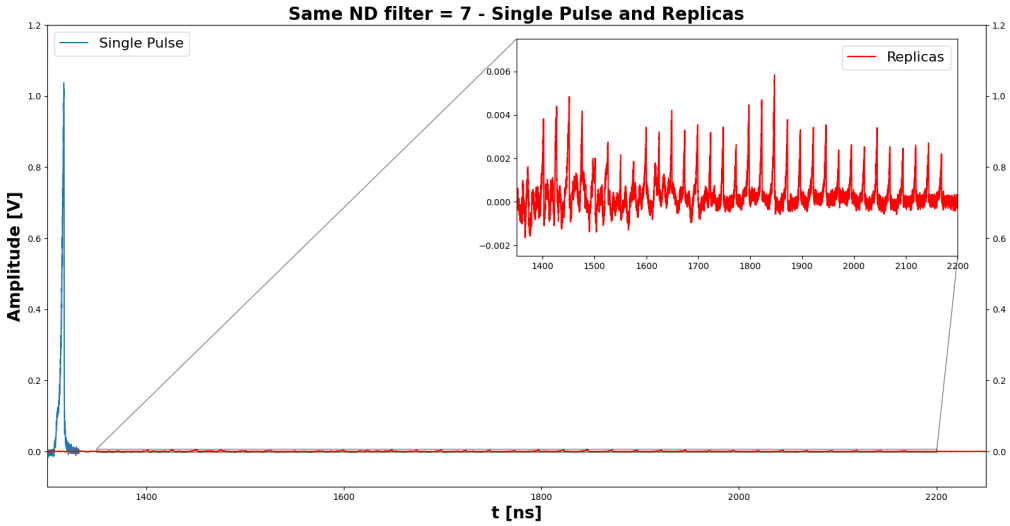

Figure 5.3: Oscilloscope recording using the same ND filter. Looking at the top right pane we see an higher noise level in the first region because we are measuring pulses close in time to the Pockels cell discharge.

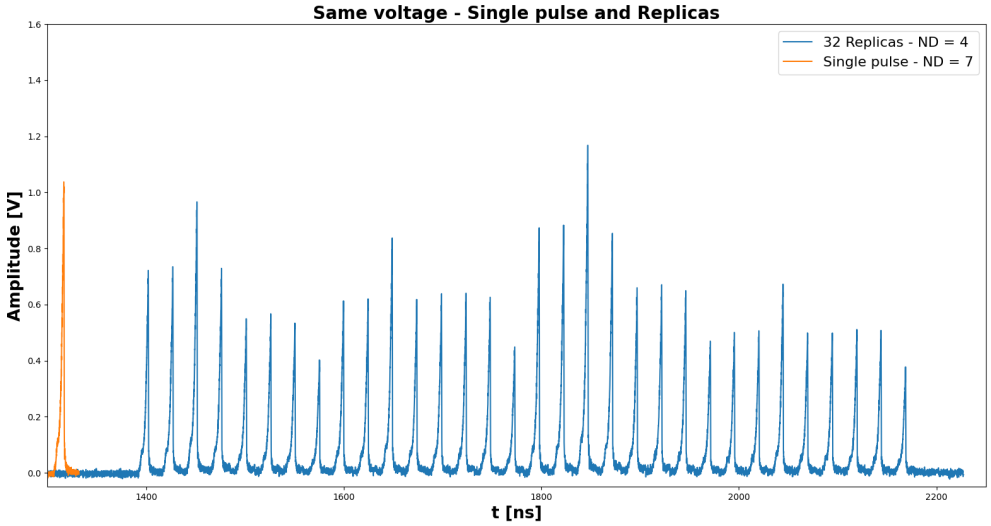

Figure 5.4: Oscilloscope recording maximizing signal intensity.

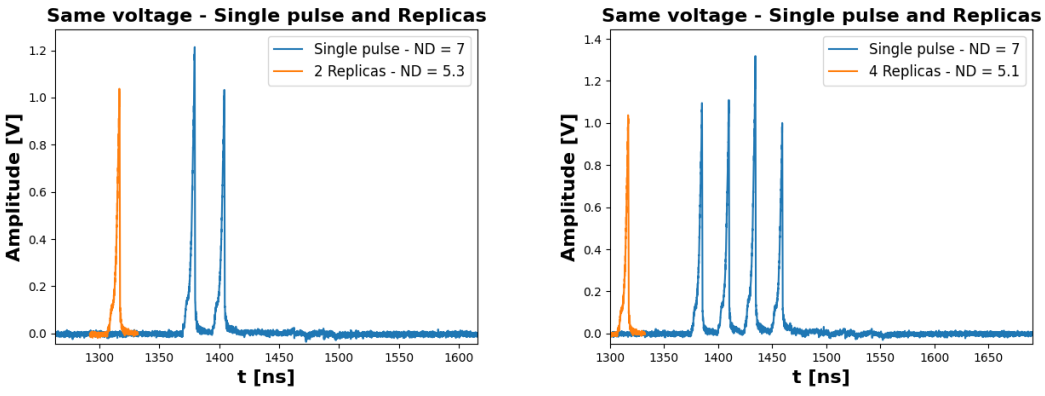

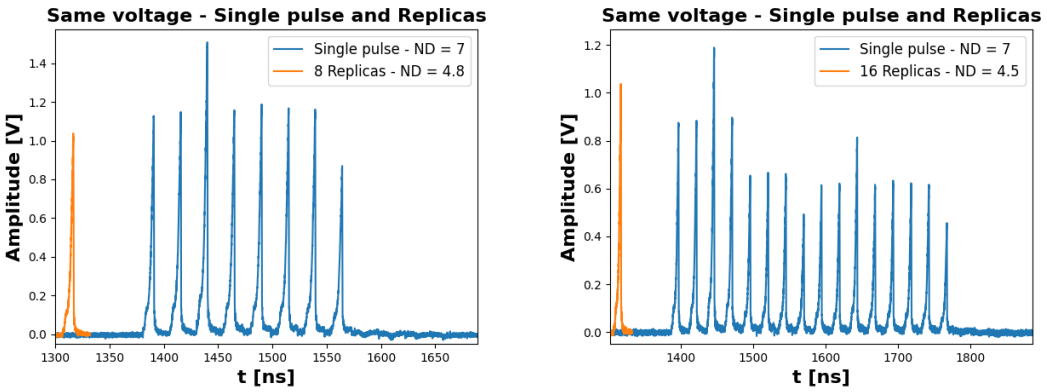

As we can see from figures above it is almost impossible to reach the same voltage peaks the single shot and for the replicas. Indeed, in addition to the difficulty to find the good ND value, there is an unavoidable difference among the amplitudes of the replicas. To have a rough idea of the reason of this mismatch we can consider that early arriving pulses encounter less fiber connectors and travel through less meters of fiber losing a smaller amount of energy than the late ones. However, considering these last sources of losses in a dedicated simulation of the PPRS we should see a trend of intensities going like the one depicted below.

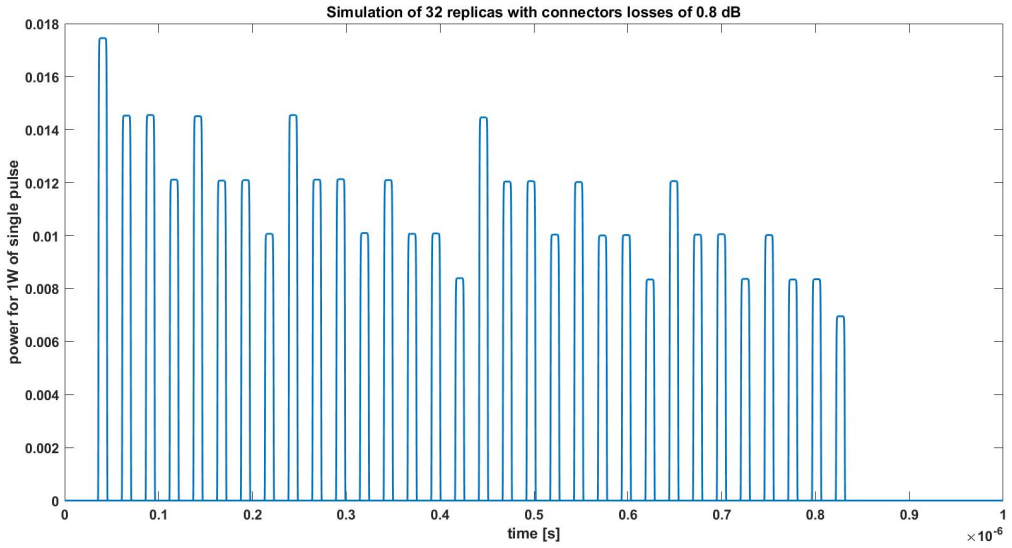

Figure 5.5: Simulated train of pulses for a square 1W input pulse. Connector losses and fiber length should affect the amplitude of the recorded voltage signal in this way. Indeed first arriving pulse travels through shorter lengths and encounters only 7 connectors while the last, other than running a longer path crosses 12 connectors.

The simulation has been calculated considering the combination of all the 32 paths through all the branches of the PPRS and counting 1 connector for each short branch, (the one

connecting only couplers) and counting 2 connectors for each longer branch (coupler-fiber and fiber-coupler). The amount of losses per fiber connector is the one obtained from the analysis of the previous chapter. From the comparison with the experimental measurement we can recognize the four clusters of 8 replicas each which have approximately the same trend among them. However while in the simulation those cluster are gradually decreasing in intensity when moving to late times of arrival, in the measurements we do not see this clear decrease. Moreover, the most resulting disagreement is on the amplitude of the first and third peak of each cluster which are weirdly lower and higher respectively than expected. The reasons of this disagreement are most likely related to some imperfection in the connections or in the input or output ports of some piece of fiber used. Retrieving this anomaly in the implemented system can be quite complicated, out of the scope of this work and not necessarily required to conduct a meaningful analysis of the train on replicas and obtain an improved SNR.

5.3. Analysis of the measurements

It is now the time to look at the result of the processed measurements. A Python based script has been developed to manipulate the oscilloscope recordings and both the set of data have been analysed. In particular, in the first case in which the neutral density filters remained unchanged we should expect the SNR to remain the same or at least getting worse. Indeed, as anticipated in the previous section, in the PPRS the energy of the pulse by splitting reduces down to very low levels while the noise level remains the same of the single shot measurement. Thus the average on the replicas does not bring any improvement, on the contrary, decreases due to energy losses during the PPRS.

For the second set of measurements, the ones taken changing ND filters and maximizing the voltage signal below the photodiode saturation threshold, the improvement of the SNR is significantly high as we can see from Fig. 5.7 below.

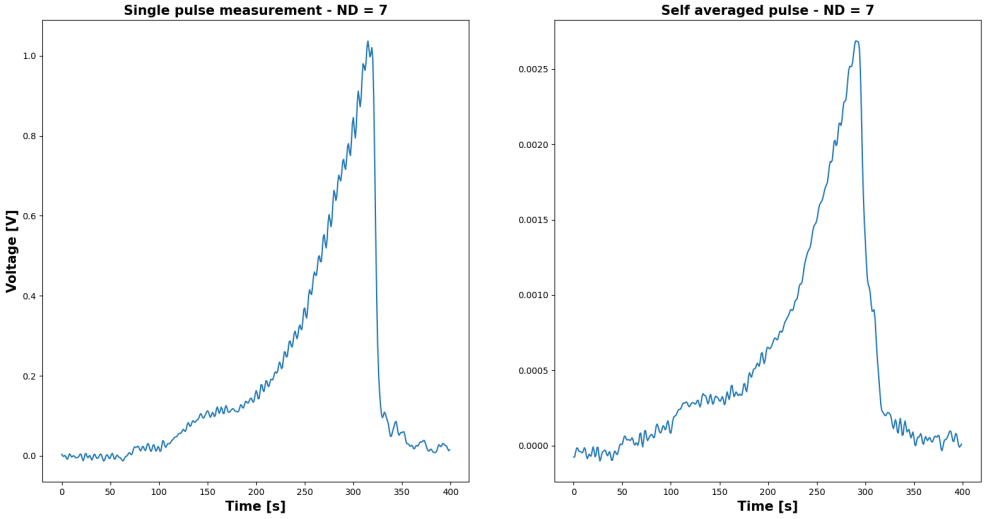

Figure 5.6: Comparison between the single pulse measurement and the self averaged one in the case in which the optical power used for the single pulse measurement is the same injected into the PPRS (same ND filter used). It is clear that the SNR did not improve but got worse.

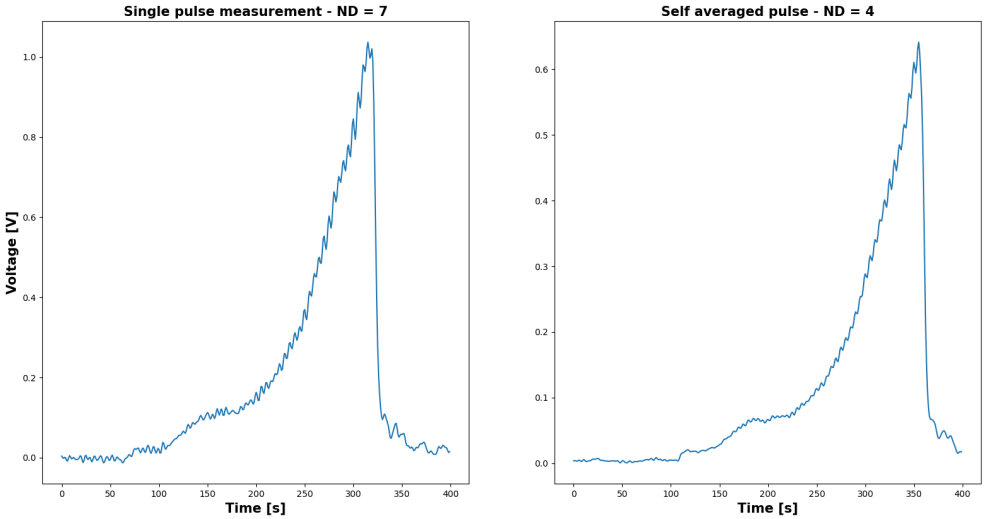

Figure 5.7: Comparison between the single pulse measurement and the self averaged one in the case in which the optical power in input of the PPRS is adjusted to obtain the same voltage value of the single pulse measurement. The quality of the self - averaged pulse signal is definitely better than the single one. The serrated crest that we see is the amplitude modulation effect of the SSD system described in chapter 2 indeed it is preserved in the average.

Looking at the numbers and remembering the mentioned difficulty of obtaining the same voltage among measurements, we see an improvement of the SNR of less than the expected factor $\sqrt{32}$. This is probably due to the smaller voltage peak reached by the average of the 32 replicas with respect to the voltage of the single pulse. However, even if we assume to have the same voltage level for both the averaged pulse and the single one we still reach a ratio of the SNRs smaller than expected. This last operation is acceptable when the SNR ratio is evaluated, if we assume the only source of noise coming from the oscilloscope. Indeed, the noise level of the two signals remains unvaried while we only change the amplitude of the signal which in principle could be obtained just injecting more optical power inside the PPRS, i.e. reducing even more the absorptive power of the ND filters.
An hypothesis that might explain this behaviour can be that the noise is not truly random but there is a kind of dependence on something either in the oscilloscope or in the photodiode. For instance, when slicing the replicas, the first temporal region of the cropped pulses still might have some residual signal on the late edge of the previous pulse in the train. Since this first temporal region of the averaged pulse is the one used for the calculation of the noise RMS for the SNR, the presence of noise coming form the discharge of the photodiode and the RGA's Pockels cell discharge as shown in inset of 5.3 can in a way perturb the randomness of the oscilloscope noise, thus affect the $\sqrt{N}$ law. In support to this hypothesis there is the fact that the more replicas we consider, the more pronounced is the drift of the experimental SNR ratio with respect to the $\sqrt{N}$ law, as we can see from Fig.5.8. On the other hand, if we compute the noise RMS using few points in the temporal region next to the rising edge of the pulse, far from possible residual effects of photodiode discharge we clearly see a difference and better agreement with the theoretical curve (Fig.5.9)

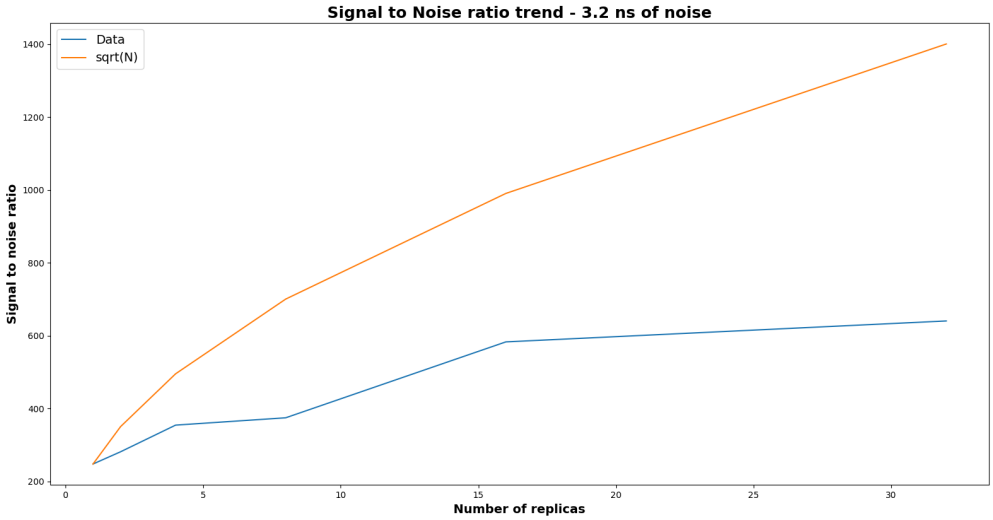

Figure 5.8: Signal to noise ratio theoretical and experimental improvement along with the number of replicas used for the average. Noise evaluation over the first 3.2 ns before the beginning of each averaged pulse (80 points)

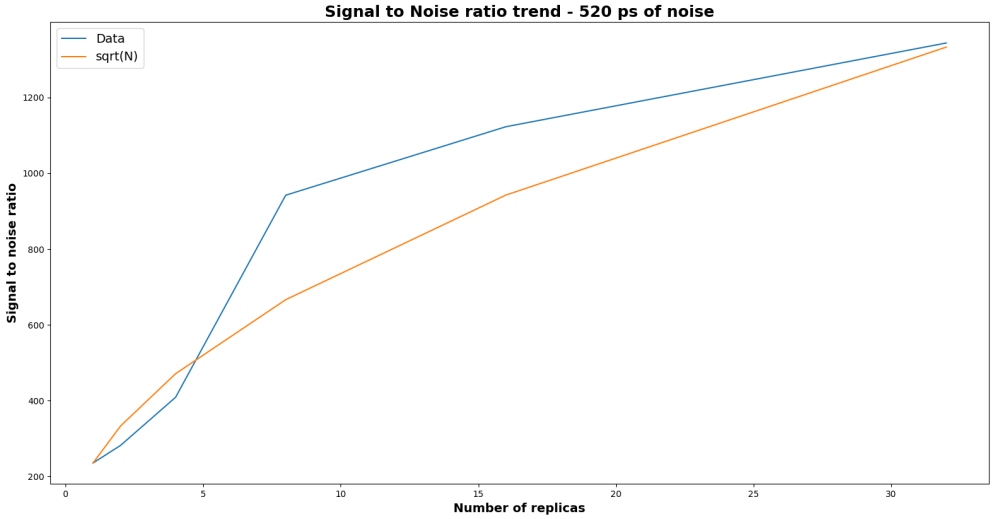

Figure 5.9: Noise evaluation over the first 520 ps before the beginning of each averaged pulse (13 points)

Beside the trend of the SNR curve along with the number of replicas one could also look at the autocorrelation of the portion of time corresponding to the beginning of the recording, i.e. before the arrival of the first replica, and the the one corresponding to the

time interval between two replicas. In the first case we characterize the noise coming only from the oscilloscope while in the second case both the photodiode and the oscilloscope constitute sources of noise. Indeed, it is known that a purely stochastic process is totally uncorrelated in time, thus its autocorrelation function is zero everywhere.

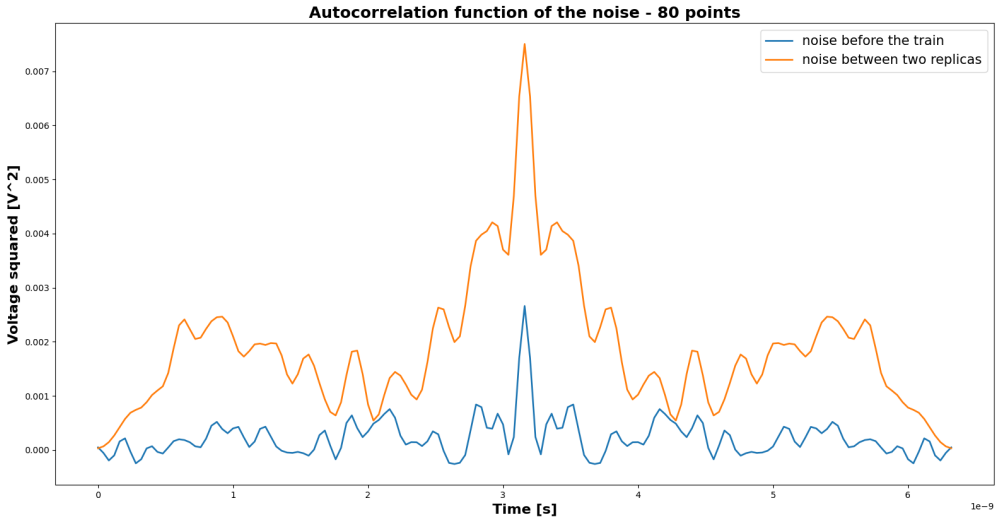

Figure 5.10: Autocorrelation function of the noise level before and in between the train of pulses. Except for the peak in the middle due to perfect temporal overlap of the noise with itself, it is clear that the noise before the arriving of the pulses has an higher degree of randomness with respect to the noise we find in the time intervals among replicas.

Except for the peak in the center of symmetry which corresponds to zero delay between the signal and itself (in other words, correlation for infinite frequencies), Fig.5.10 shows clearly that the noise coming only from the oscilloscope is substantially uncorrelated, i.e. stochastic, while the noise recorded in the 3.2 ns before the beginning of the n-th replica cannot be considered purely random. This can explain the trend of the SNR curve with number of averages and also allows us to conclude the the source of correlated noise most likely the discharge of the photodiode as supposed above, meaning that in order to see a better agreement of the experimental SNR trend with the theoretical one, longer fiber lengths should be employed in the PPRS.

In conclusion to this chapter we could say that the aim of improve the quality of the laser temporal profile measurement with the PPRS has been achieved. It really is an added value to the diagnostic of the single shot laser experiments. Moreover, the setup is

	SNR
Single pulse	220.22
Averaged (same ND)	81.55
Averaged (almost same voltage)	365.42
Averaged (same voltage)	640.17
Averaged (same voltage - less points)	1343.66
Averaged (ideal)	1261.65

Table 5.1: Summary of the SNR values

quite simple so that other modules (coupler + additional fiber) can be easily added. This will be indeed the future development to further increase the SNR of the measurements. Another step forward could be the substitution of the first 1:2 splitter with a 2:2 coupler and exploit both inputs to passively replicate and self-average two different pulses. This modification though will need a careful choice of the delay between the two input pulses to avoid overlap among their replicas. Once these upgrades will be considered and a more compact setup will be designed, the PPRS will be installed as a permanently diagnostic of the HPLF helping both the beamline staff and users with the monitoring of the laser and with reliable simulation inputs respectively.

6 | Conclusions and future developments

The aim of this work was to present part of latest developments conducted for the characterisation of the high power laser of ID24-HPLF at ESRF. Starting from the crucial importance of the quality of the temporal profile of the drive laser pulse in laser induced shock compression experiments, two different studies have been carried out. A complete model of the whole amplification chain has been considered to simulate the effect of temporal distortion induced by gain saturation in amplifiers. Comparison of simulation results with the experimental measurements showed a quite good agreement both for the temporal shape and the energy. Moreover, the simulation proves to be a reliable instrument to reconstruct the optimal temporal profile and energy of the seed pulse for any given target shape and energy. It thus represents an helpful tool for both beamline operators and users to monitor and shape the laser pulse. One of the main limits of the simulation is the absence of accurate knowledge of some parameters, namely the initial population inversion *in primis* for each amplifier, and the actual stimulated emission cross section that depends on the unknown amount of Nd^{3+} doping and the specificities of the glass host. While the latter is as ©Amplitude trade secret, the former can be estimated with specific measurements. Nevertheless, many approximations have been considered and future developments might work on the complete modeling of such neglected effects. Among them, a complete model of the amplification also for the case of the partial temporal overlap would be desirable as well as the modeling of flash lamps pumping distribution along the propagation direction of the beam. All these measures could improve the agreement between simulations and measurements of the temporal shape thus furnish better estimation of energy losses.
However, in the next periods the most useful further development would be the correct model of the ModBox pulse shaper behaviour, so to conclude the simulation and obtain as a result the digital input for the Arbitrary Waveform Generator.

On the other side, the adaptation to our case and the implementation of the Passive Pulse

Replication System allowed a significant improvement of the quality of the temporal profile measurement. Besides the benefit produced by the self-average, such system makes possible to exploit all the optical power that the fiber system can withstand without the risk of damaging to increase the signal over the noise level of the oscilloscope. Although the results are already showing an enhancement of the SNR of the self-averaged pulse, further upgrades can be planned. The addition of a further 2:2 coupler to achieve a larger number of replicas would be the next step and a more compact setup, installed in the laser diagnostic will be designed. For purely statistical interests it would be curious to investigate more deeply the reasons why the $\sqrt{N}$ law for the SNR improvement is not respected. Attempts to make purely uncorrelated the noise over the signal, as suggested, could be a way for this scope.

Beside these two main major activities a further study has been conducted to overcome a technical issue that somehow contributed to leave unknown another parameter of the simulation. The ModBox output energy was indeed necessary as input for the simulation, and the obtained value from the estimation has been used to produce the results shown in section 3.5. Even if in the next future a dedicated energy meter sensitive in the nJ range will be purchased, the conducted work, beside providing estimations of the amount of losses per each element in the pipeline, confirmed the suspects of loss of power from the ModBox output raised by ©Amplitude laser engineers. Further developments on this side would be, after the comparison with a direct energy measurement, the collection of a larger number of measurements with different configurations to strengthen the estimation and refine the proposed physical model of the ModBox.

Bibliography

[1] J. R. Marciante, W. R. Donaldson, and R. G. Roides, "Averaging of Replicated Pulses for Enhanced Dynamic-Range Single-Shot Measurement of Nanosecond Optical Pulses," *IEEE PHOTONICS TECHNOLOGY LETTERS*, vol. 19, pp. 1344–1346, 2007.

[2] S. Pascarelli, O. Mathon, T. Mairs, I. Kantor, G. Agostini, C. Strohm, S. Pasternak, F. Perrin, G. Berruyer, P. Chappelet, C. Clavel, and M. C. Dominguez, "The Time-resolved and Extreme-conditions XAS (TEXAS) facility at the European Synchrotron Radiation Facility: the energy-dispersive X-ray absorption spectroscopy beamline ID24," *Journal of Synchrotron Radiation*, no. 23, 2016.

[3] V. Mowlika, C. Naveen, A. Phani, A. Sivakumar, S. M. B. Dhas, and R. Robert, "Shock wave induced magnetic phase transition in cobalt ferrite nanoparticles," *Materials Chemistry and Physics*, vol. 275, p. 125300, 2022.

[4] A. Sivakumar, S. Ramya, S. Sahaya Jude Dhas, A. I. Almansour, R. S. Kumar, N. Arumugam, M. Murugesan, and S. Martin Britto Dhas, "Assessment of crystallographic and electronic phase stability of shock wave loaded cubic cerium oxide nanoparticles," *Ceramics International*, vol. 48, no. 2, pp. 1963–1968, 2022.

[5] N. Sévelin-Radiguet, R. Torchio, G. Berruyer, H. Gonzalez, S. Pasternak, F. Perrin, F. Occelli, C. Pépin, A. Sollier, D. Kraus, A. Schuster, K. Voigt, M. Zhang, A. Amouretti, A. Boury, G. Fiquet, F. Guyot, M. Harmand, M. Borri, J. Groves, W. Helsby, S. Branly, J. Norby, S. Pascarelli, and O. Mathon, "Towards a dynamic compression facility at the ESRF," *Journal of Synchrotron Radiation*, vol. 29, pp. 167–179, Jan 2022.

[6] K. K. M. Lee, L. R. Benedetti, R. Jeanloz, P. M. Celliers, J. H. Eggert, D. G. Hicks, S. J. Moon, A. Mackinnon, L. B. Da Silva, D. K. Bradley, W. Unites, G. W. Collins, E. Henry, M. Koenig, A. Benuzzi-Mounaix, J. Pasley, and D. Neely, "Laser-driven shock experiments on precompressed water: Implications for "icy" giant planets," *The Journal of Chemical Physics*, vol. 125, no. 1, p. 014701, 2006.

[7] W. Grochala, R. Hoffmann, J. Feng, and N. Ashcroft, "The chemical imagination at work in very tight places," *Angewandte Chemie (International ed. in English)*, vol. 46, pp. 3620–42, 07 2007.

[8] H. He, T. Sekine, T. Kobayashi, and K. Kimoto, "Phase transformation of germanium nitride (Ge_3N_4) under shock wave compression," *Journal of Applied Physics*, vol. 90, no. 9, pp. 4403–4406, 2001.

[9] A. Zylstra, O. Hurricane, D. Callahan, A. Kritcher, J. Ralph, H. Robey, J. Ross, C. Young, K. Baker, D. Casey, T. Döppner, L. Divol, M. Hohenberger, S. Pape, A. Pak, P. Patel, R. Tommasini, S. J. Ali, P. Amendt, and G. Zimmerman, "Burning plasma achieved in inertial fusion," *Nature*, vol. 601, pp. 542–548, 01 2022.

[10] M. Guaraglini, *Laser-driven shock compression of liquid mixtures and silica up to extreme thermodynamic conditions of interest for planetary interior models*. PhD thesis, Université Paris-Saclay, HAL, 11 2019.

[11] M. Koenig, A. Benuzzi-Mounaix, A. Ravasio, T. Vinci, N. Ozaki, S. Lepape, D. Batani, G. Huser, T. Hall, D. Hicks, A. MacKinnon, P. Patel, H. S. Park, T. Boehly, M. Borghesi, S. Kar, and L. Romagnani, "Progress in the study of warm dense matter," *Plasma Physics and Controlled Fusion*, vol. 47, pp. B441–B449, nov 2005.

[12] M. Bonitz, T. Dornheim, Z. A. Moldabekov, S. Zhang, P. Hamann, H. Kählert, A. Filinov, K. Ramakrishna, and J. Vorberger, "Ab initio simulation of warm dense matter," *Physics of Plasmas*, vol. 27, no. 4, p. 042710, 2020.

[13] M. Desjarlais, "Warm dense matter."

[14] S. Minomura and H. Drickamer, "Pressure induced phase transitions in silicon, germanium and some III–V compounds," *Journal of Physics and Chemistry of Solids*, vol. 23, no. 5, pp. 451–456, 1962.

[15] T. S. Duffy and R. F. Smith, "Ultra-High Pressure Dynamic Compression of Geological Materials," *Frontiers in Earth Science*, vol. 7, 2019.

[16] T. J. Ahrens, "Dynamic compression of earth materials," *Science*, vol. 207, no. 4435, pp. 1035–1041, 1980.

[17] J.-P. Davis, M. D. Knudson, and J. L. Brown, "Results from new multi-megabar shockless compression experiments at the z machine," *AIP Conference Proceedings*, vol. 1793, no. 1, p. 060015, 2017.

[18] J. Lin and T. F. George, "Laser-generated electron emission from surfaces: Effect of the pulse shape on temperature and transient phenomena," *Journal of Applied Physics*, vol. 54, no. 1, pp. 382–387, 1983.

[19] A. Cordone, "Laser induced dynamic compression of vitreous GeO_2 up to the TPa regime," Master's thesis, Politecnico di Milano, 2021.

[20] W. M. Rankine, "On the thermodynamic theory of waves of finite longitudinal disturbance," *Philosophical Transactions of the Royal Society of London*, vol. 160, pp. 277–288, 1870.

[21] Hugoniot, "Mémoire sur la propagation du mouvement dans un fluide indéfini (première partie)," *Journal de Mathématiques Pures et Appliquées*, vol. 3, pp. 477–492, 1887.

[22] M. Koenig, B. Faral, J. M. Boudenne, D. Batani, A. Benuzzi, and S. Bossi, "Optical smoothing techniques for shock wave generation in laser-produced plasmas," *Phys. Rev. E*, vol. 50, pp. R3314–R3317, Nov 1994.

[23] G. Berruyer, C. Clavel, H. Gonzalez, D. Lorphèvre, O. Mathon, S. Pascarelli, S. Pasternak, A. R.-B. Florian Perrin, N. Sévelin-Radiguet, R. Torchio, F. Torrecillas, and F. Villar, "High Power Laser Facility - Phase 1." ESRF, 03 2019. Technical Design Report.

[24] S. Pascarelli, "Fundamentals of x-ray absorption fine structure: basic principles," 2017.

[25] M. Borri, C. Cohen, O. Fox, J. Groves, W. Helsby, O. Mathon, L. McNicholl, S. Pascarelli, K. Sawhney, R. Torchio, and M. Zuvic, "Characterisation of ge micro-strip sensors with a micro-focused x-ray beam," *Nuclear Instruments and Methods in Physics Research Section A: Accelerators, Spectrometers, Detectors and Associated Equipment*, vol. 988, p. 164932, 2021.

[26] M. Borri, C. Cohen, J. Groves, W. Helsby, O. Mathon, L. McNicholl, S. Pascarelli, N. Sévelin-Radiguet, R. Torchio, and M. Zuvic, "Prototyping experience with ge micro-strip sensors for edxas experiments," *Nuclear Instruments and Methods in Physics Research Section A: Accelerators, Spectrometers, Detectors and Associated Equipment*, vol. 1017, p. 165800, 2021.

[27] M. Zavelani-Rossi and F. Vismarra, *High Intensity Lasers for Nuclear and Physical Applications*. Società Editrice Esculapio, 2020.

[28] S. Skupsky, R. W. Short, T. Kessler, R. S. Craxton, S. Letzring, and J. M. Soures,

"Improved laser beam uniformity using the angular dispersion of frequency-modulated light," *Journal of Applied Physics Vol.66*, no. 8, pp. 3456 – 3462, 1989.

[29] J. Furthner and A. Penzkofer, "Emission spectra and cross-section spectra of neodymium laser glasses," *Optical and Quantum Electronics*, vol. 24, pp. 591–601, 05 1992.

[30] J. Campbell and T. Suratwala, "Nd-doped phosphate glasses for high-energy/high-peak-power lasers," *Journal of Non-Crystalline Solids*, vol. 263-264, pp. 318–341, 2000.

[31] C.Bibeau and S.A.Payne, "Terminal-Level Relaxation in Nd-doped laser materials," *ICF Quarterly Report, Lawrence Livermore National Laboratory Report UCRL-LR-*, no. 105821-95-2, p. p.119, 1995.

[32] L. M. Frantz and J. S. Nodvik, "Theory of Pulse Propagation in a Laser Amplifier," *Journal of Applied Physics 34*, pp. 2346–2349, 1963.

[33] V. Ivanov, Y. Senatsky, and G. Sklizkov, "Stimulated raman scattering in a laser glass," *JETP Letters*, vol. 47, pp. 95–98, 01 1988.

[34] A. Penzkofer and W. Kaiser, "Nonlinear loss in nd-doped laser glass," *Applied Physics Letters*, vol. 21, no. 9, pp. 427–430, 1972.

[35] D. Schimpf, C. Ruchert, D. Nodop, J. Limpert, A. Tünnermann, and F. Salin, "Compensation of pulse-distortion in saturated laser amplifiers," *Optics express*, vol. 16, pp. 17637–46, 11 2008.

[36] M. Li, X. M. Zhang, Z. G. Wang, X. D. Cui, X. W. Yanand X. Y. Jiang, J. G. Zheng, and W. Wang, "Analytical and numerical solutions to the amplifier with incoherent pulse temporal overlap," *Optics Communications*, vol. 382, pp. 49–57, 2017.

[37] C. Brito Cruz, J. Gordon, P. Becker, R. Fork, and C. Shank, "Dynamics of spectral hole burning," *IEEE Journal of Quantum Electronics*, vol. 24, no. 2, pp. 261–269, 1988.

[38] V. Grabovskii, V. I. Prokhorenko, and V. N. Sukhovatkin, "Specific features of laser pulse amplification in double-pass single-stage amplifiers," *Soviet Journal of Quantum Electronics*, vol. 22, pp. 865–868, 1992.

[39] S. Pearce, C. Ireland, and P. Dyer, "Simplified analysis of double-pass amplification with pulse overlap and application to Nd:YVO4 laser," *Optics Communication*, vol. 22, pp. 297–303, 2005.

[40] J. Jeong, S. Cho, and T. J. Yu, "Numerical extension of Frantz - Nodvik equation for double-pass amplifiers with pulse overlap," *Opt. Express*, vol. 25, pp. 3946–3953, Feb 2017.

[41] R. A. Minasian, "Modulation and demodulation of optical signals," *Encyclopedia of Modern Optics*, pp. 129–138, 2005.

[42] C. Nölleke, "Schematischer aufbau eines mach-zehnder-modulators. bs: Strahlteiler, m: Spiegel.," 2008.

[43] A. Hilt, E. Udvary, G. Járó, and T. Berceli, "Harmonic components and dispersion of mobile network signals due to fiber-optical transmission," 05 2017.

[44] iXblue company, "Modbox-front-end – the latest improvements – july 2020," 2020.

[45] THORLABS, "DET08CFC(/M) Fiber Input InGaAs Biased Detector User Guide,"

[46] THORLABS, "Damage threshold of silica single mode fibers,"

A | Appendix A

To derive the relationship between the optical power captured by the photodiode and the voltage at the oscilloscope we should start considering the voltage produced at the photodiode output.

$$V_{pd} = R_\lambda P_{in} R_{load} \tag{A.1}$$

From wire specifications we have the losses for 10 meters cable in dB meaning that

$$P_{wire} = P_{pd} 10^{-\frac{\beta}{10}} = (R_\lambda P_{in})^2 R_{load} 10^{-\frac{\beta}{10}} \tag{A.2}$$

where Ohm's law has been used to express the power at the photodiode output in terms of the generated current.
If we now consider that the impedance of the wire is the same as the input impedance of the oscilloscope (50 Ω) we can obtain an expression for the voltage read by the oscilloscope.

$$\frac{V_{osc}^2}{R_{load}} = P_{osc} = P_{wire} = (R_\lambda P_{in})^2 R_{load} 10^{-\frac{\beta}{10}} \tag{A.3}$$

$$V_{osc}^2 = (R_\lambda P_{in} R_{load})^2 10^{-\frac{\beta}{10}} \tag{A.4}$$

From which we obtain 4.1.

List of Figures

List of Tables

List of Symbols

Variable	Description	SI unit
$\boldsymbol{h}$	Planck constant	J $\cdot s$
$\boldsymbol{c}$	speed of light in the gain medium	m/s
$\boldsymbol{\nu}$	frequency of the laser radiation	$\mathrm{m}^{-3} \cdot s^{-1}$
$\boldsymbol{R_p}$	pumping rate	$\mathrm{m}^{-3} \cdot s^{-1}$
$\boldsymbol{W}$	rate of stimulated emission	s^{-1}
$\boldsymbol{\tau_i}$	lifetime of the i-th atomic energy level	s
$\boldsymbol{F}$	photon flux	$\mathrm{m}^{-2} \cdot s^{-1}$
$\boldsymbol{\sigma_s}$	stimulated emission cross section	m^2
$\boldsymbol{\Gamma_s}$	saturation fluence	$\mathrm{J/m}^2$
$\boldsymbol{\rho}$	radiation energy density	$\mathrm{J/m}^3$
$\boldsymbol{\tau_p}$	pulse duration	s
$\boldsymbol{G_0}$	small signal gain	-
$\boldsymbol{\phi}$	diameter	m
$\boldsymbol{n}$	refraction index	-
$\boldsymbol{r}$	electro-optic coefficient	m/V
$\boldsymbol{\lambda}$	laser wavelength	m
$\boldsymbol{\Delta\phi}$	phase shift	rad
$\boldsymbol{V_\pi}$	voltage to produce a π phase shift	V
$\boldsymbol{R_\lambda}$	photodiode responsivity	A/W
$\boldsymbol{R_{load}}$	load resistance	Ω
$\boldsymbol{\beta}$	electrical cable losses	dB
$\boldsymbol{\gamma}$	fiber-photodiode losses	dB
$\boldsymbol{\alpha}$	fiber-fiber connection losses	dB
$\boldsymbol{\psi}$	free space - fiber coupling losses	dB

Acknowledgements

My acknowledgements go firstly to my Advisor Prof. Ghiringhelli for giving me the opportunity to develop my thesis work at the ESRF. At the same way, I want to thank my Supervisor at the ESRF, Dr. Nicolas Sévelin-Radiguet, who carefully guided me from the beginning of the internship, supporting me, clarifying my doubts and teaching me a lot. A big thank goes also to Prof. Gianluca Valentini for sharing his opinions with me about chapter 4.

My thanks go also to all the staff of the beamline ID24, from my office mates and friends Sofia, Luca, Anastasia and Federico to Raffaella, Jean-Alexis, Olivier, João, Cesare, Florian, Kirill and Angelika, for the time spent conversing with them either of physics either of everyday life.